Julius-Maximilians-
UNIVERSITÄT
WÜRZBURG

UNIVERSITÄT WÜRZBURG
PHYSIKALISCHES INSTITUT
epVI

Optically Detected Magnetic Resonance on Organic and Inorganic Carbon-Based Semiconductors

Dissertation zur Erlangung des
naturwissenschaftlichen Doktorgrades
der Julius-Maximilians-Universität Würzburg

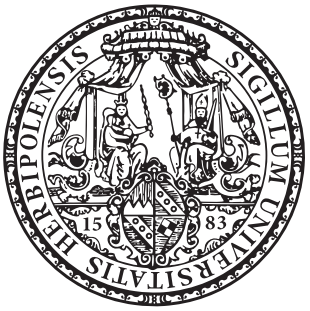

vorgelegt von
Hannes Kraus
aus Würzburg

Würzburg, 2014

Eingereicht am 15. September 2014
bei der Fakultät für Physik und Astronomie

1. Gutachter: Prof. Dr. Vladimir Dyakonov
2. Gutachter: Prof. Dr. Tobias Hertel
3. Gutachter: Prof. Dr. Etienne Goovaerts
der Dissertation.

Vorsitzende(r)

1. Prüfer: Prof. Dr. Vladimir Dyakonov
2. Prüfer: Prof. Dr. Tobias Hertel
3. Prüfer: Prof. Dr. Matthias Kadler
im Promotionskolloquium.

Tag des Promotionskolloquiums: 17.11.2014

Doktorurkunde ausgehändigt am

To my daughter

Lina Magali

Hoping that you will pursue your dreams. If I can someday read a similar document with your name on it, I'll be happy. If not, I'll be equally happy. As long as you are!

Contents

1. Introduction

Carbon is an amazing element. Not only is it the fourth most abundant material in the universe, it is so indispensable for sustaining our life; the lack of alternatives to a carbon based biosystem coined the word „carbon chauvinism“ among exobiologists [1]. Carbon is the main architect of our life – not only consist we of carbon, we are also depending on its many forms and allotropes; starting from a small wood cooking fire, and ending in carbon nanotube extended fabrics. One of the exceptional points of carbon is its extreme versatility. It forms the most numerous compounds of all elements, and its many varieties have founded a whole scientific area, the organic chemistry.

This work devotes itself to the research on three of these carbon forms and allotropes: organic semiconductors for applications in organic photovoltaics, semiconducting nanotubes, and the compound silicon carbide. The common denominator here is the applied method: The optically detected magnetic resonance (ODMR) enables insight into the spin-dependent excitation and charge carrier kinetics of optically active species.

Organic semiconductors adress an important issue nowadays: The abandonment of fossil and nuclear power create a great demand for affordable and efficient renewable energy sources. The organic photovoltaics, and its younger, even more promising organic-inorganic hybrid sibling, the metal halide perovskite solar cell, strive to create a viable alternative for classic silicon photovoltaics. To maintain competitiveness, fundamental research on the excitation pathways en route to charge carrier dissociation and, ultimately, photocurrent, is indispensable. This work tries to motivate the research of triplet exciton states in organic photovoltaic materials, and to provide some insight into the influence of energy level balancing on possible photocurrent loss mechanisms.

Carbon nanotubes are a hot topic not only scientifically; they are also one of the few solid state physics topics that ring a bell in the general population. Their unique structural and electronic properties incite a whole series of possible applications, of which regrettably only a fraction is being realized now. For other applications, especially in electronics, more knowledge about the intrinsic electronic properties is required. Here, using ODMR, information about the still unexplored triplet excitons in single walled semiconducting nanotubes is obtained.

Silicon carbide is better known for its durability and ruggedness than for quantum applications. It is a staple in high-power, high-temperature electronics, and routinely used as an abrasive. However, silicon vacancies in silicon carbide crystals express an interesting spin-dependent optical activity. In many aspects similar to diamond nitrogen vacancy centers, silicon carbide is talked about as an alternative for NV centers concerning quantum computing. But silicon carbide quantum defects have even more to offer: All of them are strongly influenced by a magnetic field, and some are also temperature dependent. This inspires using silicon carbide as an in-situ temperature sensor (for e.g. cellular level biological applications) and μm-size magnetometer with optical readout, without changing the fundamental device constituents. Here, the fundamental spin properties of the aforementioned defects are elucidated, and the stage for the sensing applications is set.

The manuscript starts with a detailed introduction of magnetic resonance methods and the underlying physics, followed by the description of the actual experiments. The three main subjects are presented in three chapters, with an individual in-detail introduction. Finally, a brief general summary is drawn.

2. Methods: magnetic resonance

The common denominator of the following research activities on quite distinct carbon allotropes, are the methods used to obtain this information. This chapter strives to introduce the methods of electron paramagnetic resonance (EPR) and its powerful extension, the optically detected magnetic resonance (ODMR). The latter branches into full-field and zero-field optically detected magnetic resonance, of which the full-field variety was used to obtain most of the results in this monograph.

To obtain a better overview, only the general characteristics and qualities are presented here; the more specialized variations of these methods will be introduced together with their corresponding results.

2.1. Fundamentals of electron paramagnetic resonance

2.1.1. The spin

The common ground for all magnetic resonance methods is their object of scrutiny, the **spin**. The spin, purely quantum-mechanical in nature, has no classical counterpart, and is a property of all elementary particles and atomic nuclei.

To investigate electronic properties and optical transitions, a closer look at the electron, and its spin is worthwile. Hence, the methods used here are all related to the electron spin.

A free electron, by itself, possesses a spin of $S = \frac{1}{2}$. All three main subjects of this work – semiconducting polymers, carbon nanotubes and silicon carbide defects – are however complex environments, where multiple charge carriers interact. These form a fictitious "effective", and usually higher spin. This effective spin behaves like a single spin, as far as the electron paramagnetic resonance methods are concerned, hence the wording is usually simplified to "spin".

A spin will precede around an external magnetic field, and can herein occupy $2S+1$ unique positions. For the spin triplet and quartet multiplicities that are relevant in this work, this is sketched in fig. 2.1. Here is also the first hint on the working principle of all magnetic resonance methods: The precession mode of the spins can be switched by an electromagnetic field; in case of electrons, this field is in the microwave range for typical laboratory magnetic fields up to 1T.

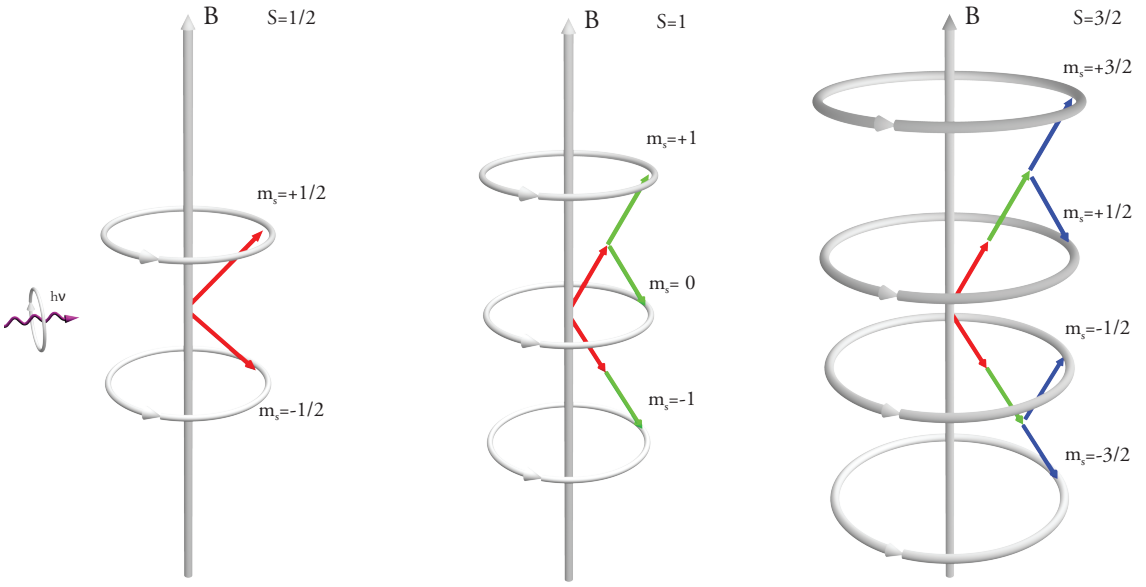

(a) $S = \frac{1}{2}$ (b) $S = 1$ (c) $S = \frac{3}{2}$

Figure 2.1.: Spin doublet, triplet and quartet in an external magnetic field. The $S = \frac{1}{2}$ doublet in **a**), a paramount example for an uninfluenced free electron, has two possible Zeeman states. The $S = 1$ triplet in **b**) has two unique spins, which can occupy three energetic states, whereas the $S = \frac{3}{2}$ in **c**) has three spins, leading to four spin states. The configuration can be changed by a resonant excitation $h\nu$; in case of electrons, $h\nu$ is in the μeV microwave range.

2.1.2. The spin Hamiltonian

The involved resonance energies of all possible EPR transitions are fully described by the spin Hamiltonian, first formulated by Abragam and Pryce [2]:

$$\mathcal{H} = \underbrace{g\mu_B \boldsymbol{S}\vec{B}}_{e^- \text{ Zeeman splitting}} + \underbrace{\boldsymbol{S}^T \boldsymbol{D} \boldsymbol{S}}_{\text{zero field interaction}} + \underbrace{\boldsymbol{S}^T \boldsymbol{A} \boldsymbol{I}}_{\text{hyperfine interaction}} - \underbrace{\boldsymbol{S}_a^T \boldsymbol{J} \boldsymbol{S}_b}_{e^-e^- \text{ exchange interaction}} - \underbrace{g_N \mu_N \vec{B}^T \boldsymbol{I}_Z}_{\text{nuclear Zeeman splitting}} + \underbrace{\boldsymbol{I}^T \boldsymbol{Q} \boldsymbol{I}}_{\text{nuclear quadrupole interaction}} \tag{2.1}$$

Tensors and both vector and scalar operators are denoted in bold. The **isotropic e^-e^- exchange interaction** $J(r) = J_0 \cdot e^{-\beta r}$ is negligible for the interaction distances considered here [3]. It is only relevant to, from the stance of this work, small interaction species, which are only marginally discussed. This also holds for silicon carbide, although the interaction ranges are larger, because the strong shielding in silicon carbide still allows an almost perfect point dipole approximation. This is corroborated by the absent rhombicity of the zero field interaction in silicon carbide. An example where the isotropic exchange interaction could play a role are the polaron pairs in organics, and the nearly free charge carrier continuum

in carbon nanotubes. As these species' spectral contributions can not be deconvolved in the ODMR spectra presented here, the exchange interaction is not further considered.

The **nuclear Zeeman interaction** can also be disregarded, as its strength, governed by $\mu_N = \frac{1}{1836}\mu_B$, is marginalized by the hyperfine interaction.

Finally, the **nuclear quadrupole interaction** is only relevant for interactions with $I > \frac{1}{2}$ nuclei, which is not the case with the main antagonists of this manuscript, carbon and silicon.

The important contributions to the measurements presented herein are the Zeeman splitting, the dipolar **zero field interaction** and the **hyperfine interaction**. These will be discussed in detail in the following chapter.

2.1.3. The Zeeman splitting and resonant transitions

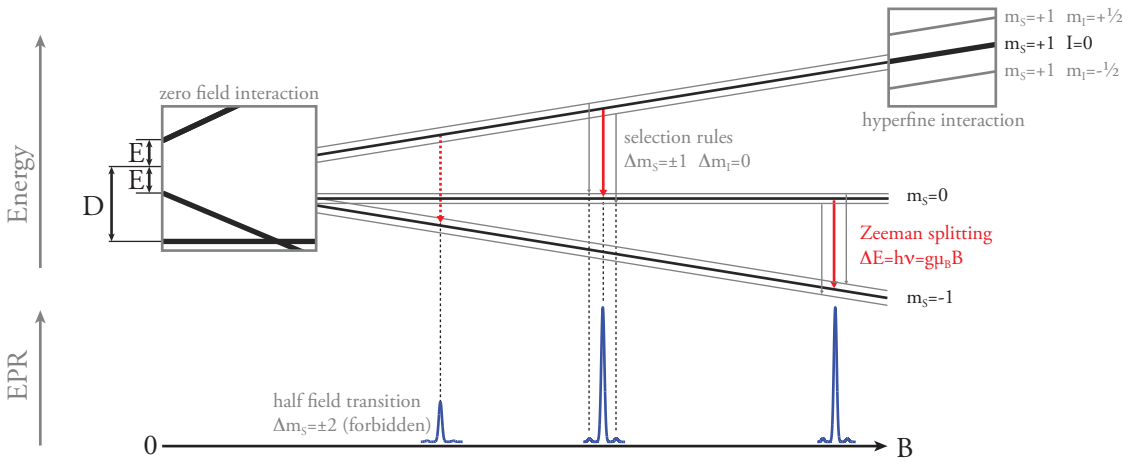

Figure 2.2.: Overview over Zeeman splitting (ch. 2.1.3), zero field (ch. 2.1.4) and hyperfine interaction (ch. 2.1.9) on an exemplary triplet spin system. The zero field splitting is rhombic $D \neq E > 0$, the corresponding forbidden $\Delta m_S = \pm 2$ half field transition is superelevated to be visible. The spin sublevels due to hyperfine interaction are generated by a mixture of $I = 0$ and $I = 1/2$ nuclei, which is common for isotope mixtures. The HFI is only shown in the high field approximation. The simulated spectra of the transitions were created assuming the natural abundance of silicon isotopes.

The splitting of optical spectra in a magnetic field was discovered by Pieter Zeeman already in the late 18th century [4]. The famous Stern-Gerlach experiment then supplied the explanation for this splitting [5]. 20 years later, the second world war fueled the development of radar technology, and consequently of microwave equipment. This enabled Yevgeny Zavoisky to build the first EPR spectrometer, which recorded the microwave absorption when inducing a spin transition between Zeeman levels [6].

The Zeeman splitting of the participating spin states is described by the corresponding term in the Abragam-Pryce-Hamiltonian.

$$\mathcal{H} = \boxed{\boldsymbol{g}\mu_B \boldsymbol{S}\vec{B}} \tag{2.2}$$

The eigenstates of this system are all possible $2S+1$ spin configurations, while the eigenenergies are defined by

$$E_{|S,m_S\rangle} = m_S \cdot \boldsymbol{g}\mu_B\vec{B} \tag{2.3}$$

In these equations, the gyromagnetic ratio ($g\,\mu_B$) consists of the Bohr magneton μ_B, which is the ground state quantised magnetic moment, and the Landé- or g-factor, which amounts to $g = 2.00231930436153$ for free electrons. m_S is the magnetic z-projection of $\boldsymbol{S}$, the spin quantum number of the spin state, and B the directional external magnetic field. E.g. for a triplet, the complete system looks as follows:

$$|1,+1\rangle \quad : \quad E_{|1,+1\rangle} = +1\boldsymbol{g}\mu_B\vec{B} \tag{2.4a}$$

$$|1,\ \ 0\rangle \quad : \quad E_{|1,0\rangle} = 0 \tag{2.4b}$$

$$|1,-1\rangle \quad : \quad E_{|1,-1\rangle} = -1\boldsymbol{g}\mu_B\vec{B} \tag{2.4c}$$

The transition energy, and hence the EPR resonance condition, for the dipole allowed $\Delta m_s = \pm 1$ transition (e.g. $|1,-1\rangle \longleftrightarrow |1,0\rangle$), amounts to:

$$\Delta E = \boldsymbol{g}\mu_B\vec{B} = h\nu_{\text{microwave}} \tag{2.5}$$

When this condition is fullfilled, transitions between spin states can be induced which leads to a detectable absorption or emission in the microwave field.

The position of this resonance condition is governed by the only intrinsic variable in this equation, the g-factor. The g-factor describes the atomic environment of the scrutinized species. The deviation from the free electrons g-factor is due to local magnetic fields superimposing the external field $\vec{B}$; these could stem from the magnetic moment of a spin-orbit-coupling, or from a crystal field. In solid states, this deviation is rather small, but commonly anisotropic. Therefore the g-factor has to be extended to a 3x3 tensor of second order. This tensor is always diagonalisable and can therefore be described by three components $\boldsymbol{g} = (g_{xx}, g_{yy}, g_{zz})$.

In this work, the exact position and anisotropy of the g-factor are small in comparison to the observed linewidths and the widths of zero field interaction, and to a lesser degree, of hyperfine interaction. Therefore the g-factor is mostly assumed to be isotropic.

2.1.4. Zero field interaction D

Without an external magnetic field, the magnetic sublevels of a spin state with an arbitrary multiplicity should be degenerate. In real molecules, this is usually not the case, and this is due to the zero field interaction (ZFI). Two effects can give rise to a ZFI: spin-orbit coupling of ground and excited state, and anisotropic dipolar interaction of the participating spins.

The dipole-dipole zero field interaction stems from the Coulomb field of two dipole moments in spatial vicinity. The classical magnetic flux density

$$\vec{B}(\vec{r}) = \frac{\mu_0}{4\pi}\left(\frac{3\vec{r}(\boldsymbol{m}\cdot\vec{r})}{r^5} - \frac{\boldsymbol{m}}{r^3}\right) \tag{2.6}$$

can be translated into its quantum mechanical equivalent with spin magnetic moments $\boldsymbol{S}$ instead of classical magnetic moments $\boldsymbol{m}$ [7].

$$\mathscr{H}_{\mathrm{ZFI}} = \frac{g_e^2\alpha^2}{8}\sum_{i\neq j}\left(\frac{\boldsymbol{S}_i\boldsymbol{S}_j}{r_{ij}^3} - \frac{3\boldsymbol{S}_i\vec{r}_{ij}\cdot\boldsymbol{S}_j\vec{r}_{ij}}{r_{ij}^5}\right) \tag{2.7}$$

Introducing an effective Spin $S = S_i + S_j$, this equation can be contracted into the already known tensor form

$$\mathscr{H}_{\mathrm{ZFI}} = \boldsymbol{SDS} \tag{2.8}$$

This tensor form can now also be used for higher spin systems, with the effective spin $\boldsymbol{S} = \sum_k \boldsymbol{S_k}$. It looks as follows:

$$\mathbf{D} = \begin{pmatrix} D_{xx} & 0 & 0 \\ 0 & D_{yy} & 0 \\ 0 & 0 & D_{zz} \end{pmatrix} = \begin{pmatrix} \frac{1}{3}D - E & 0 & 0 \\ 0 & \frac{1}{3}D + E & 0 \\ 0 & 0 & -\frac{2}{3}D \end{pmatrix} \tag{2.9}$$

With a diagonalized ZFS tensor $\boldsymbol{D}$, eqn. 2.8 can be expanded to

$$\mathscr{H}_{\mathrm{ZFS}} = D\left(S_z^2 - \frac{1}{3}S(S+1)\right) + E\left(S_x^2 - S_y^2\right) \tag{2.10}$$

With eqn. 2.10, the zero field interaction can be thoroughly described by the paramenters D and E, in a coordinate system where $0 \leq \frac{E}{D} \leq \frac{1}{3}$. Please note the difference of the ZFI tensor $\boldsymbol{D}$ and its parameter D.

2.1.5. Axial and rhombic zero field splitting

In a triplet system, the D parameter describes an axial anisotropy of the zero field interaction, which lifts the degeneracy between $|1,0\rangle$ and the $|1,\pm1\rangle$ manifold. The electron distribution is flattened along the z-axis in the sample coordinate system. The E parameter now introduces

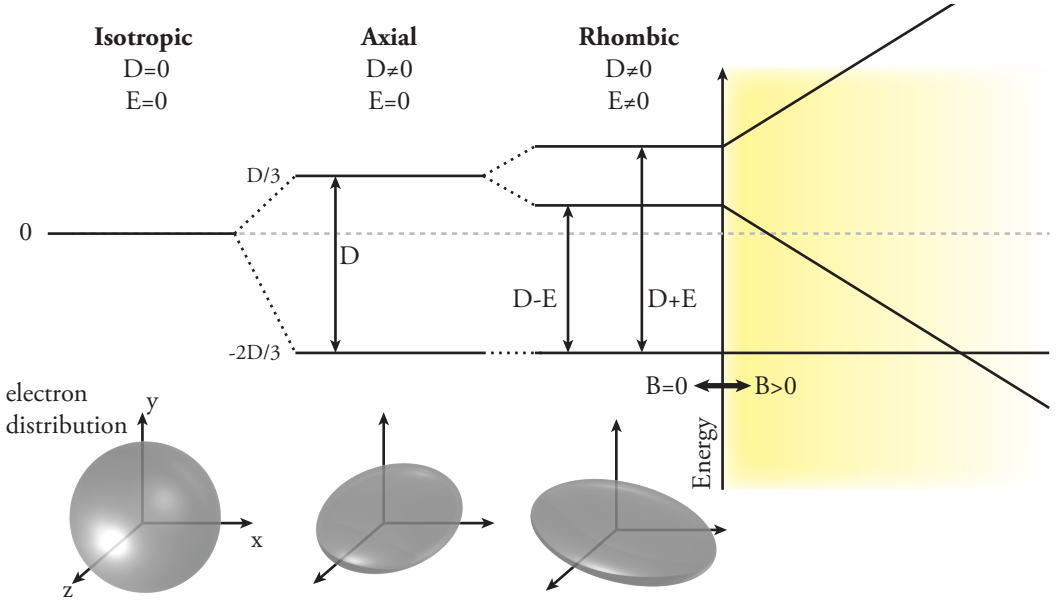

Figure 2.3.: Energy diagram of triplet sublevels in zero field and under Zeeman splitting conditions.

a rhombic anisotropy, additionally elongating the electron distribution along the x-axis [8]. In fig. 2.3 the influence of the parameters on the zero field splitting are shown. Under influence of an external magnetic field, the Zeeman splitting is added to the ZFI splitting. Also, the coordinate system is not arbitrary any more, and the parameters gain an angular dependence, linking the external magnetic field coordinate system to the aforementioned sample system:

$$D = D_0 \left(\cos^2 \vartheta - 1/3\right) \tag{2.11a}$$

$$E = E_0 \sin^2 \vartheta \cos(2\phi) \tag{2.11b}$$

This influence of the rotation of $\vec{B}$ against the sample molecular or crystal axis (also called c-axis) is depicted in fig. 2.4a. In highly oriented samples, the shown spectrum at a certain angle can be measured directly (see ch. 5.9.1. In anisotropic, unoriented samples, all transitions from all possible Euler angles are summed, and lead to the also shown **powder spectrum**.

Until now, the high spin systems were represented by an exemplary triplet. In principle, all equations are valid regardless of the multiplicity of the spin systems. However, there are some fundamental differences between integer spin systems ($S = 1, 2, \ldots$) and half-integer systems, so-called Kramers systems. The Kramers systems split into Kramers doublets, which are the $m_S = \pm\{\frac{1}{2}, \frac{3}{2}, \ldots, S\}$ spin manifolds. A Kramers doublet is always degenerate at zero field, regardless of the rhombicity of the system.

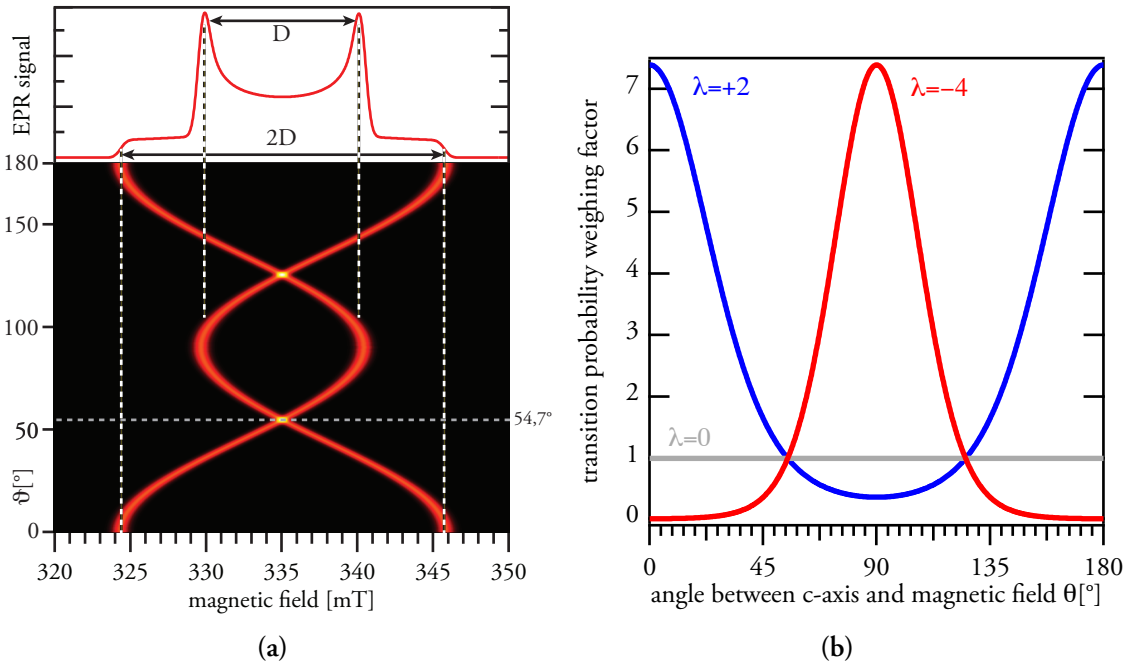

Figure 2.4.: a) (**bottom**) EPR response of a highly oriented triplet system when sweeping ϑ of the three Euler angles (ϑ, ϕ, χ). At the "magic angle" $\vartheta = 54.7°$ all transition are superimposed. (**top**) Powder spectrum for an unoriented sample, obtained by summing the spectra for all possible Euler angles. **b)** The ordering parameter governs whether sample orientations parallel $(0°, 180°)$ or perpendicular $(90°)$ to the magnetic field axis are included in the powder spectrum summation.

2.1.6. Partially ordered samples

For samples which are neither highly crystalline nor completely unoriented, a compromise between summed powder and oriented spectra has to be found. Especially when ordering of paramagnetic centers in a plane is probable, as it is expected for very thin organic and carbon nanotube samples, the following approach is viable.

The simulated spectra are computed by weighing the transition probability for a certain orientation with a factor that is depending how much this orientation is aligned with the paramagnetic center c-axis. This is expressed by an ordering parameter λ, which influences the calculation of the transition probability as follows:

$$P(\vartheta) = e^{\frac{\lambda}{2}\left(3\cos^2\vartheta - 1\right)} \tag{2.12}$$

This equation is unintuitive at first glance. For a better understanding, consider fig. 2.4b. At negative ordering parameters $\lambda < 0$, the paramagnetic centers are rather ordered perpendicular to the external magnetic field, while $\lambda > 0$ means an inclination of the centers to the field. At $\lambda = 0$, all orientations are equal, yielding a powder spectrum. The higher the value

of the parameter, the sharper the weighting peaks get, describing a higher degree of ordering. This can equivalently be done for an ordering for the ϕ Euler angle. For an application, see ch. 4.4.1.

2.1.7. The half field transition

The half field transition is the first-order forbidden dipole transition with $\Delta m_S = \pm 2$, which is spectrally situated at the double g-factor of the principal $\Delta m_S = \pm 1$ transitions. In the materials shown here, the half field transition is usually at $g \approx 4$. Due to its forbidden nature, the amplitude of this transition is very weak, and usually does not allow for spectral deconvolution. However, its mere presence is a very clear and undisputable qualitative argument for a high spin system.

2.1.8. The magnetic tape measure – estimating distances from EPR

The zero field interaction is in essence derived from the classical dipole external magnetic field. This application of the correspondence principle allows, inversely, to deduct a classical spatial parameter r from the quantum mechanical D tensor. This r describes the spatial extent for the charge carrier distribution comprising the spin system.

However, some assumptions have to be made. First, the ZFI should be mainly dipolar in nature, with a negligible contribution from spin-orbit coupling [9]. Second, the spin system used in the ZFI Hamiltonian is a fictitious effective spin system, which only describes a median point of the real charge carrier distribution [10]. Especially for $S > 1$ spin systems, the approximation of two point dipoles does not apply, hence the calculated values should be used considering a large uncertainty. Especially in systems with large delocalizations (e.g. conjugated polymers), the delocalization of the spin weakens the point-dipole approximation and leads to overestimation of D and hence, to underestimation of the calculated interspin distance values [11].

With this in mind, the estimation of the spatial extent can be an important tool to assign a certain species to a corresponding real space substructure, or to compare classical effects like thermal expansion to their repercussions in the quantum world.

Consider the individual parameters of equations 2.7 and 2.10:

$$D = \frac{3}{4}(g\mu_B)^2 \left\langle \frac{r^2 - 3z^2}{r^5} \right\rangle \tag{2.13a}$$

$$E = \frac{3}{4}(g\mu_B)^2 \left\langle \frac{y^2 - 3z^2}{r^5} \right\rangle \tag{2.13b}$$

with r as the charge carrier distance, and z is the component parallel to the crystal c-axis. If the zero field Hamiltonian is axial ($E = 0$), we can assume

$$\left(\frac{r^2 - 3z^2}{r^5}\right) \leq \frac{1}{r^3} \tag{2.14}$$

and then solve eqn. 2.13a for r [12]:

$$r = (3/4 g\,\mu_B)^{\frac{1}{3}} \cdot \left(D[\mathrm{Hz}] \cdot 10^7 h \cdot g\,\mu_B\right)^{-\frac{1}{3}} \tag{2.15}$$

E.g. for an axial spin triplet with $D = 1000$MHz, the paramagnetic center distance is $r \approx 3.9\mathring{A}$. For a weaker splitting $D = 100$MHz, the interaction is weaker, and consequently the distance $r \approx 7.3\mathring{A}$ is larger.

2.1.9. The hyperfine interaction

The hyperfine interaction matters when a spin system is influenced by nuclei with $I \neq 0$. Analogously to the electron Zeeman interaction, it splits one Zeeman level into $2I + 1$ sublevels, with an energy shift of

$$\Delta E_{\mathrm{HFI}} = g_e \mu_B \boldsymbol{A} m_I \tag{2.16}$$

with the hyperfine interaction tensor $\boldsymbol{A}$ and the nuclear magnetic quantum number m_I. The effect of the HFI on the energy levels is shown on fig. 2.2. If the HFI tensor $\boldsymbol{A}$ is isotropic, the observed charge carrier resides at the location of the nucleus. If it is anisotropic, charge carrier and nucleus are distant, and the HFI is mediated again by dipolar interaction [13].

2.1.10. Line broadening

The lineshape of EPR transitions is governed by two mechanisms. All quantum transitions, be they optical or EPR, are subject to **homogeneous broadening**. This natural linewidth is due to the uncertainty of the involved transition energies, which create a Lorentz-shaped broadening of the ideal monochromatic emission. The energy uncertainty of the involved levels is

$$\delta E \approx \frac{\hbar}{\tau} \tag{2.17}$$

with the spontaneous decay lifetime τ. In EPR, this lifetime broadening is increased when large incident microwave power induces stimulated emission, thus further reducing the lifetime. This phenomenon is called **saturation broadening**.

The second mechanism is the **inhomogeneous broadening**, manifesting as a gauss-shaped broadening of the EPR lines. There is a multitude of underlying reasons for the inhomogeneous broadening:

- **Unresolved hyperfine interactions** are analogous to the HFI introduced in ch. 2.1.9. With a large number of statistically dispersed surrounding nuclei, the HFI resonance peaks are averaged, and only a gaussian-broadened envelope can be recorded.

- **Overmodulation** of the magnetic field happens when the magnetic field modulation used in EPR lock-in signal recovery is large in comparison to the linewidth.

- **Unresolved zero field interaction** is, like the unresolved HFI, due to zero field interactions (ch. 2.1.4) with a splitting in the order of the natural linewidth. The D cannot be resolved, but increases the linewidth of the observed resonance. This is assumed to happen with the polaron peak resonance observed in organic materials and nanotubes.

In the simulations shown here, these two broadenings are then convolved with all calculated resonance positions, yielding an envelope profile to create a best match to the experimental results. This necessitates the assumption, that all broadening mechanisms are isotropic in nature. However, to fully describe a spin system, anisotropic *strains* for the $\boldsymbol{g}$-Tensor, the HFI $\boldsymbol{A}$-Tensor and the ZFI $\boldsymbol{D}$-Tensor, have to be considered. As the interaction tensors, especially $\boldsymbol{D}$, discussed in this work are much larger than the linewidths, the simpler isotropic broadening was used.

2.2. Optically detected magnetic resonance (ODMR)

Until now, the EPR conditions were shown in a generalized way, without catering to the exact mechanism of signal generation. In classic EPR, the observable is the microwave absorption, or rather, the deviation of the microwave absorption under EPR conditions. However, most of this work was done taking a detour from this direct observation of microwave-induced transitions: In optically detected magnetic resonance, or, in short, ODMR, the observable is the variation of the intensity of an optical transition under EPR conditions. Please note that ODMR does not directly measure the optical transition energy variation between the individual Zeeman states. Under EPR conditions, populations of the participating Zeeman substates are equalized. If we assume different population or depopulation rates for the Zeeman sublevels, it should influence the rate for the optical transition, leading to a variation of photoluminescence (PL) intensity.

As the generation mechanism for the three researched material classes in this work differ, only a rough overview will be presented here. The individual excitation pathways will then be discussed in the material classes chapters.

2.2.1. ODMR signal genesis

The common denominator for all models for the ODMR signal genesis is the modulation of microwave range spin substate transitions, which couple to the observed optical transition via different rates. In simple terms, an EPR resonance condition means an open path between spin substates, activating a different optical transition rate, which in turn leads to a modulation of the optical transition's intensity (i.e. photoluminescence).

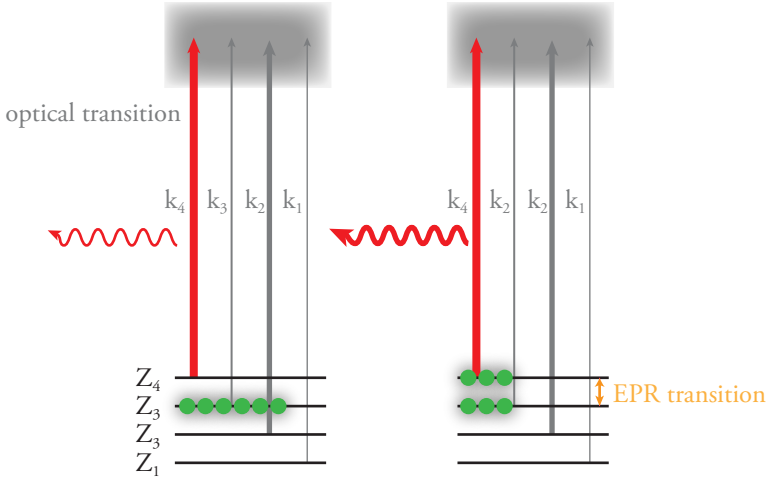

Figure 2.5.: Generalized ODMR working principle. An arbitrary spin system with 4 substates $Z_{1...4}$ has 4 different rates $k_{1...4}$ connecting it to the optical transitions. Assume a preferential population of the Z_3 state, which has a small influence on optical transitions. If we now open a pathway between Z_3 and Z_4, the optical intensity increases, as the population of Z_3 can feed the k_4 transition.

How the ODMR effect in an actual material system is created, depends on the excitation kinetics of the system. For excitonic systems where the detection is in the singlet manifold, and the magnetic resonance manipulation in the excited triplet manifold, there are three models. In this work, concerning the localized triplets in organic photovoltaics and single walled carbon nanotubes, the **triplet-triplet annihilation** model is favored and will be introduced in more detail. The competing models are the **ground state depletion** model, which is responsible for the ODMR in diamond NV centers [14] and defects in silicon carbide; and finally, the **triplet polaron quenching** model, which could be responsible for the $g = 2$ polaron pair peaks and the initial generation of the localized triplets [15] (see also fig. 2.6).

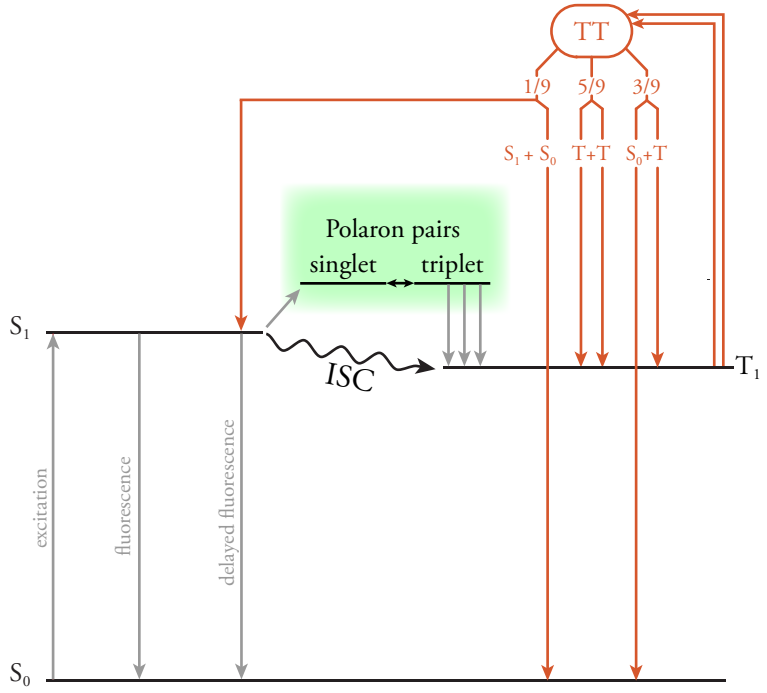

Figure 2.6.: Triplet-triplet-annihilation in a singlet-triplet excitonic system. In orange are all mechanisms concerning TTA, the green box depicts the triplet-polaron-quenching which could be responsible for the polaron pair peak, and also be an alternative to the ISC as a triplet generation pathway. S_0 is the ground state, S_1 the excited singlet, and T_1 the excited triplet.

2.2.2. Triplet-triplet-annihilation

Triplet-triplet-annihilation assumes that two non-geminate triplet excitons T meet and create a mixed (TT) state, which possesses a nine-dimensional Hilbert space [16, 17]. This mixed state is described by eigenfunctions, which can be divided into three scattering channels:

- Quintet $(T+T): |2,[-2,-1,0,+1,+2]\rangle$
- Triplet $(S_0+T): |1,[-1,0,1]\rangle$
- Singlet $(S_0+S_1): |0,0\rangle$

which are populated with the respective probabilities $\frac{5}{9}, \frac{3}{9}$ and $\frac{1}{9}$. The least probable singlet channel can then either again cross into a triplet state, or recombine under fluorescent emission. This fluorescence, as it stems from a complex triplet channel, has a much longer lifetime than regular singlet fluorescence and is therefore dubbed "delayed fluorescence". The delayed fluorescence has been postulated as being responsible for the ODMR response of molecular

crystals [16, 17, 18, 19], semiconducting polymers [15], and has been directly observed in semiconducting polymers [20] and carbon nanotubes [21].

The ODMR signal is then achieved by resonance conditions in the triplet and quintet channels, which in turn influence the rates pertaining the singlet channel and, ultimately, the delayed fluorescence. As the aforementioned scattering happens very fast, it is important to note that the resonance conditions pertains the triplets erecting the quintet channel, not the short-lived virtual quintet itself. One model cites the singlet-quintet SQ mixing of the singlet channel with the quintet's singlet-configuration [18], in analogy to the singlet-triplet mixing when observing spin-coupled radical pairs [22].

Incidentally, the relevant EPR transitions for the quintet and the originating triplets are the same [15, 23], and – neglecting the triplet-triplet interaction radius – can be phenomenologically treated like a sole triplet.

2.2.3. Simulations

The numerous simulations shown here were done with MATLAB, using the *EasySpin 4.5.5* package [24]. To simulate full field EPR and ODMR spectra, the program *pepper* was used. For non-Boltzmann equilibrium spin populations, *pepper* correctly calculates microwave absorptive and emissive curves [25]. However in ODMR, we do not observe the microwave sign, but the influence of population changes on the photoluminescence. To account for this, for ODMR simulations the microwave emissive transition was inverted.

2.3. The experiments

This section briefly describes the full field ODMR experiment and the conventional EPR machine on which it is based. For the orientation dependent experiments, an orientation independent excitation intensity, and therefore the fiber excitation is crucial. Finally, the zero field ODMR setup is introduced. As the equipment needed to investigate the different carbon allotropes slightly varies, only a rough overview of the common devices is given. Individual modifications of the setup to obtain a special result is given together with the result, as pertinent.

2.3.1. Electron paramagnetic resonance

The EPR and ODMR setups are based on a heavily modified *Bruker 200D* X-band spectrometer. The *Bruker ER4104OR* cavity is a rectangular resonator with two optical access ports, a resonance frequency of $\nu = 9.43\text{GHz}$ and a quality factor $Q \approx 3000$ when loaded. Inside the

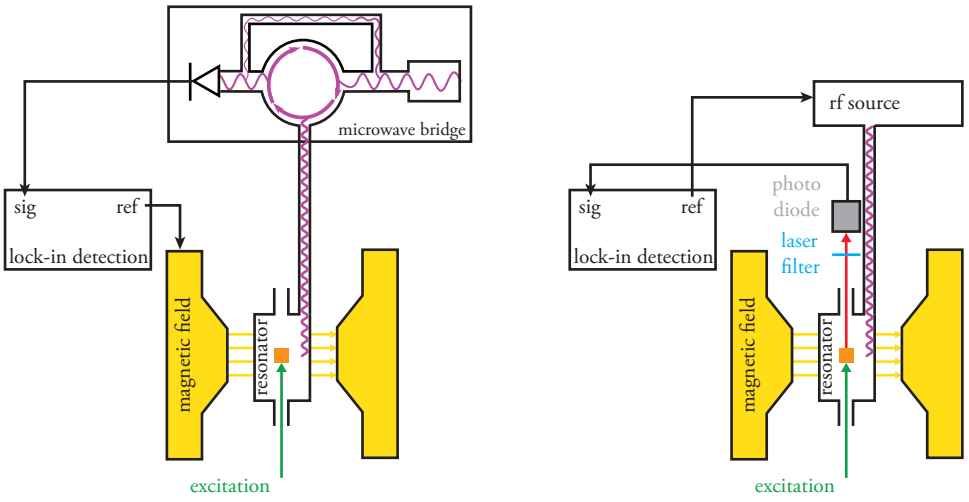

(a) EPR experiment

(b) full field ODMR experiment

Figure 2.7.: EPR and ODMR experiment schematics.

cavity, a flow cryostat *Oxford Instruments ESR900* allows sample temperatures $T = 4 \ldots 340K$, controlled by a *Lakeshore 330* PID temperature controller.

The magnetic field is controlled by a feedback loop Hall sensor with a relative precision of 0.01mT. Absolute precision of 0.001mT can be achieved with a nuclear magnetic resonance magnetometer. However in this work, the magnetic field sweep ranges are commonly very broad, which forbids an interpolation of the magnetic field from NMR magnetometer values at sweep start and stop, and the slow locking time of the magnetometer renders recording of values for every field position impractical. In combination with resonance linewidths reported here usually exceeding 1mT, the absolute magnetic field precision is neglected. Therefore, in the figures g-factor axes are left out, and only relative g-factors are discussed.

The excitation source portfolio comprises a DPSS laser with the wavelength 532nm, which is mainly used in the organic photovoltaics chapter. Two Diode lasers with 568nm and 980nm are used to excite the S_2 and S_1 transitions, respectively, of single walled carbon nanotubes. Finally, both a 780nm diode for bulk excitation of all phonon sidebands, and a tunable small bandwidth *Sacher Lion 920* laser for resonant zero phonon line excitation of silicon carbide. EPR microwave (also often dubbed RF) excitation and detection is provided by a *Bruker ER047* microwave bridge with a maximum power of 200mW. The detected microwave absorption signal feeds a lock-in amplifier, which is referenced by a 100kHz modulation of the magnetic field to maximum $\Delta B = 0.5$mT. This modulation of the measurement x-axis leads to the idiosyncratic first derivative signals of EPR, as explained in fig. 2.8a.

2.3.2. Full field ODMR

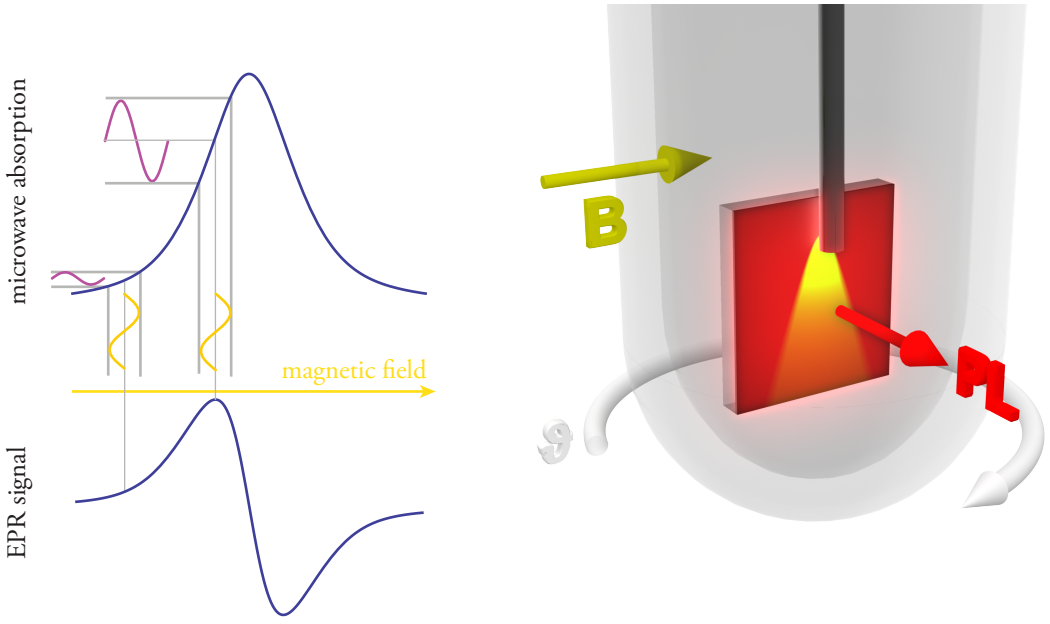

(a) first derivative EPR signal

(b) tilt independent fiber excitation

Figure 2.8.: a) Modulation of the magnetic field leads to a first derivative recorded signal. Adapted from [23]. **b)** Fluence stabilisation of the ODMR. A sample tube with a specimen on a herasil glass sheet is excited with a fiber coming from the top. The relative position of the fiber to the specimen is fixed and the excitation is independent of ϑ.

The optically detected magnetic resonance uses the same framework as EPR. The differences are the microwave excitation, which is provided by a *Wiltron 69137A* high frequency sweep generator, together with a *Microsemi* rf amplifier leading to a maximum RF output of 33dBm (2W). The photoluminescence is detected with a silicon photodiode. In between photodiode and sample, long pass filters corresponding to the excitation wavelength extinguish the excitation light.

The resonant photoluminescence variation is also recorded lock-in, however the reference is provided by toggling the microwave power (and hence, the y-axis), which delivers, in contrast to EPR, a zeroeth harmonic spectrum. As the integral photoluminescence is also recorded, ODMR signal amplitudes are usually given as relative variations $\frac{\Delta I_{\mathrm{PL}}}{I_{\mathrm{PL}}}$, also referred to as **ODMR contrast**.

2.3.3. Excitation fluence stabilization

In the conventional ODMR setup (fig. 2.7b), the laser beam is directed on the sample via the optical access port of the EPR resonator. Only when the sample surface is parallel to the

magnetic field, the laser beam hits the sample straight on. When the sample is tilted by ϑ, the excitation flux density is reduced according to Lambert's cosine law

$$I_{\text{sample}} = I_{\text{source}} \cos\vartheta \tag{2.18}$$

leading to a nonexistent excitation at $\vartheta = 90°$. Especially in systems where the ODMR response depends nonlinearly on the excitation density, i.e. systems with multimolecular processes like triplet-triplet annihilation, results obtained without adressing this issue would be unreliable. The problem was solved by introducing an airtight fiber load lock, which allows inserting an optic fiber into the EPR sample tube (fig. 2.8b). The fiber is fixed in the tube, and hence the excitation density becomes sample tilt independent. However, the grazing incidence of the excitation commands a constant, but much weaker excitation intensity than achievable by direct beam excitation. This problem is planned to be alleviated by mounting a 90° prism at the fiber tip.

2.3.4. Sample preparation

Specimens sensitive to ambient conditions, like the organic and nanotube materials, were prepared in a glovebox under a protective nitrogen atmosphere. The sample solution was drop-cast or spincoated on a *Herasil* substrate, which has a low density of para- and ferromagnetic impurities, and inserted into 4mm diameter quartz EPR sample tubes. These were flushed with helium and either fuse-welded with a residual helium atmosphere of $\approx$ 10–100mbar, or sealed with the aforementioned fiber load lock.

The silicon carbide specimens are unperturbed by ambient conditions. However, to facilitate a thermal coupling of the sample to the flow cryostat, a residual helium atmosphere was also used with silicon carbide.

2.3.5. Zero field ODMR

The zero field ODMR is integrated into a *HORIBA Labram HR* confocal raman microscope, which was also used for the photoluminescence measurements on silicon carbide. For ZF-ODMR, the microscope was only used to focus a 785nm laser excitation on the sample surface, adjacent to an thin wire acting as an antenna to couple a radio frequency into the sample. The main difference between high field and zero field ODMR is, that the magnetic field is held at zero or constant low field (up to 30mT), and the microwave frequency is swept by a *Stanford research SG384* microwave source and amplified by a solid state amplifier *Becker 20280035-T* with a maximum power output of 4W. Magnetic field for low field measurements was first provided in a very simple manner, by a fixed magnet that could be moved closer to the sample to increase the field in the xy-plane. Later, a more sophisticated variant was conceived; with

a three dimensional magnetic field provided by coils, with the coil pair in z-direction being used for the main field dependency, and the xy coils for shimming the magnetic field into the sample molecular c-axis. The ZF-ODMR is also described in [26] and [27].

3. Organic heterojunctions for photovoltaics

> *"Und wenn sich dann in einer weit entfernten Zukunft die Kohlenlager der Erde einmal erschöpfen würden, so würde die Menschheit deshalb noch lange nicht untergehen. Sie wäre frei von den Fesseln, die sie heute durch ihre Abhängigkeit von der Kohle trägt. Und leben und Kultur würden kein Ende haben, bis einst – in Jahrmillionen – die Sonne nicht mehr scheint."*
>
> *"And when, in a far future, earth's coal deposits would be depleted, humankind would not perish. It would be free from the shackles of the dependency on coal. And life and culture would not end, until – after eons – the sun stops shining"*
>
> — New ways of utilizing solar power, Frankfurter Allgemeine Zeitung , 20 July 1914

Renewable energies are, in recent years, entering the focus of public attention, and also, of legislation around the world. The German Renewable Energy Act (Erneuerbare-Energien-Gesetz), for example, targets an increase of renewable energies contribution to the overall power generation from today's 28% to above 55% in 2060. In this law, fixed feed-in tariffs are set, but there is also a set interval in which these tariffs decrease. Therefore, renewable energies technologies research and development has to keep pace to stay profitable. Conversely, there are substantiated concerns, that a localized subsidization of renewable energies leads to a global depression of fossil energy pricing, and hence, an increase of consumption in other countries; nullifying the net emission reduction [29]. Both issues – tariff reduction and net emission constancy – can be tackled by increasing the attractiveness of renewable energy sources; by creating cheap and efficient technologies, which are profitable without subsidization.

3.1. Organic photovoltaics

Especially in photovoltaics, the search for a disruptive technology alternative for the expensive silicon solar cells is on. One candidate, which had a history of fast progress in the previous years is the organic photovoltaics (OPV) approach. Here, the solar cell pn-junction is created by a

Results of this chapter are in preparation for publication [28].

mixture of organic, (hydro)carbon semiconductors [30]. Considering the ubiquity of plastic products in our daily lifes, it is not hard to imagine that production and processing of those "power plastics" are in principle more cost effective and scalable than their inorganic competitors. Despite these principal advantages of the OPV approach, some serious issues hampered a significant market penetration until this day, except for off-grid niche applications [31]. Among those are the still modest power conversion efficiencies (PCE) of 11.1% [32], and the limited stability of even expensively encapsulated devices. On both issues, electron paramagnetic resonance is a proven tool to help elucidating the underlying fundamental processes. Especially high spin states – in this case – triplets, are playing an important role when discussing accelerated material aging and exciton quenching. For example, EPR in conjunction with ODMR has proven a rapid degeneration path by activating triplet oxygen by energy transfer from the P3HT donor triplet [33].

3.2. Excitations in semiconducting organic materials

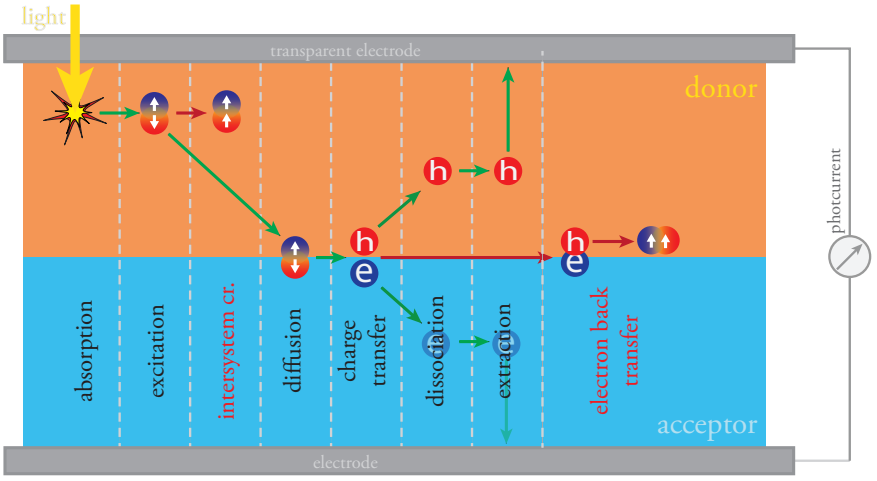

Figure 3.1.: Simplified kinetic diagram of a bilayer organic solar cells. The green arrows depict the way to the photocurrent; the red arrows potential loss mechanisms or recombination.

Organic semiconductors have some similarities to classical semiconductors. Their valence band equivalent, the highest occupied molecular orbital (HOMO), and their conduction band equivalent, the lowest unoccupied molecular orbital (LUMO), are created by their alternating single and double bond. Semiconducting polymers are sp^2 hybridized, and the strong σ-bond does not participate in conduction. The p_z orbitals, however, are only weakly bound and create a conjugated π-electron system. According to the SSH-Model by Su, Schrieffer

and Heeger [34], the Peierls-Distortion lifts the twofold degeneracy of the one-dimensional polymer chain, giving rise to a π-Band (HOMO), and the π^*-Band (LUMO).

Please consider Fig. 3.1. From the conversion efficiency point of view, a perfect excitation pathway (green arrows) would be as follows: An excitation by light with an energy larger than the HOMO-LUMO gap results in a strongly Coulomb-bound electron-hole pair. If this pair is localized, it is called a Frenkel exciton, if it is delocalized over the molecule, it is called Wannier-Mott exciton. This exciton can now diffuse to a real space interface between a polymer donor and an electronegative acceptor (in this work, only fullerenes are considered), the exciton can and transfer its electron to the acceptor [35]. This still bound charge carrier pair is, in literature, dubbed either **charge transfer state/complex**, or very commonly **polaron pair**, described as a charge carrier pair dressed by a corresponding lattice vibration of the donor polymer [36] or the acceptor fullerene [37]. This polaron pair can then dissociate into free charge carriers, which can be extracted at their corresponding electrode, creating the solar cell's photocurrent.

However, there are different loss pathways, where an excitation does not culminate in a photocurrent. Directly after excitations, there is direct **radiative recombination** of the exciton, under emission of photoluminescence; **nonradiative recombination** [38], and finally, the **intersystem crossing** of the exciton into a triplet state, which can be observed by EPR.

If none of these happened and a polaron pair was formed, the very same can instantaneously recombine geminately, with none to very low luminescence emission. A geminate recombination is always spin-preserving, and as spin singlet hence not accessible from EPR methods. In systems where the acceptor's LUMO level is close to the donor's triplet level, an **electron back transfer** from the acceptor to the donor triplet can also be discussed.

Now, after successful dissociation of the polaron pair, the individual charge carriers can, with other free charge carriers, non-geminately recombine into a polaron pair [39], which obeys a spin statistic with a triplet:singlet ratio of $3:1$ [40]. These triplet polaron pairs can be manipulated and observed with EPR, and especially ODMR [41].

The aforementioned triplet excitons are detrimental to the photovoltaic device perfomance, as the longer-lived triplet excitons act as a trap for states which would otherwise participate in photocurrent generation. Hence, knowledge of the nature and kinetics of triplet excitons in OPV are of fundamental interest.

EPR is an apt tool to obtain this knowledge, as it is in principle sensitive to free charge carriers ($S = \frac{1}{2}$), to polaron pairs if it they possess a triplet configuration (loosely bound $S = 1$), and to localized triplet excitons. However, the signals of polaron pairs and triplets are weak, and they can be more easily accessed by the more sensitive ODMR (see ch. 2.2).

3.3. ODMR deconvolution of organic donors

Monocrystalline, or on the other hand, perfectly anisotropic materials are easy to characterize in EPR, as their spectral characteristics can either be directly read from the spectrum, or in the case of an anisotropic powder spectrum, easily deconvolved in a simulation (fig. 2.4a). Semiconductors for OPV are, however, partially ordered by design, as a certain degree of crystallinity proves to be advantageous for their transport performance [42]. This leads to a high variability of the ODMR spectral shape even for one material. These spectra for partially ordered materials are henceforth called pseudo-powder spectra.

It has to be kept in mind that the spatial extent of the species to which ODMR is sensitive to is 1–20$\mathring{A}$ (see ch. 2.1.8). E.g. one thiophene unit cell measures already 3.9$\mathring{A}$ in size. Together with conjugation lengths starting from 20 units, reaching above 100 units [43], the mesoscopic morphology scale of the polythiophene far exceeds the ODMR scope.

Therefore, the intrinsic exciton parameters, like the zero field splitting D, E, and hence the ODMR stationary points (turning points), are not governed by the morphology. The plane and c-axis of the excitons, however, are depending on the ordering and orientation of the material. Therefore, signal shape and amplitude can change with different morphology and laboratory systems, leading to ambiguity of the curves spin nature, multiplicity and rhombicity.

3.3.1. Different kinds of molecular ordering

OPV active layers are commonly only few hundreds of nanometers thick. Together with the aforementioned length and hence, large aspect ratio of semiconducting polymers, a certain preference for the polymer conjugation unit's long axis ($\neq$ c-axis) to be parallel to the sample surface can be surmised. The second constrain that pertains many polymers is that they either stack preferentially with the molecule backbone lying down on the surface (face-on), or standing up (edge-on), as depicted in fig. 3.2.

An important difference concerning the full field ODMR method is that in

- **face-on configuration**, the molecular plane is parallel to the sample surface, and the c-axis is orthogonal. This means that when the magnetic field is parallel to the sample surface $\Rightarrow$ the magnetic field is perpendicular to *all* molecular c-axes, regardless on their long axis orientation on the sample. Inversely, when the magnetic field is perpendicular to the sample surface, again *all* c-axes are parallel to B. Consider the Euler angles in this system: Here, no preferential ordering of one ϕ direction exists, the ordering pertains only the angle ϑ between sample surface and magnetic field.

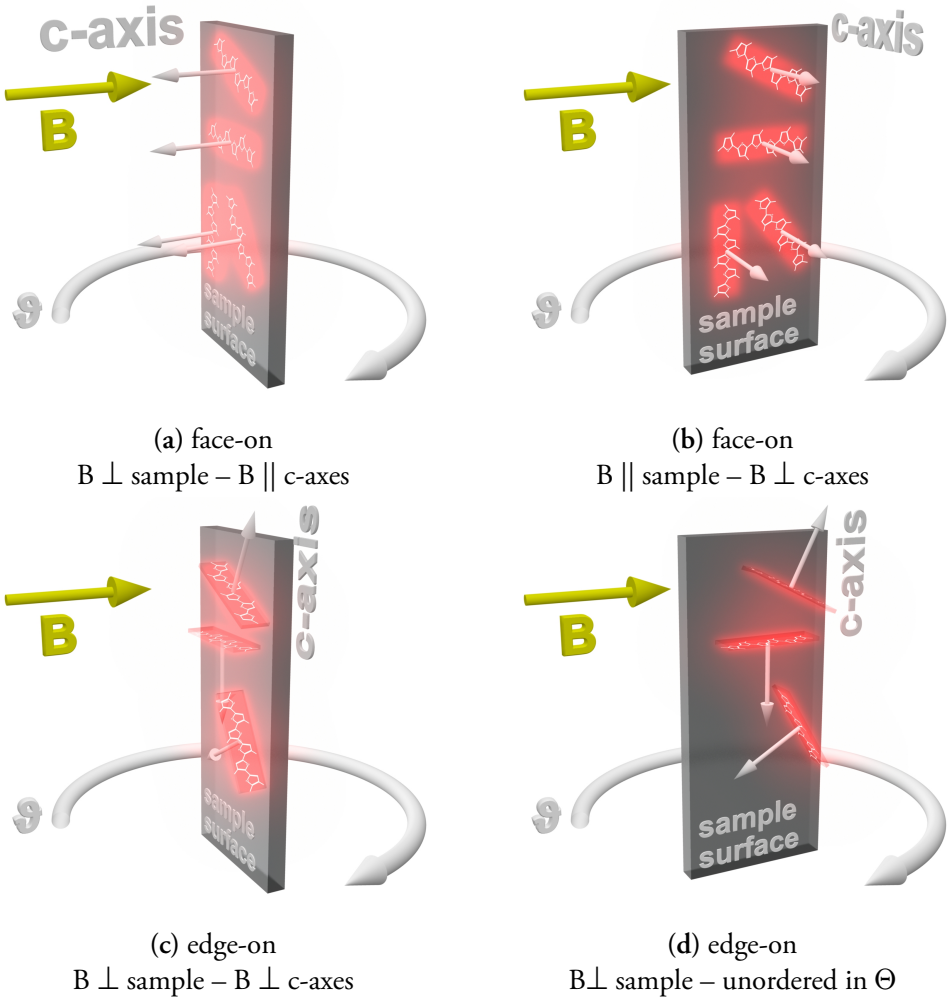

(**a**) face-on
B ⊥ sample – B || c-axes

(**b**) face-on
B || sample – B ⊥ c-axes

(**c**) edge-on
B ⊥ sample – B ⊥ c-axes

(**d**) edge-on
B⊥ sample – unordered in Θ

Figure 3.2.: Edge-on and face-on configurations under different sample angles ϑ. Please note that the sample rotation angle ϑ and the Euler angle Θ are not necessarily identical, especially when the sample is oriented in the Euler angle ϕ. For the edge-on behaviour, see also fig. 4.7 concerning nanotubes.

- **edge-on configuration**, the c-axes are parallel to the sample surface. However in this plane, they are completely anisotropic. This means that only at B⊥sample surface, *all* c-axes are perpendicular to B. In all other orientations, a fraction is parallel, and another perpendicular. This is similar to the situation with carbon nanotubes explained in ch. 4.4.1. Here, from the viewpoint of the magnetic field, due to the aforementioned reduced dimensionality because of the sample thinness, the ordering along the Euler angle ϕ plays a role in addition to the ordering along ϑ, complicating the ODMR spectral deconvolution. In fig. 3.2d), it becomes clear why we have to include a ϕ-ordering. Consider the Euler angles: The c-axes here are averaged in all possible ϑ-angles, but only after rotating ϕ by either 0° or 180°.

This means that in edge-on configurations, we can expect a singularity spectrum at B⊥sample surface, and pseudo-powder spectra for the other orientations, and in face-on configurations, defined spectra for B⊥sample and for B||sample.

3.3.2. Polythiophene

Poly(3-hexylthiophene) (P3HT) is one of the classics in organic photovoltaics. A p-type semiconductor, its for a second generation polymer, comparatively high stability [33], together with its modest power conversion efficiencies made P3HT one of second generation OPV's workhorses. The simple processing and ready availability also established P3HT together with $PC_{60}BM$ as one of the most in-depth researched bulk heterojunction OPV systems.

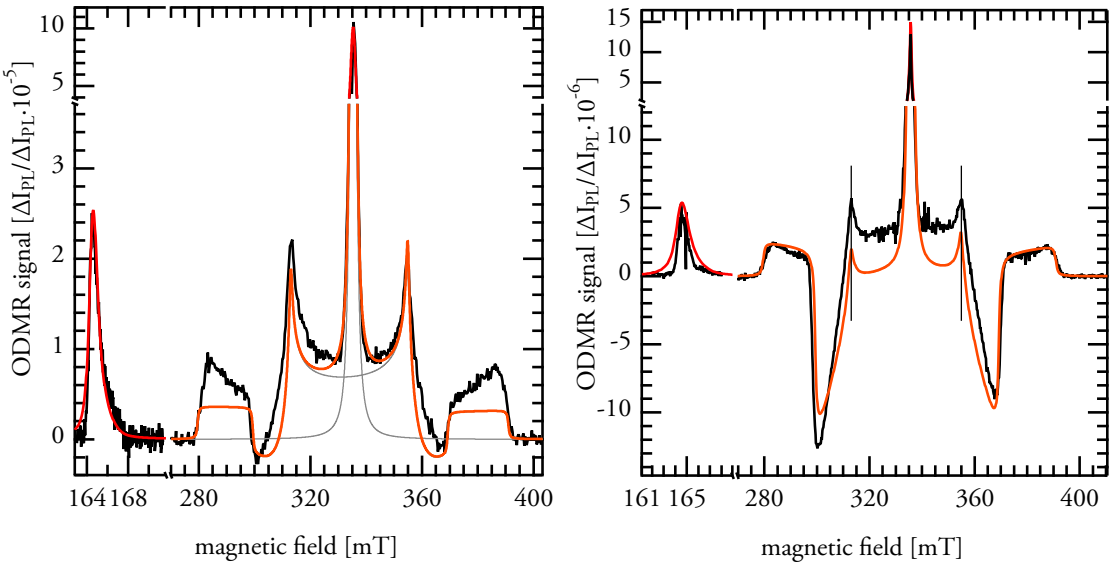

(a) P3HT 2009-06-30 (b) P3HT 2009-09-08

Figure 3.3.: ODMR of P3HT. Both curves have been deconvolved with two $S = 1$ triplet spin systems, with $D_{T_1} = 1530$MHz, $E_{T_1} = 130$MHz and $D_{T_2} = E_{T_2} = 0$. The individual constituents of the simulation are depicted in grey, and summed in the red curve. The simulation of **a**) was calculated with an ordering parameter of $\lambda_\phi = 1.3$, **b**) with $\lambda_\phi = -0.2$. The linewidths are considered unimportant, as they cannot be ascertained in a broad pseudopowder spectrum. Temperature $T = 5$K.

The ODMR spectrum of P3HT, shown in fig. 3.3 is not trivial. It is dangerous to, after scrutinizing the spectrum, just assume stationary points to ascertain D and E. A very simple approach would be to assign the peak at $g \approx 2$ (335mT) to a triplet with $D = 0$, and the broad "wing"-like signature to an axial triplet, and read the outermost turning points to obtain $2D$.

This was done by Swanson et al. in [44], where the first ODMR of P3HT was observed. They assume an axial triplet with $D = 1569\text{MHz}, E = 0$ to give rise to the full field signature. These values are not correct.

P3HT orders itself edge-on on the substrate in thin films [45]; this has been also shown specifically for this sample by x-ray diffractometry measurements carried out by K. Topczak in [46]. Therefore, the ODMR spectral deconvolution of the spectra shown in fig. 3.3 has to consider an ordering both in Θ and ϕ directions. The shown spectra are from two different sample of Sepiolid P200 P3HT. The simulations matching both spectra were done with identical ZFS parameters for two $S = 1$ triplets $D_{T_1} = 1530\text{MHz}$, $E_{T_1} = 130\text{MHz}$ and $D_{T_2} = E_{T_2} = 0$. The difference in spectral shape was accounted for by using an ordering (ch. 2.1.6) in ϕ-direction. The changing sign of the resonant PL enhancement in the T_1 triplet signature is caused by a non-Boltzmann population of the spin substates, with the population order from lowest to hightest $|1,-1\rangle, |1,0\rangle, |1,+1\rangle$. A non-equilibrium population is to be expected when assuming triplet-triplet-annihilation as signal generation path.

The simulations are not a perfect match, however the stationary points are now described much better than in the literature [44]. To further improve this, both ϑ and ϕ-ordering have to be accounted for simultaneously, which was not possible at the time of publication.

The rhombicity of the P3HT triplet renders a precise calculation of the triplet extent according to ch. 2.1.8 impossible. However, we can still tentatively compute the extent for the axial part of the ZFS-Tensor, which amounts to $r = 3\mathring{A}$. This value, together with the fact that the ZFS-Parameters are identical for different samples, and hence independent of morphological variations, corroborated the long-standing working model of the triplet exciton having a high degree of localization on one thiophene ring. However, previous conjectures of multiple intra-chain and interchain triplets in [23] and [46] are discarded, as they are unnecessary to explain the P3HT ODMR spectrum.

Interesting supplementary measurements would be on a sample with P3HT on a nickel oxide layer, as it changes the P3HT configuration to preferentially face on [47].

3.3.3. PTB7

The thienothiophene derivative PTB7 – chemical structure shown in fig. 3.4 – is a third generation donor-acceptor block copolymer with a low bandgap of $E_g = 1.8\text{eV}$ [48]. In comparison with second generation donor polymers like P3HT, its low energy gap improves PTB7's absorption at longer wavelengths up to 800nm. In conjunction with the fullerene $PC_{70}BM$ as acceptor, PTB7 yields reproducible power conversion efficiencies of above 9% [49]. Another advantage concerning charge carrier transport is the expected face-on stacking configuration of PTB7 [50]. The face-on configuration should also reflect in the ODMR, according to ch. 3.3.1. The ODMR curves for 0° and 70° are shown in fig. 3.5. As the fluence stabilized

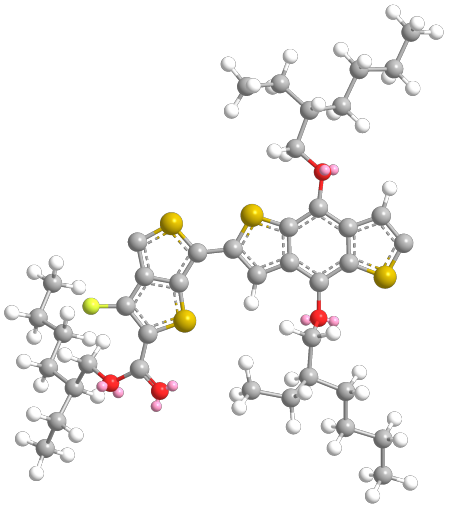

Figure 3.4.: Chemical structure of PTB7, full name Poly[[4,8-bis[(2-ethylhexyl)oxy]benzo[1,2-b:4,5-b']dithiophene-2,6-diyl][3-fluoro-2-[(2-ethylhexyl)carbonyl]thieno[3,4-b]thiophenediyl]].

excitation (ch. 2.3.3) was not available when these spectra were recorded, spectra at 90° were not available.

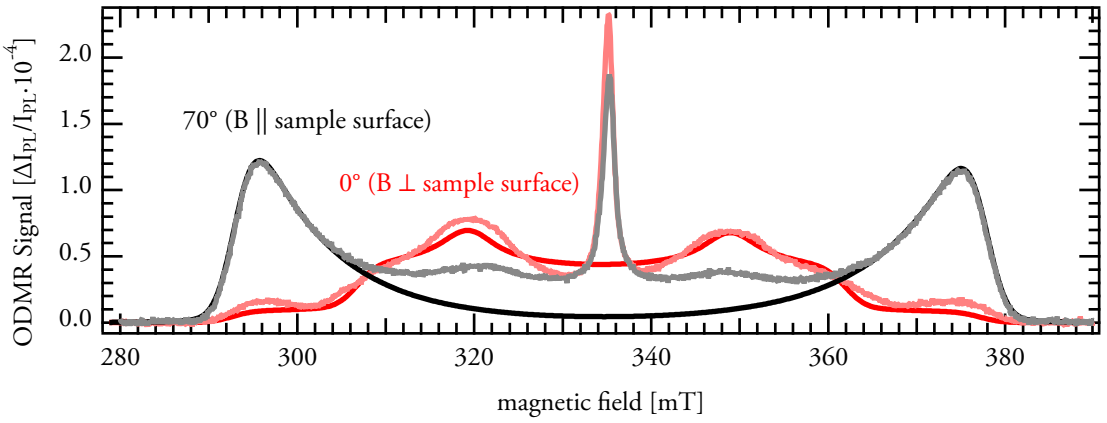

Figure 3.5.: ODMR (darker colors) and simulations (brighter colors) of PTB7. For B || sample surface, here the spectrum for $\vartheta = 70°$ was used, because the measurements were done before the fluence stabilization (ch. 2.3.3) was conceived. T=5K.

The zero field splitting parameters for the broad triplet in PTB7 were taken from [46] and slightly optimized, yielding $D = 1185$MHz and $E = 120$MHz. As expected, the change in ODMR spectral shape of the face-on PTB7 can be, unlike P3HT, explained considering only an ordering in respect to the ϑ angle and a Boltzmann equilibrium distribution of the Zeeman states. The spectrum for B || sample surface is simulated with an ordering parameter of $\lambda_\vartheta(0°) = -0.4$, which is a telltale for an ordering with the c-axis perpendicular to the

magnetic field. Conversely, the spectrum for B ⊥ sample is simulated with $\lambda_\vartheta(70°) = 2$, where the c-axis ordering should be along the magnetic field. Summarily, the deconvolution of the ODMR of PTB7 corroborates the assumption of the materials face-on configuration. Another interesting property of an OPV heterojunction comprising PTB7 is an electron back transfer, which will be discussed in ch. 3.4.

3.3.4. Diindenoperylene

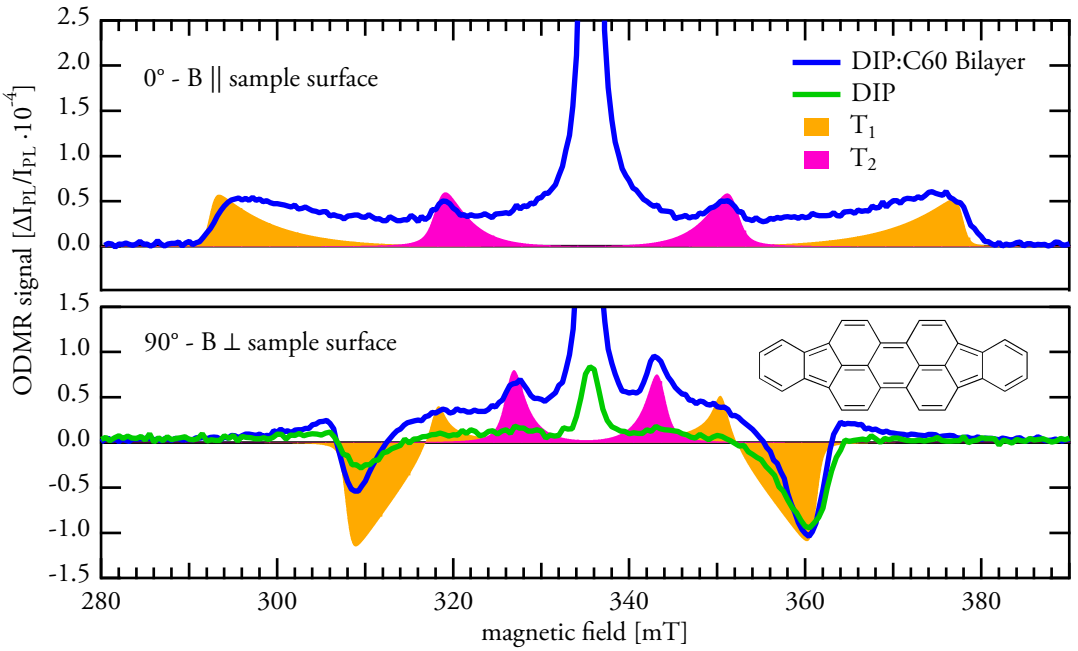

Figure 3.6.: ODMR of DIP and a DIP:C_{60} bilayer. The experiments (pure DIP in green, DIP:C_{60} bilayer in blue) were carried out at $T = 5$K. The simulations (fills to zero) were done using two $S = 1$ spins systems with $D_{T_1} = 1205$MHz,$E_{T_1} = 100$MHz, non-Boltzmann population, and $D_{T_2} = 480$MHz, $E_{T_2} = 0$, Boltzmann-population. For 0°, the ordering parameter was $\lambda_\vartheta = +6$ (c-axis aligned with magnetic field), and conversely, for 90°, $\lambda_\vartheta = -6$ (c-axis ⊥ magnetic field). The DIP chemical structure is shown in the inset.

The organic small molecule Diindenoperylene (DIP) yields, in conjunction with coevaporated C_{60} fullerenes as acceptor, reasonable solar cell power conversion efficiencies of around 4% [51]. It has also seen application as a exciton blocking layer for other OPV heterojunctions [52]. The limitation for DIP for sole application as a OPV donor lies in its preferred edge-on stacking configuration, which is advantageous for horizontal charge transport in thin film transistors, but hampers vertical charge transport in solar cell devices, as well as its light absorption. The latter is due to the optical dipole being perpendicular to the incident light [53].

The reason why DIP is worthwile concerning spin studies, lies in its supposed electron back transfer triplet generation. This is first hinted in preliminary measurements (not shown), where a simple mixed powder of DIP:C_{60} yielded a signature attributed to triplet exciton on DIP, where the pure DIP powder showed none.

The ODMR of pure evaporated DIP, shown in fig. 3.6 only shows a PL-quenching contribution at 90° sample angle, while at 0° no signal was found. In a bilayer of DIP:C_{60}, the ODMR signal strength is enhanced. Here, we can identify full field contributions in both 0° and 90°. However, describing the spectra is not trivial, as they boast stationary points, excluding the central peak. This can not be explained with one triplet exciton. We now assume one more localized rhombic triplet T_1 with $D_{T_1} = 1205$MHz and $E_{T_1} = 100$MHz, and one less localized axial triplet T_2 with $D_{T_2} = 480$MHz. Due to its similarity with the spectrum recorded for neat DIP, T_1 is attributed to a DIP localized triplet. The ZFS parameters for T_2, however, are close to the parameters of C_{60}. However, for C_{60} thin films, a strong rhombicity is observed ([54] and the shift of C_{60} half field in fig. 3.7), while T_2 is axial.

Therefore, the two possible scenarios to explain T_2 are: **(i)** The rhombicity of the C_{60} triplet, commonly observed in thin films, is lifted in DIP:C_{60} heterojunctions, as it is in C_{60} in a polystyrene glass matrix [54]. **(ii)** The T_2 is expressed by the DIP after all, but only in presence of the C_{60} acceptor. This could also be due to an electron back transfer to T_2, which is only possible with an acceptor in close vicinity. Additionally, the D, E values calculated for T_2 do also not match the values for the axial triplet of C_{60} in styrene glass ($D = 341$MHz [54]). Hence, scenario (ii) is more probable.

The simulations were carried out with an ϑ-ordering of the paramagnetic centers' c-axes along the magnetic field for B || sample surface, and c-axes perpendicular magnetic field for B $\perp$ sample surface. As the simulation matches the experiment, the assumption of an edge-on configuration seems to be valid. The mismatch between experiment and simulation amplitudes stems from the neglected ϕ-ordering, which is especially relevant for simulations of edge-on ordered crystals. Here, the central peak was also neglected. However, the drastic increase of this signal in the bilayer matches the usual assumption of distant, Coulomb bound charge carriers in triplet configuration, i.e. polaron pairs, giving rise to this signal.

3.4. Electron back transfer in high conversion efficiency photovoltaic heterojunctions

One key factor for the overall power conversion efficiency of a solar cell is the open circuit voltage V_{OC}. This voltage is ultimately limited by the gap between donor HOMO and acceptor LUMO. To increase V_{OC}, third generation OPV materials are commonly designed so,

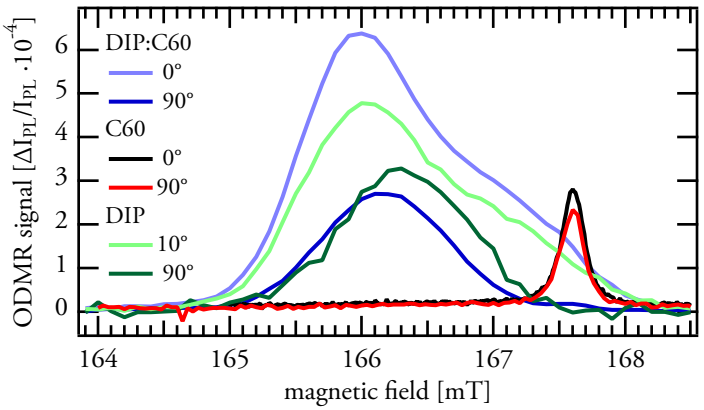

Figure 3.7.: ODMR of DIP, C_{60} and a DIP:C_{60} bilayer - half field transitions. The curves were recorded in the same experiment as in fig. 3.6. DIP and C_{60} and the Bilayer thin films were created by evaporation.

that the gap between donor and acceptor LUMOs is as small as possible. However, the donor triplet states can then, unlike in wide gape materials, be energetically situated below the acceptor LUMO (see fig. 3.11). This can subsequently lead to a back transfer of the excited and then separated charge carrier pair onto the donor, more precisely, the donor's triplet exciton state. Hence, when designing an OPV heterojunction, the balance between high open circuit voltage, and adverse effects like electron back transfer (EBT), has to be kept in mind.

Electron back transfer in OPV blends has already been observed in a blend of P3HT and the endohedral fullerence $LuN_3@C_{80}$-PCBEH. This molecule is a C_{80} cage encasing a Lutetium Nitride (LuN_3) complex, with a polar chain for solubility attached. However in this case, an intramolecular charge transfer in the acceptor, competing with the electron transfer from the donor, is held responsible for the back transfer [55]. In this manuscript, the hallmark for the electron back transfer was an incomplete quenching of the donor triplet exciton although an efficient charge transfer is taking place.

Similar observations were made in PTB7 heterojunctions. PTB7:PC_{70}BM bulk heterojunctions drastically improve their power conversion efficiency from 3.6% to 7.0% when adding 3 weight percent of diiodooctane (DIO) to the active layer solution [56]. This additive also heavily influences excitonics and morphology. In this chapter, results from photoluminescence quenching, morphology analysis through surface topography measured by atomic force microscopy (AFM) and ODMR, are linked to obtain information about a possible electron back transfer in PTB7:PC_{70}BM heterojunctions.

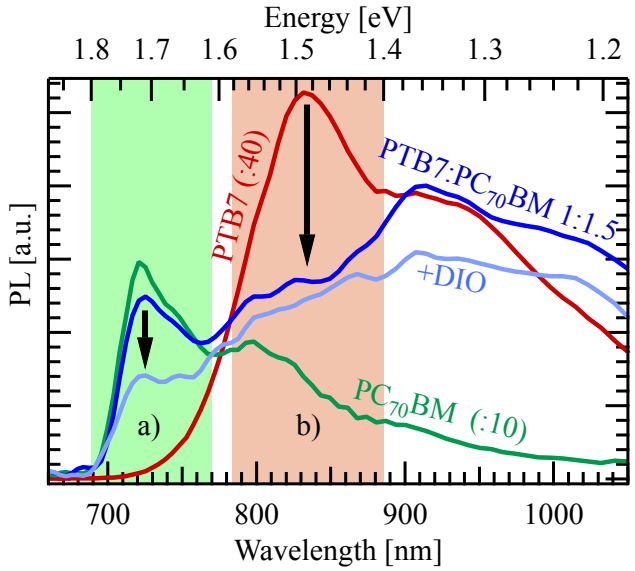

Figure 3.8.: Photoluminescence of the PTB7 blends and their constituents at $T = 5$K. The blends exhibit a pronounced quenching, as the PTB7 PL is 40 times stronger, while the pure $PC_{70}BM$ PL is 10 times stronger. T=5K.

3.4.1. Photoluminescence quenching of PTB7:$PC_{70}BM$

For photolumincescence (PL) spectroscopy, the samples were mounted on a helium coldfinger cryostat and kept under dynamic vacuum during the measurement. The excitation source was a cw laser at a wavelength 532 nm with a power of 14 mW. The PL was collected by large diameter concave mirrors and focused into a monochromator. The signal collected by a silicon photodiode was recorded lock-in, and afterwards corrected for the spectral responsitivity of the setup. The PTB7 and both blend film samples were all 100 nm thick; the neat $PC_{70}BM$ sample had an undefined thickness due to crystalline spikes dominating the sample surface.

In PTB7, a strong PL in the near infrared was observed (Fig. 3.8), showing a vibronic progression with a peak-to-peak distance of 0.11 eV around 900 nm (1.4 eV) at $T = 5K$. The emission from $PC_{70}BM$ is at higher energies, peaking at 720 nm (1.7 eV). The PL of the PTB7:$PC_{70}BM$ 1:1.5 blend expresses a strong fluorescence quenching to roughly $\frac{1}{40}$ of the PTB7 PL, with the shape roughly following a superposition of the blend constituents, save the vanishing primary PTB7 peak at 1.5 eV (Fig. 3.8b) and an additional shoulder at lower energies. Upon addition of DIO, the acceptor signature at 1.7 eV decreases significantly (a), while the overall signal is quenched further. There is no certain indication for a charge transfer PL as seen in other low bandgap absorbers [57]. These results have also been reproduced at room temperature with the same conclusions.

The main message to extract from the PL quenching is the strong acceptor signature of the 1:1.5 blend, which already hints an excitation process of isolated $PC_{70}BM$, unfettered by the PTB7 donor phase. This isolation is obviously lifted upon addition of DIO.

3.4.2. Additive influence on morphology

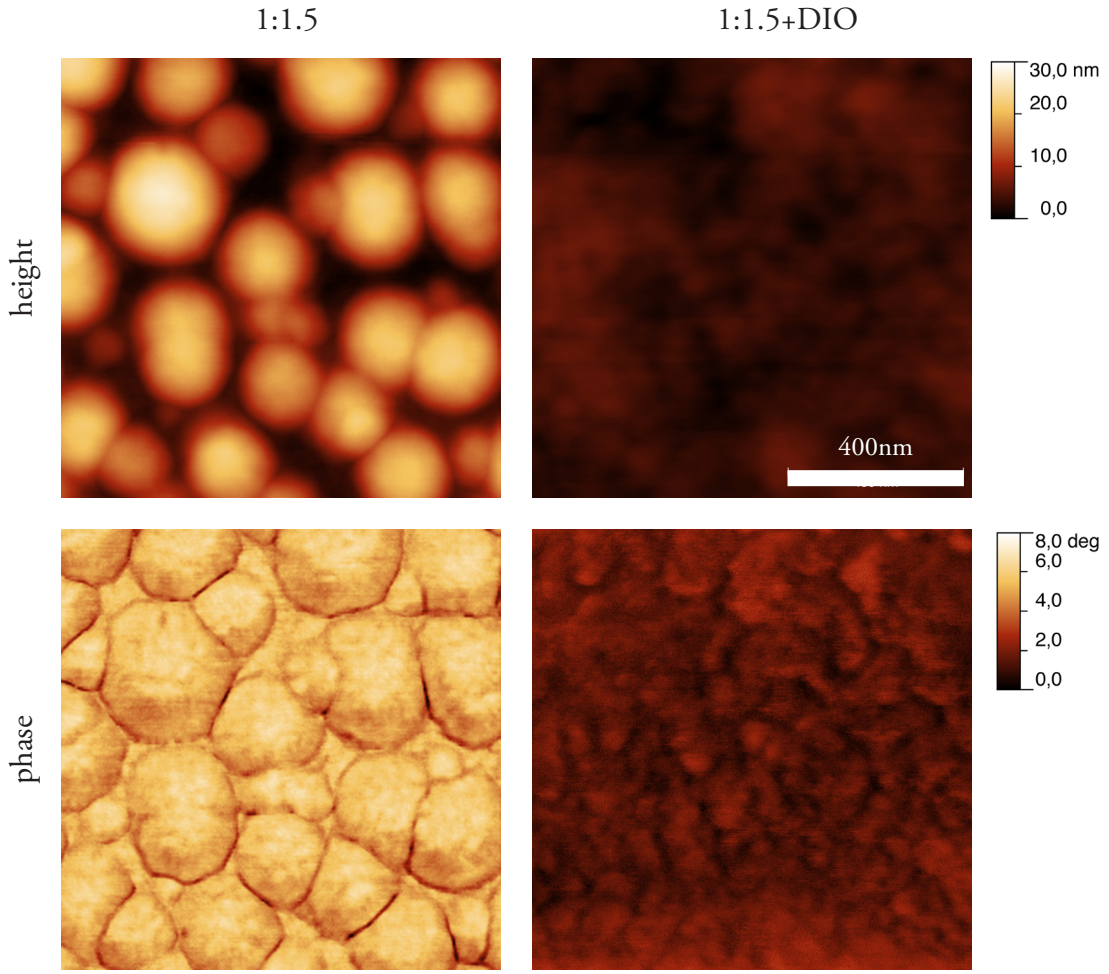

Figure 3.9.: Atomic force microscopy of the PTB7:PC_{60}BM surface with and without additive. The height and cantilever response phase were recorded in tapping mode at ambient conditions.

The atomic force microscopy (AFM) images were recorded with a Veeco/Bruker Dimension Icon microscope, with a tip radius of 10 nm on functional solar cell devices. The specimens were glass with indium tin oxide and PEDOT:PSS, followed by the PTB7:PC_{70}BM active layer and evaporated Ca/Al contacts. The preparation is described in greater detail in [56]. For the measurement, the AFM tip was placed on the area of the active layer where no Ca/Al contact was situated, in conventional tapping mode. Height and phase of the tapping response were recorded, as the phase image is more convenient to detect the donor–acceptor boundaries of composite materials [58].

The AFM images (Fig. 3.8 bottom) for PTB7:PC_{70}BM 1:1.5 without additive show a very explicit phase segregation, with a roughness of 25 nm and circular islands with an average

diameter of 200 nm. In the tapping phase image, these islands show a retardation of the tapping response, which is attributed to $PC_{70}BM$ [59].

When adding DIO, this phase segregation is almost completely lifted (right side of fig. 3.9). The heterojunction surface becomes very flat, with an average roughness of 7 nm and no distinct phase segregation. Together with the increased performance, a better intermixing of the heterojunction constituents is expected upon addition of DIO.

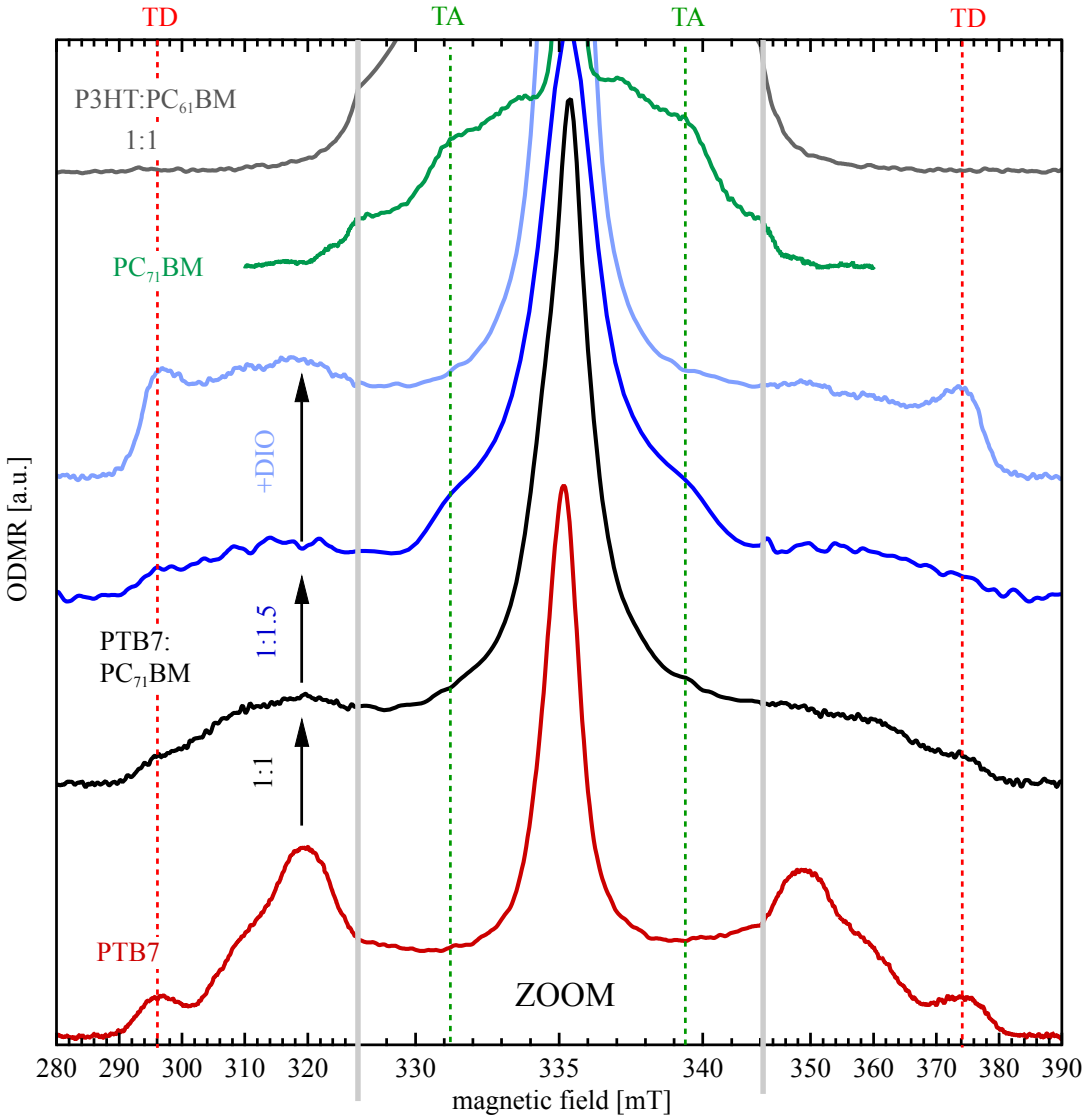

Figure 3.10.: ODMR spectra of PTB7 and PTB7:$PC_{70}BM$ blends with different donor:acceptor ratios, with and without addition of DIO. For comparison, the P3HT:$PC_{60}BM$ blend (grey) and pure $PC_{70}BM$ (green) are shown. In the environment of the central peak (325-345mT) the x-axis is rescaled to allow identification of the narrower $PC_{70}BM$ triplet. The outer stationary points of the PTB7 triplet (**TD**) and the inner peaks attributed to the $PC_{70}BM$ triplet (**TA**) have been marked with dashed lines.

3.4.3. ODMR of PTB7 blends

The ODMR of a PTB7:$PC_{70}BM$ heterojunction and its constituents are shown in fig. 3.10. The triplet resonances of the neat PTB7 and neat P3HT have already been discussed in ch. 3.3. The narrow polaron pair resonance at $g \approx 2$ ($B \approx 336$ mT) stemming from almost separated triplet-like charge transfer states [41, 60], is neglected, because it is not relevant for the forthcoming discussion.

As expected [61], the blend of P3HT:$PC_{60}BM$ ODMR shows a complete quenching of all triplet excitons characteristic for its neat constituents [55]. All PTB7 heterojunctions, however, express triplet patterns. Also shown is the signature of neat $PC_{70}BM$, which has a smaller zero field splitting, leading to a 8 mT wide full field triplet.

The ODMR spectra of PTB7:$PC_{70}BM$ blends show distinct differences as the blend ratio is changed from 1:1 to 1:1.5. For a 1:1 blend, signatures of polymer triplet excitons are observed with parameters identical to those of neat PTB7, which is linked to a triplet exciton localized on the polymer donor (henceforth named **TD**, Triplet Donor). The triplet pattern in the blend is probably blurred by the lesser degree of spatial order compared to the neat film.

Going to a surplus of fullerenes (1:1.5), these polymer triplets are almost quenched, while an ODMR signal very similar to the neat $PC_{70}BM$ signature emerges. It is hence associated with triplet exciton localized on the fullerene acceptor (from now referred to as **TA**, Triplet Acceptor).

The addition of DIO upon the 1:1.5 blend in turn quenches the $PC_{70}BM$ triplet, while the PTB7 localized **TD** reappears.

3.4.4. Electron back transfer in PTB7 heterojunctions

Using PTB7 as donor moiety for OPV is interesting, because V_{OC} of the devices is easily above 800mV, while a J_{SC} of 12mA/cm^2 is still maintained. The aforementioned P3HT:$LuN_3@C_{80}$-PCBEH has a similar open circuit voltage, but a much lower J_{SC}. It expresses a significant amount of molecular triplet excitons localized on the donor [55]. This triplet generation and drop in J_{SC}, was attributed to the EBT of already separated electrons to the donors' T_1 triplet state, which is situated slightly below the acceptor LUMO. A similar picture can be drawn for the PTB7:$PC_{70}BM$ blend, although in the PTB7 blends a high short circuit current is maintained despite the EBT.

The ODMR results can be described by the concurrent EBT and direct triplet conversion processes shown in Fig. 3.11. The 1:1 blend with the PTB7-localized triplet yield (**TD**) could be due to direct ISC in neat PTB7 islands within the blend, or due to EBT at the donor–acceptor interface. We propose the EBT path, with the following chain of reasoning: We link the $PC_{70}BM$ localized triplet yield in the fullerene richer blends to direct ISC in the accep-

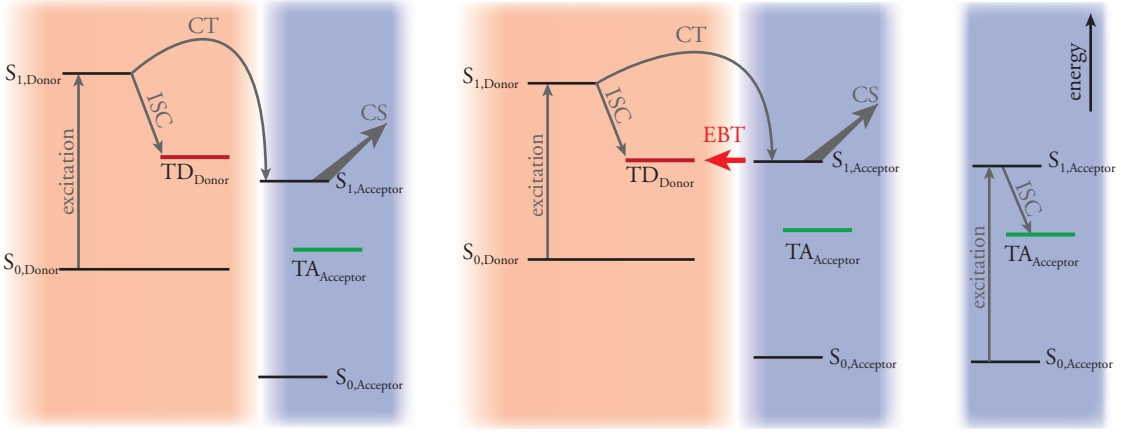

Figure 3.11.: Proposed charge transfer (CT), intersystem crossing (ISC), electron back transfer (EBT) and also charge separation (CS) mechanisms involved in the formation of triplets and photocurrent in blends of P3HT:$PC_{60}BM$ and PTB7:$PC_{70}BM$.

tor (fig. 3.11 c). This assumption is validated by the large isolated phases of the individual absorbers in the 1:1.5 blend, as observed in the AFM pictures (fig. 3.9) and by Lou et al. [62]

This is corroborated by the PL results, showing an $PC_{70}BM$ signature in the 1:1.5 blends which disappears upon addition of DIO. This change and a slight redshift are the only changes in the PL due to DIO, the overall quenching ratio stays the same. Therefore, we can discount the possibility of ISC in neat donor islands being the reason for the reappearance of the PTB7-alike **TD** in the DIO blend. We rather suggest the increased amount of interfaces made obvious in the AFM images facilitates efficient charge transfer with subsequent electron back transfer to the donor.

An EBT becomes possible, when the excited state ($S_{1,\mathrm{Donor}}$) of the PTB7 is so close to the excited state of the $PC_{70}BM$ ($S_{1,\mathrm{Acceptor}}$), that the lower lying PTB7 triplet state $\mathbf{TD}_{\mathrm{Donor}}$ can be resonantly populated via a back transfer from the charge transfer state, as shown in fig. 3.11.

However, it is difficult to derive this $\mathbf{TD}_{\mathrm{Donor}} \longleftrightarrow S_{1,\mathrm{Acceptor}}$ resonance directly from the LUMO-LUMO gap of the involved systems. The LUMO energy values are only valid for uncharged molecules, and can thereof neither describe optical transitions nor molecules that are charged or in a charge transfer state [63]. However, we can take the LUMO-LUMO distance as a rough guide, to see if the behavior of wide gap vs. narrow gap donors moves in the right direction.

Consider the 1eV LUMO-LUMO gap of the PTB7 blend. It is 0.1eV narrower than the gap of P3HT:$PC_{60}BM$, which shows no localized triplet generation whatsoever. The reduced LUMO offset between PTB7 and $PC_{70}BM$ in comparison to the P3HT blend can also be derived from the higher open circuit voltage $V_{OC} = 0.76V$ [64, 59]. This is 140mV above

P3HT's $V_{OC} = 0.62$V [65]. Although V_{OC} is directly related to the gap of the donor HOMO and acceptor LUMO, a higher V_{OC} is also a hallmark for a reduced LUMO-LUMO gap [66]. The difference between directly measured LUMO-LUMO energy gap and the values for V_{OC} hints a divergence between the assumed energy gaps and the energy gaps relevant for the EBT process.

Both P3HT:$LuN_3@C_{80}$-PCBEH and PTB7:$PC_{70}BM$ express an EBT, but the latter has significantly higher performance. For a possible explanation, it should be noted that these measurements were done under open circuit conditions, without contacts on the samples. This weakens the charge separation (CS, Fig. 3.11) path, and could lead to charges lingering at the interface, hence increasing the observed triplet generation by EBT in PTB7:$PC_{70}BM$.

3.5. Organic photovoltaics – Summary

In this chapter, semiconducting materials for applications in organic photovoltaics were characterized using ODMR. Potential loss mechanisms induced by the formation of triplet excitons are shown to be present in most materials. The ordering of solid films at a mesoscopic scale was highlighted, and its influence on the ODMR curves and possible approaches to deconvolve these were presented. For the semiconducing polymers P3HT and PTB7, it was shown that, contrasting previous assumptions, one localized and one distant triplet exciton is sufficient to explain the ODMR response. For the small molecule diindenoperylene, two localized triplet excitons are suggested.

In the second part, the results from photoluminescence measurements, atomic force microscopy and optically detected magnetic resonance on neat and blended PTB7 were associated. The PL quenching shows efficient charge transfer also in the coarser blends without the additive DIO; with the additive the individual PL contribution from the neat materials is even further suppressed. AFM pictures show the drastic influence of the additive on the sample topography – and very probably also on the morphology – reducing the blend coarseness from 200 nm wide island to a smooth surface. This increase of interfaces is also observed in ODMR, where it increases the chance of an EBT from CT states to the donor triplet. Just considering ODMR, two different scenarios can explain the formation of triplet excitons on PTB7 and on $PC_{70}BM$, respectively:

1. Enriched domains of the pure materials are formed upon changing the blend ratio. Singlet excitons created inside these domains (polymer or fullerene) cannot reach the interface to undergo charge separation and therefore undergo ISC to triplet excitons.

2. The change in blend ratio, and hence the change in morphology affects the rate of electron back transfer (EBT) from the charge transfer state back to the polymer triplet.

Together with PL quenching and topography data, the latter scenario is proposed for the typical PTB7:$PC_{70}BM$ 1:1.5+DIO solar cell blend.

To summarize this chapter, EPR and ODMR have proven to be powerful tools to establish the existence and ascertain the nature of charge carriers in organic photovoltaic materials, and can also readily be used to investigate new, interesting players on the photovoltaic field, e.g. metal halide perovskite solar cells [67].

4. Semiconducting single walled carbon nanotubes (SWNT)

" 'The result of two hundred years of solid-state physics. For whatever good that does, it is a continuous pseudo-one dimensional diamond crystal - though it's not actually pure carbon. There are several trace elements in carefully controlled amounts. It can be mass-produced only in the orbiting factories, where there's no gravity to interfere with the growth process.' 'Fascinating ... I can appreciate that this may have all sorts of technical applications. It would make a splendid cheese cutter.' "

— Arthur C. Clarke „The Fountains of Paradise", 1978

4.1. A brief history of the research on carbon nanotubes

A common misconception is to whom the first documented discovery of carbon nanotubes can be attributed to. Commonly, this accomplishment is ascribed to Sumio Iijima in 1991 [68]. However, there's a manuscript which predates the work of Ijima by almost 40 years: Lukyanovich and Radushkevich show transmission electron microscopy images of 50μm thick hollow carbon fibers in [69]. From there, many researchers found evidence for nanotubes using different growth technologies, but without noticing the importance and potential of this novel carbon allotrope [70].

The reason why the work of Ijima is perceived as the groundbreaking for the nanotube research is, according to [71], a combination of the paper not being in specialized materials science journals, but in the high ranking Nature journal read by an interdisciplinary audience, and science in the 90s reaching the maturity to get ready to "think nano".

Until 1993, all nanotubes investigated were of the multi-walled kind (MWNT). This changed as, again Iijima [72], and independently Donald Bethune [73], presented the first single walled nanotubes (SWNT). From there, a multitude of potential applications for nanotubes unfolded: In material engineering, from mundane implementations like a nanotube enhanced bicycle [74], to rather arcane future technologies like space elevators [75, 76];

Results of this chapter are partially published in Nat. Photonics [21].

in medicine as means to convey heat to the direct vicinity of cancer cells [77]; and among others, in electronics, where transistors [78] and the improvement of the efficiency of solar cells are viable applications. Finally, there are also some first reports on nanotube photonic devices [79, 80].

There are two families of nanotubes: Semiconducting and metallic. The structure which determines the family a tube belongs to will be introduced in the following chapter.

4.2. How to roll a nanotube

There are multiple characteristic features of nanotubes. The most prominent characteristic is whether the tube's walls consist of a single atomic layer (SWNT), or if there are two or more concentric layers. Although the individual tubes comprising a multiwalled tube (MWNT) can be semiconducting, the whole tube is usually metallic due to the low statistic change of all layers being semiconducting. However, controlled growth of semiconducting triple wall nanotubes has been reported [81].

For single walled carbon nanotubes, the deciding factor to be metallic or semiconducting is the chirality.

4.2.1. Chirality

Carbon nanotubes are, in principle, rolled up graphene sheets. The characteristic parameters are the diameter of the tube, and the so-called "chiral" angle to a plane orthogonal to the tubes axis. Both parameters can also be described by a pair of indices (m,n). These refer to two unit vectors starting from one carbon ring, as depicted in fig. 4.1.

The usual configuration is called chiral, but there are two special cases, the armchair nanotube (m=n) and the zigazag nanotube (m=0) (fig. 4.2). The chirality, as the principal describing parameter of the SWNT, governs its structural and especially electronic parameters. As a general rule, if $\frac{m-n}{3}$ is an integer, the tube possesses metallic character, otherwise it is semiconducting. This can be calculated by simplifiying the 2-dimensional energy dispersion from the tight-binding approximation for graphite for a tube with infinite length. This allows to reduce the dispersion to one dimension, leading to discrete energy bands which can provide a Fermi gap or not, only depending on the tubes diameter [82]. For small diameters, this rule is weakened by effects of curvature and subsequent rehybridisation [83].

The diameter of a tube can be calculated with

$$d_{\mathrm{SWNT}} = \frac{a}{\pi}\sqrt{n^2 + m^2 + nm} \tag{4.1}$$

with the graphene lattice constant $a = 246\mathrm{pm}$.

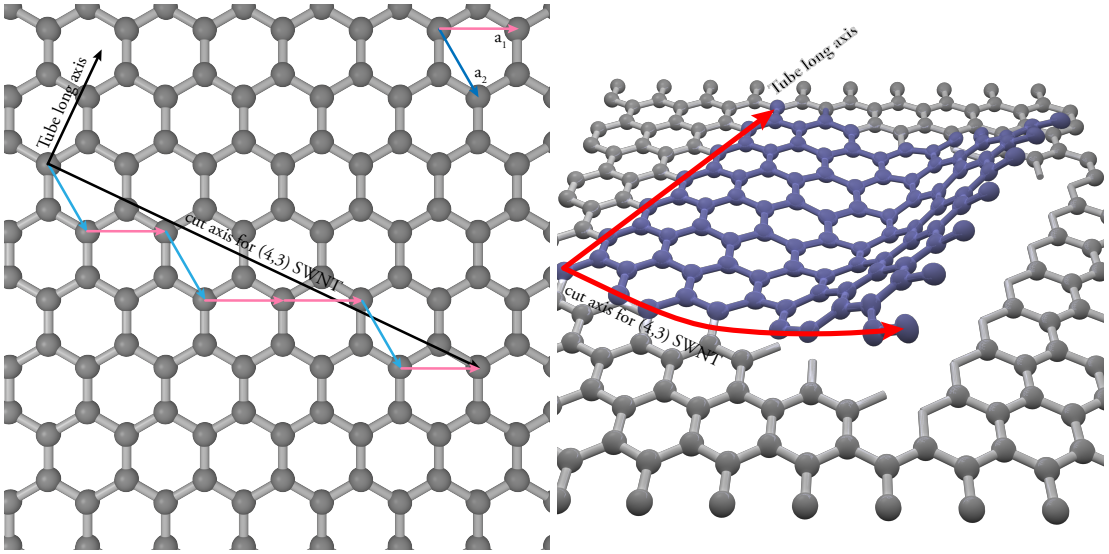

(a) (b)

Figure 4.1.: Description of a nanotube using (m,n) chirality indices. **a**) a graphene sheet with the (m,n) indices, and an exemplary (4,3) cut axis. The nanotube is constructed by cutting along this axis, then along the nanotube long axis starting from (0,0) and from (m,n), then roll it up. **b**) shows this for the (4,3) tube

4.2.2. Electronic structure

The electronic structure of a SWNT directly stems from the aforementioned band structure, which is shown in fig. 4.3 for the semiconducting (6,5) tube. The first optical transition E_{11} occurs between the band edges, between the innermost so-called *van-Hove-Singularities*, as well as the between higher levels, as depicted in fig. 4.3a. The nomenclature is S_{ii} for a semiconducting nanotubes' transition, M_{ii} for a metallic, and E_{ii} if the tube type is unknown or not relevant, with ii standing for the participating van-Hove levels. Transitions can only occur between the ith level in valence and ith level in conduction band. Crossover transitions $E_{ij}, i \neq j$ are forbidden, but can be observed by cross-polarized excitation [84, 85].

To project the calculated band structure to a real optical transition spectrum, we have to consider the peculiarities of excitonic states in graphite, and therefore also in SWNTs. Contemplating the reciprocal lattice of graphite, one notices two possible Brillouin zones K, K', and hence, two band valleys with different k-vectors [87]. Excitons can now form either as electron-hole pairs in one valley (A-Exciton), or with either hole or exciton in K, and the partner in K' ($\mathscr{E}$-Exciton). The latter ones can not recombine radiatively, as they have differing k-values, and therefore form "dark" states [88]. The A and $\mathscr{E}$-Excitons are, because of symmetry [89], split into altogether four excitonic states, of which just one (the odd symmetry A_2) is allowed optically – "bright". To summarize, for one E_{ii} there are four possible excitons, of which one is optically allowed.

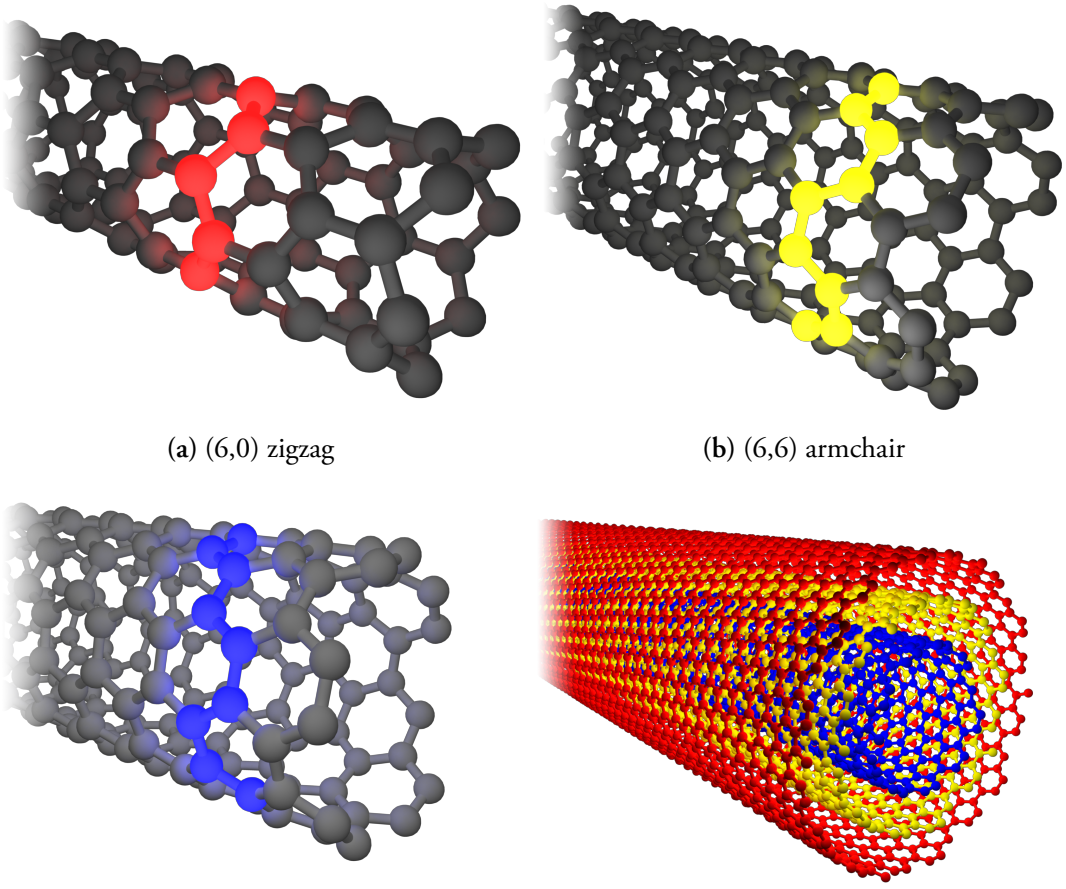

(**a**) (6,0) zigzag

(**b**) (6,6) armchair

(**c**) (6,5) chiral

(**d**) Triple-walled MWNT

Figure 4.2.: Overview over different types of nanotubes. **a**) a (6,0) metallic zigzag tube. **b**) a (6,6) metallic armchair tube. Zigzag and armchair tubes get their nicknames from the shape of the line if one follows the circumferencing C-C bonds. **c**) the semiconducting (6,5) nanotube, which was also used in all experiments in this work. **d**) An example for a multiwalled nanotube, the semiconducting triple walled nanotube sample 1 from [81].

These bright transitions of the (6,5) tube, shown in 4.3b, are blueshifted in respect to the DFT calculated values. This is due to the Coulomb interaction between the tube's electrons, which is not included in the calculation. It enhances the band gap and simultaneously creates the bound excitonic states, which absorb most of the excitation intensity [90]. Furthermore, π electron screening of an exciton by other electrons depends on the dielectric constant $\varkappa$ of the tube itself and its respective environment; e.g. variations of $\varkappa$ can change the E_{11} transition energy by almost 50% [91].

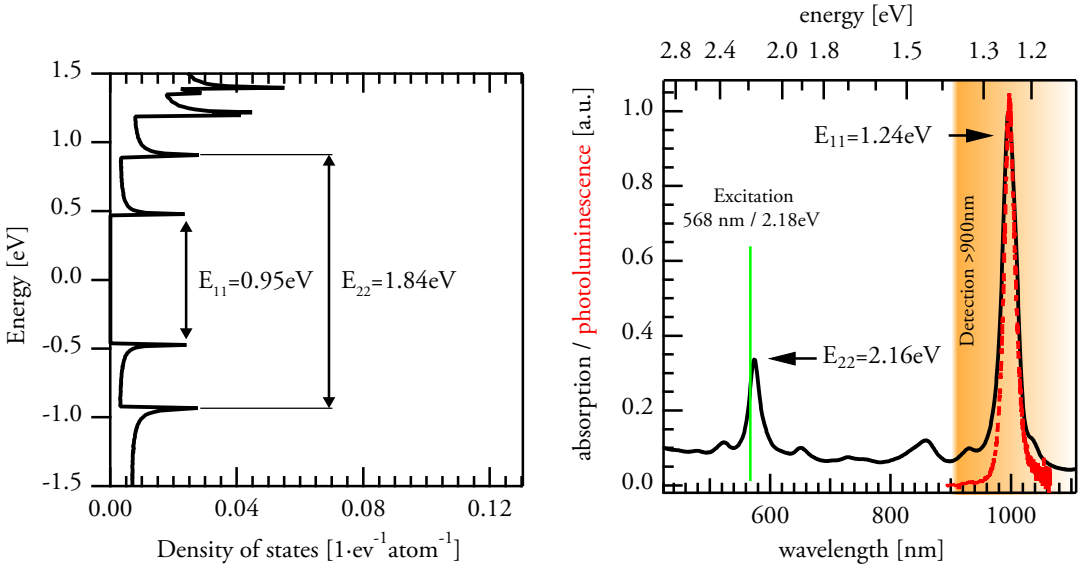

Figure 4.3.: Electronic states of (6,5) SWNT. a) shows the density of states, calculated with real-space density functional theory according to [86]. The first two excitations are higlighted with their energies, as they correspond to the optical absorption and photoluminescence spectra shown in **b)**. The energy mismatch between a) and b) supposedly stems from Coulomb interaction. The typical excitation (DPSS Laser @568nm) and detection (Silicon diode with longpass filter >900nm) energies for the ODMR experiments shown later are also denoted. Unless explicitly stated otherwise, this excitation and detection was used. *Absorption and PL measurements were performed by Florian Späth.*

4.2.3. Elusive triplet excitons

The large number of cited publications in the last chapter already hinted that, for singlet excitation of SWNTs, there's already a lot of theoretical and experimental work done. Triplet states, however, have only been incidentally noticed by the SWNT community, although they could play a decisive role in SWNT electronics and photonics. For hybrid SWNT photovoltaics, triplet excitons (TE) can either have a detrimental or enhancing effect on the conversion efficiency: In organic photovoltaics, triplet states are notorious for trapping excitations in long-lived, nonradiative recombination "dead-end" states (see ch. 3.2); nevertheless there are also reports on triplet-triplet upconversion [92], and of singlet fission into two triplet excitons, increasing the quantum efficiency of the OPV system above unity [93].

The situation for SWNT is similar. The triplet trapping caveat is also valid for SWNT hybrid PV, as is the singlet fission scenario. For a nanotube single photon source [94], a triplet state could also pose as a long-lived "dead end", severely limiting the emission rate.

Albeit these important implications, there are only a few papers devoted to triplet excitons in SWNT, and these mainly concern themselves with *ab initio* or DFT theoretical predic-

tions [95, 96]; and experimental works which indirectly access triplets by probing exciton dynamics [97]. Until the research presented in this chapter, which was performed together with the colleagues from the physical chemistry at this university, no direct evidence of triplet excitons in SWNT with a spin sensitive method was furnished [21].

4.3. Proving triplets in SWNT

Direct proof of a triplet exciton can only be done by either observation of a phosphorescence, or by a spin sensitive approach. Optically detected magnetic resonance (ODMR) is the method of choice, as it is spin aware, but only sensitive on optical transitions. Unlike conventional EPR, it will ignore dark spin states which are only due to leftovers from chemical synthesis and sample preparation.

4.3.1. Not that "bright" states

Nevertheless, ODMR on carbon nanotubes is not trivial, as the tubes, due to their multitude of dark transitions, have very low photoluminescence quantum efficiencies of below 1% [98]. Much brighter fluorescing tubes with 20% quantum yields have been reported by Ju et al. [99]. They attribute the brightness they observe to absence of oxygen, which is a well known exciton quencher for SWNT. Like for the organic semiconductors, we took utmost care to keep ambient exposure of the samples to a minimum (see 2.3.4), and tried to drive out physisorbed oxygen by evacuating and heating the specimens before measurement. This has however no effect on chemisorbed oxygen, which is observed for carbon fibers [100]; heating could even have an adverse effect, as chemisorption in SWNT is reported to be accelerated by temperatures $> 200°C$ [101].

This problem is exacerbated by ODMR contrasts in organics and also fullerenes being notoriously low, and similar contrasts in the 10^{-4} range can be expected for carbon nanotubes. Summarily, finding a 10^{-4} variation in a 1% quantum efficiency material proved to be a challenging task.

As already mentioned in ch. 4.2.1, electronic and optical properties (i.e. "brightness") of a nanotube depend heavily on its surroundings. For the experiments shown here, mostly (6,5) SWNT stabilized by an organic matrix from a copolymer of 9,9-dioctylfluorenyl-2,7-diyl and bipyridine (PFO-BPy) were prepared by Florian Späth. The intricacies of the nanotube synthesis and isolation are beyond the scope of this work; the preparation is however described in [21] and, in more detail, in [102].

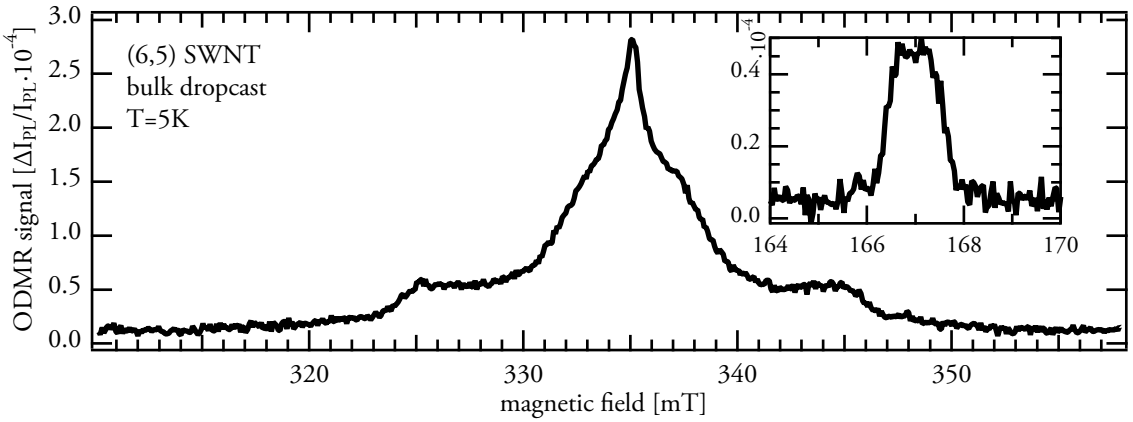

Figure 4.4.: ODMR of (6,5) SWNT. Excitation with a 568nm diode laser, detection with a silicon photodiode above 950nm, temperature T=5K. The inset shows the dipole forbidden $\Delta m_S = \pm 2$ transition. Here, the sample surface || external magnetic field.

4.3.2. ODMR of (6,5) single walled carbon nanotubes

The first ODMR spectra of (6,5) SWNT, as shown in fig. 4.4 and similar, in [21] fig. 3, were recorded from thick dropcast samples. In the bulky active layer in these samples, the tubes are randomly oriented, therefore the sample orientation in respect to the external magnetic field only plays a secondary role.

In the spectrum, a broad full field signal around g ≈ 2 (B ≈ 335mT at a microwave frequency of 9.4 GHz) can be observed. The shape and width of the signal already suggests a $S > \frac{1}{2}$ high spin state with a zero field splitting D. The final evidence is the existence of a half field transition, which can only exist in presence of a three-level Zeeman splitting.

4.3.3. Exclusion of matrix contributions

When discovering a new material property for the first time, scientific rigor requires best effort to exclude that the findings are due to measurement artifacts or synthesis leftovers. In this system, the most likely artifact is an ODMR of the polyfluorene-bipyridine matrix, in which the nanotubes are embedded.

To exclude this, another preparation pathway was used to create a gelatinous film sample, drop-cast from an aqueous solution. The gel samples were prepared as described in the experimental section of [103]; but gelatine was used instead of agarose gel, and the aggregation step was skipped.

Albeit having an even weaker photoluminescence than polymer embedded SWNT, the ODMR fingerprint looks similar. Except from this proof that the polymer-embedded and

gelatinous samples' ODMR are equal, in all other measurements only polymer samples were used due to their overall better signal to noise ratio.

Additionally, a sample was prepared with an identical preparation routine to the SWNT samples, with just the matrix polymer sans nanotubes as an active layer. Here, the ODMR response was nil, both with 568nm laser and UV lamp excitation.

At last, to further eliminate the possibility of measuring a one-shot contamination, the ODMR was verified on another polymer-embedded sample, yielding an almost identical curve to the first shown specimen.

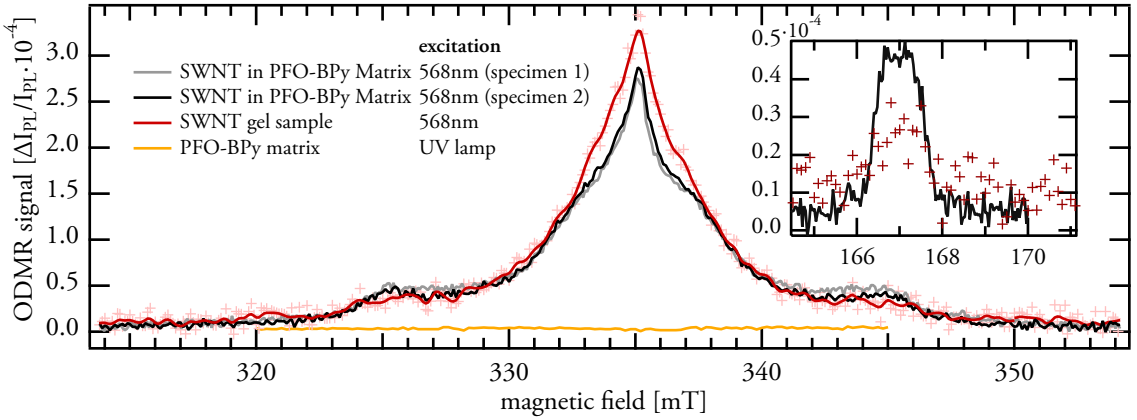

Figure 4.5.: ODMR Comparison of SWNT sample types and possible artifact sources. The first specimens curve (grey), already shown in fig. 4.4, is almost identical to the second specimen's (black, also shown in [21] fig. 3). The aqueous gel specimen (red crosses, averaged to red line) also possesses the same shape, albeit with a worse signal-to-noise ratio. The polyfluorene matrix shows no ODMR, neither under UV (orange) nor under 568nm illumination (not shown). In the inset, the also similar half field transitions of the gel specimen and PFO-BPy specimen 1 are shown.

4.4. Location and anisotropy of triplets on SWNT

In the last section, a first qualitative proof for a triplet exciton was shown. However, the powder spectrum in fig. 4.4 is broad and featureless, and does not allow for fitting EPR zero field splitting parameters. In the case of nanotubes, this problem can be approached by reducing the specimen dimensionality. The thick drop-cast samples can be seen as bulk samples, with nanotubes being randomly oriented in all directions. In a thinner sample, the large aspect ratio of the tubes only allows them to lie flat on the sample surface, albeit still randomly oriented on this surface. This reduces the 3-dimensional powder spectrum to two dimensions. To investigate thin SWNT films with ODMR, a SWNT-PFO-BPy sample was created by spincoating instead of drop-casting the SWNT-polymer solution.

4.4.1. Understanding and simulating a 2D nanotube sample

The thin sample was mounted vertically into the resonator, i.e. angular dependence means the sample surface will be turned in respect to the external magnetic field (see also fig. 4.7). The contour plot in fig. 4.6 shows this on a spincoated thin (6,5) SWNT specimen. The angular dependence seems counterintuitive at first, especially from the viewpoint of crystalline EPR spectra (like in fig. 5.27). Here, the transitions look like the bulk powder spectrum from fig. 4.4, except a singularity at 90°, where the sample surface is perpendicular to the external magnetic field.

This can be understood when taking into account that, only at this angle really every nanotube long axis (from now on called, in analogy to the crystallographic principal axis, c-axis) is perpendicular to the external magnetic field. At other angles, due to the random orientation of the tubes on the sample surface plane, some tubes are more inclined to the magnetic field, some less (illustrated in fig. 4.7).

This singularity now reduces the dimensionality of the ODMR powder spectrum, which enables to ascertain contributing spin systems and their splitting parameters. In fig. 4.6, a simulation with an ordering parameter was carried out. This ordering parameter weighs the probability for a powder spectrum transition against the angle between molecular c-axis and magnetic field. The influence of the ordering parameter is described in more detail in ch. 2.1.6.

The ODMR curve for 90° in fig. 4.6 could now be simulated using two spin centers. The broad triplet spectrum T_1 is clearly an $S = 1$ triplet, the simulation was done with an axial zero field splitting $D_{T_1} = 345\text{MHz}$ and a rhombic ZFS $E_{T_1} = 78\text{MHz}$. Here, an extremely strong ordering of the tubes' c-axes $\perp$ magnetic field of $\lambda < -500$ was used. A second triplet T_Δ with $D = E = 0$ gives rise to the peak at $g \approx 2$, which we attribute to triplets with very large interaction distances. The triplet spectral position is shifted by $\Delta g = 0.0003$ to the T_1 triplet. To corroborate the assumption of two distinguished triplet excitons, the signal amplitude dependence on the excitation power, shown in fig. 4.10 strongly differs between T_1 and T_Δ.

The same parameters were then used to simulate the 0° spectrum, just without any ordering. The amplitudes do not match very well, which could be due to the nonlinearity of the ODMR signal generation pathway (ch. 2.2.1). This is not considered in the EPR simulations. Nevertheless, the turning points fit the curve. Together with the simulations with higher ordering at 90°, the spin system parameters can be assumed to be valid.

Consider the two-dimensional character of a thin nanotube sample: The ODMR orientation singularity at B$\perp$ sample surface, together with the information that all tubes lie isotropically with their c-axis $\perp$ B, allows to surmise the orientation of the paramagnetic centers (i.e. the T_1 triplet excitons) to be **along the tubes' c-axis**. The paramagnetic centers orientation

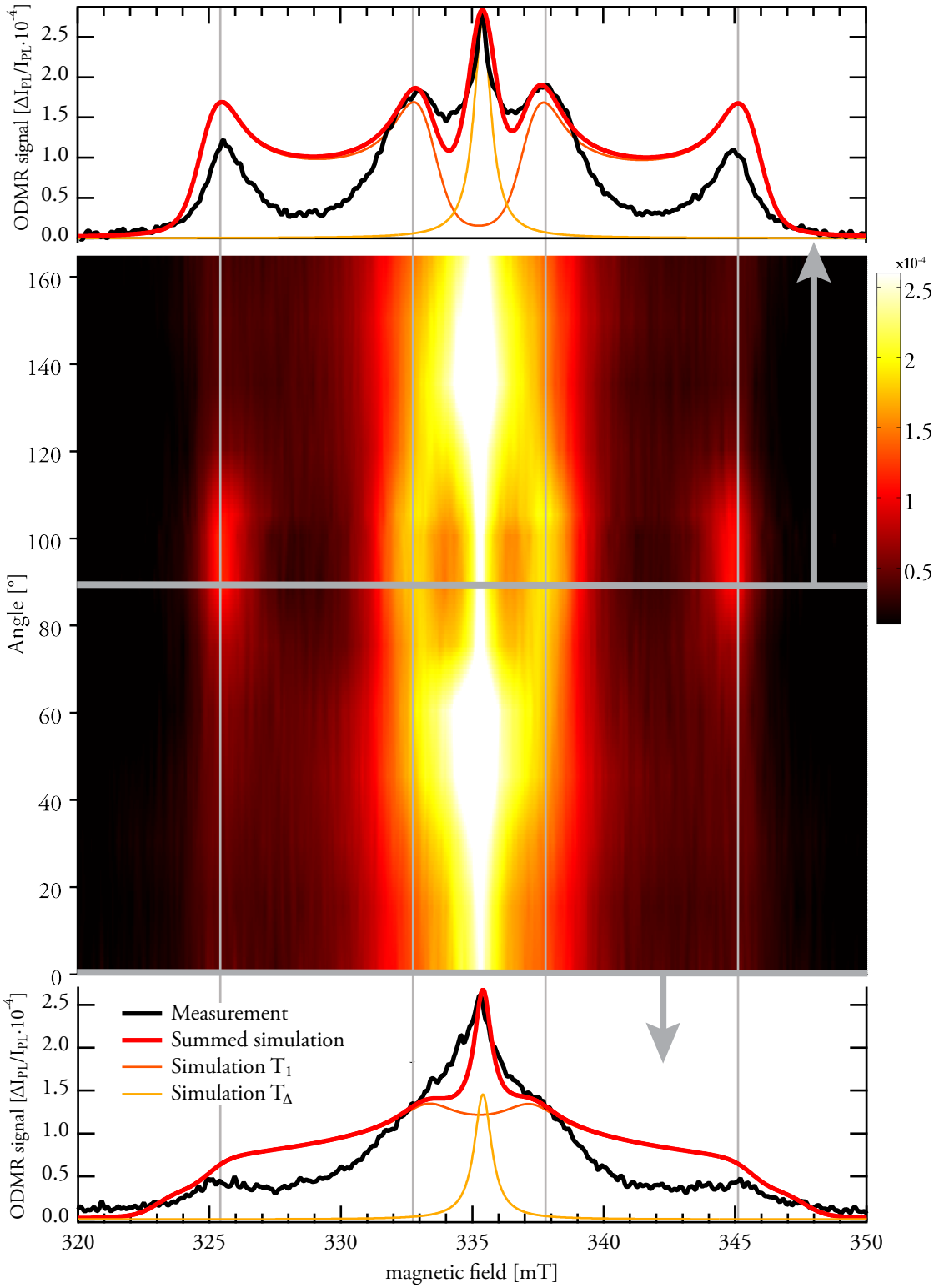

Figure 4.6.: ODMR of spincoated (6,5) SWNT, sample angular dependence. Two horizontal cuts at 0° (B || sample surface) and 90° (B ⊥ sample surface) are shown, together with simulations for two S=1 spins (parameters in the text). $T = 5$K.

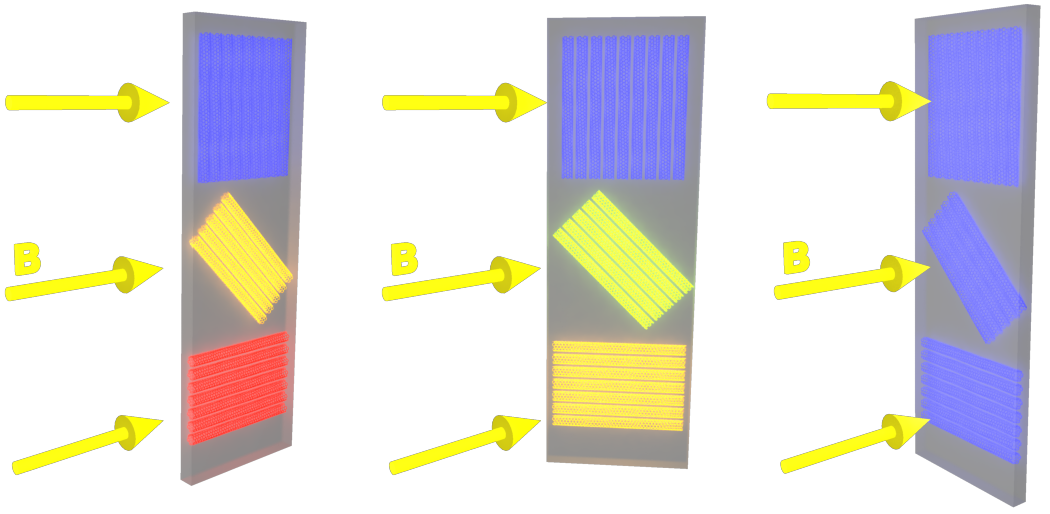

(a) 0° - B || sample surface (b) 45° (c) 90° - B ⊥ sample surface

Figure 4.7.: Illustration of the effect of different sample angles. The tubes' c-axis inclination to the magnetic field is shown by coloration from blue (not aligned to B) to red (fully aligned to B). See also fig. 3.2.

being other than along c-axis would necessitate that they would be oriented equally probable along x- and y-axis, because of the rotational symmetry of the nanotubes. This, in turn, would destroy the ODMR singularity.

With the values for D and E known, a very tentative approximation of the triplet wavefunction's extent $r_{T_1} = (4.8 \pm 0.4)\mathring{A}$ can be made. When using these values, it has to be considered that this approximation is only valid for axial triplets, while T_1 boasts a significat rhombicity. To take this into account, the error limits are extended to $r(D \pm E)$. Despite this source of uncertainty, the value matches the expectation for the exciton size to be below $10\mathring{A}$ [96].

To further elucidate the conformation of high spin states in SWNT, the obvious approach is to once more reduce the nanotube samples dimensionality. First tentative experiments were made with stretched, one-dimensional SWNT. The results are discussed in the next section.

4.4.2. Further down - one dimensional SWNT samples

To gain more information about the SWNT triplets' conformation, an obvious approach would be to further reduce the dimensionality of the sample. This was attempted by stretching of PFO-BPy-embedded nanotubes, which were in turn embedded in a polystyrene matrix. The tubes on the resulting samples are oriented in one direction, with a ratio of 8.6 : 1. This ratio could be determined by polarimetry, because the nanotubes act as optical dipoles – the sample is a linear polarisation filter [104]. For ODMR measurements, the sample was

mounted in the resonator according to fig. 4.8, with laser excitation via fiber from the top. In this experiment, 90° means the nanotubes c-axis ⊥ magnetic field, as shown in the schematic.

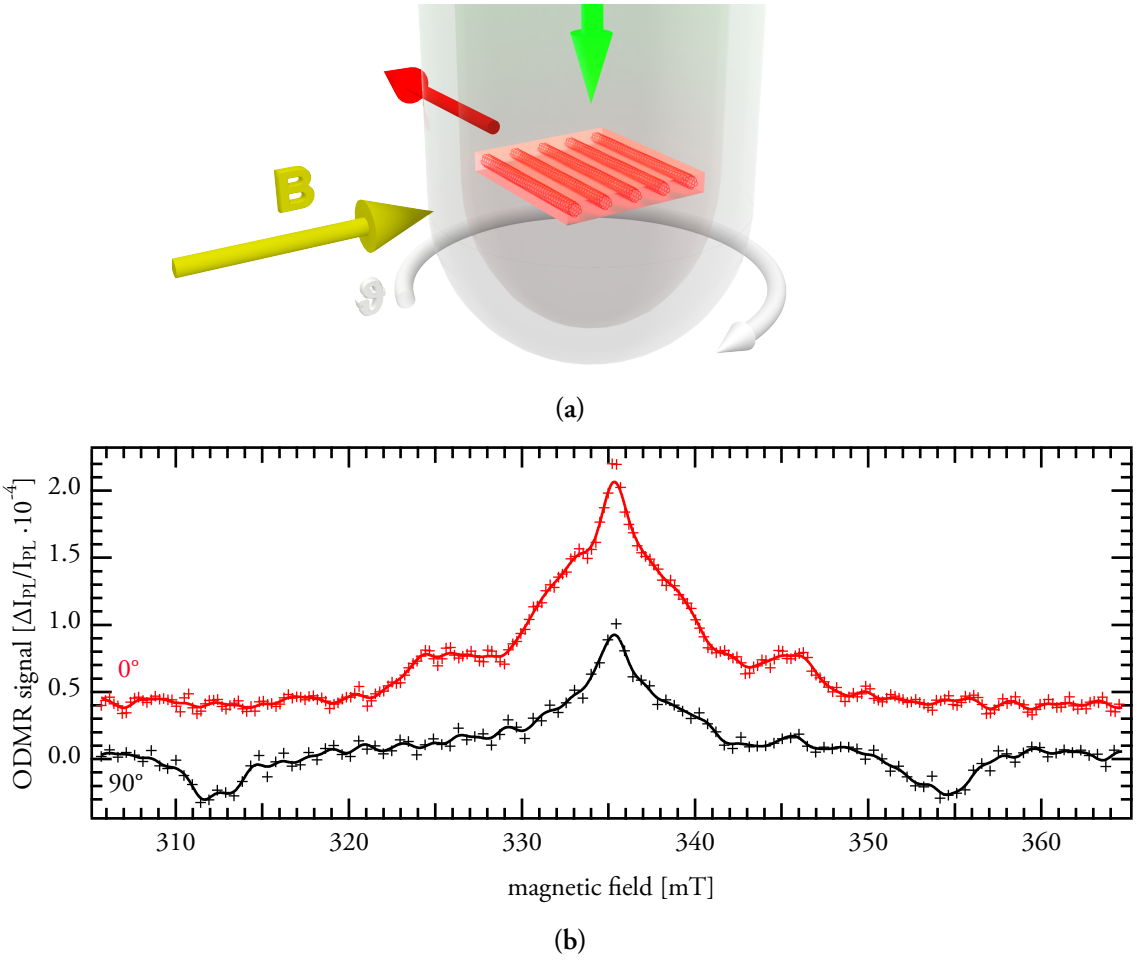

Figure 4.8.: Stretched sample measurement principle and ODMR spectrum. In **a**), the position of the sample is shown, here with 90° - B ⊥ c-axis. The green and red arrows signify excitation via a fiber, and the fixed direction of detection. **b**) shows the ODMR measurement taken with this layout at $T = 5K$. The markers constitute the measured data, which have been smoothed in the solid lines.

In fig. 4.8, at 0° sample angle (B || c-axis, the already familiar powder spectrum is observed, although a more pronounced deconvolution should be expected. Considering the limited spatial extent of the triplet described in the last chapter, the ratio of the stretched specimen could be insufficient to deconvolve the ODMR. This is envisaged by the stretched tubes being still folded and curved in the microscopic range relevant to the triplet exciton, but ordered in the mesoscopic range of singlet excitons. In this respect, the stretched sample could, counter-intuitively, behave even less ordered from the ODMR point of view, than the spincoated thin sample.

This is exacerbated by the results for 90° (B ⊥ c-axis). Here, an additional signature with an inverted sign can be observed. As the center for this signature is shifted by $\Delta g = 0.0123$ in respect to the T_1 g-value, it can neither be linked to an orientation response of T_1 nor of T_Δ. Hence a third triplet response of the SWNT has to be considered, however the present data is not sufficient to shed light on its nature or parameters.

4.5. Exciton kinetics from an EPR point of view

For continuous wave EPR and ODMR, the toolbox to investigate a spin system's dynamics is, especially in comparison with pulsed EPR, quite limited. However, a simple approximation to the involved timescales by observing the rf modulation dependency can be attempted. Although only giving rough estimates, it could help finding a missing link between species observed in cw EPR or ODMR, and time-resolved spectroscopy like transient absorption.

4.5.1. Triplet exciton lifetime

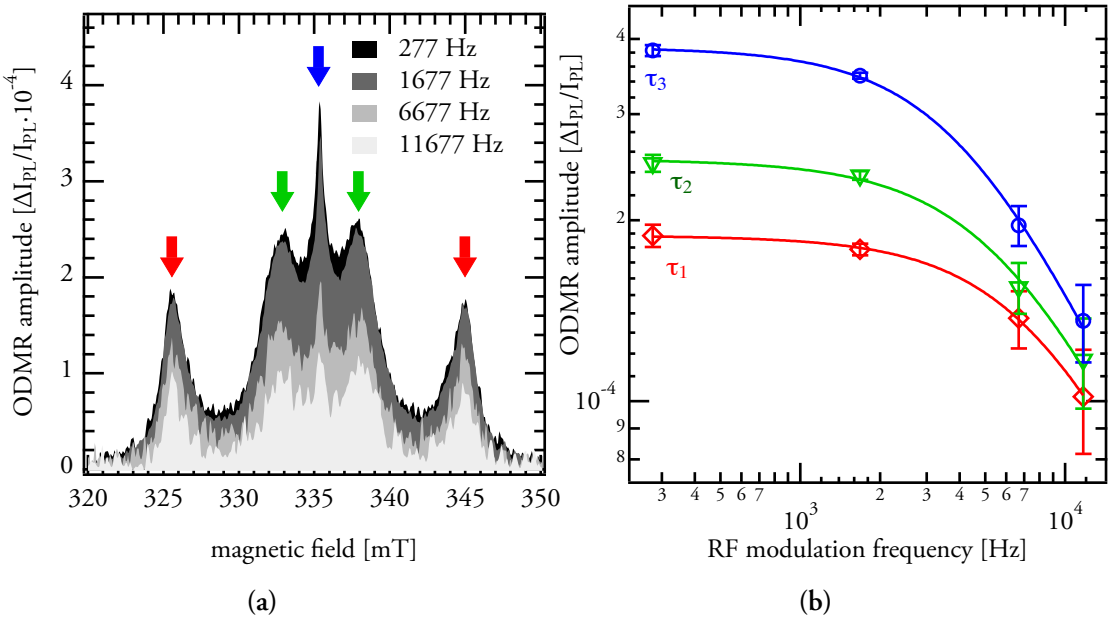

Figure 4.9.: RF modulation frequency dependence of the ODMR of a (6,5) SWNT thin film. In **a**), the ODMR magnetic field sweeps at different RF modulation frequencies are shown. The colored arrows denote the magnetic field positions of the values (averaged) shown in **b**). Here, the solid lines are fits according to [105]. The measurements were taken at $T = 5K$ and B⊥sample surface.

In full-field ODMR, the rf field is modulated with a square wave, i.e. the magnetic resonance interaction is switched on and off with a certain frequency. If the lifetime of the

observed species is now longer than the cycling of the RF interaction, the ODMR response will diminish. The response function to describe this effect is, for cw optical pump-probe spectroscopy, as follows [105]:

$$R_{\mathrm{ODMR}}(\nu_{\mathrm{mod}}) = \Re\left(\frac{R_{\mathrm{ODMR},0}}{(1+2i\pi\nu_{\mathrm{mod}}\tau)^{\alpha}}\right) \tag{4.2}$$

with $\alpha < 1$ describing the high-frequency falloff, and τ an upper-bound mean decay of the probed species.

For the (6,5) SWNT, this approach was applied to the experiments shown in fig. 4.9. With values of $0.92 < \alpha < 0.94$, the lifetimes were $\tau_1 = (20.3 \pm 3.2)\mu s$, $\tau_2 = (26.9 \pm 2.3)\mu s$, and for the low-interaction triplet T_Δ, $\tau_3 = (38.6 \pm 2.0)\mu s$. The approximated lifetimes of the T_1 triplet are close to the lifetime of $15\mu s$ found by Park et al. through transient pump-probe spectroscopy [97].

4.5.2. Multiphoton processes

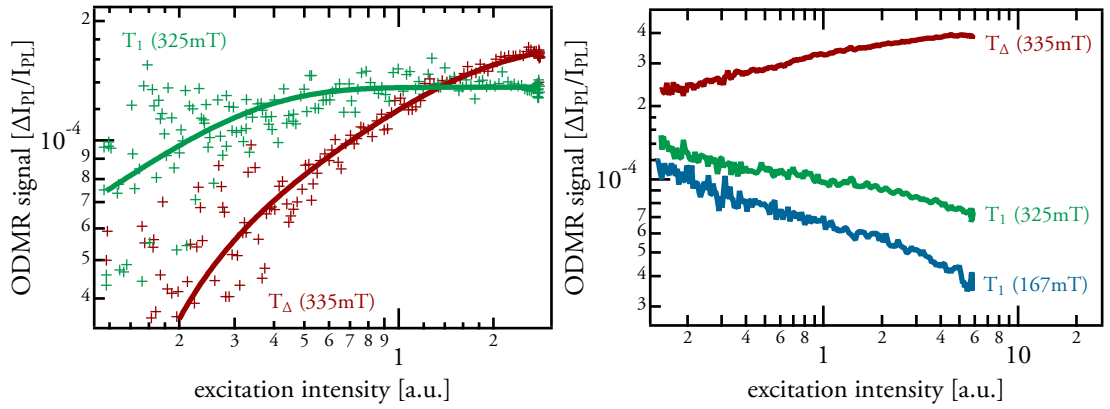

(**a**) thin sample (**b**) bulk sample

Figure 4.10.: Dependency of the thin and bulk SWNT ODMR on the incident excitation power. The T_Δ contribution's behavior differs significantly from the T_1 full field triplet, and in **b)** also from the corresponding half field contribution. Measurement at $T = 5K$; **a)** was excited directly, **b)** over a wider sample area with grazing incidence light from a fiber (for experimental details see ch. 2.3.3).

The presence of two distinct exciton species was already mentioned in ch. 4.4.1. The interaction range and type of these species can not only be estimated by their zero field splitting, it is also reflected in a qualitative manner in the ODMR response depending on the excitation intensity.

In the 2D sample (fig. 4.10a), the ODMR response is superlinear to the excitation dependence. A linear behaviour would yield a flat line, as the ODMR is already normalized on the

PL, which increases linearly with excitation intensity. This superlinearity, i.e. a higher ratio of triplet response per singlet excitation at higher singlet excitation densities, means that the triplet generation should be a multiphoton process. In other words, a higher exciton density means a larger fraction of triplet-related singlet fluorescence, which in turn should be due to two or more interacting triplets participating in the singlet fluorescence. A model for this interaction is discussed in the following chapter.

In fig. 4.10b, the bulk sample also shows a superlinear behaviour for the T_Δ long range interaction triplet, but the T_1 triplet oversaturates. Already in the T_1 curve in the thin sample, the onset of a saturation can be observed. This oversaturation is assumed to be due to high excitation densities, which leads to a signal decrease by saturating the triplet population, while the singlet population with its much shorter recombination times continues to increase [98]. This transition from the low intensity to the high intensity behaviour was discussed in more detail in [21] (escpecially fig. 4b and supporting information).

4.5.3. Triplet-triplet-annihilation (TTA) in SWNT

The multiphoton process observed in the last chapter, together with observation of a long lived delayed fluorescence by D. Stich, F. Späth and T. Hertel in [21] (fig. 1) now allows to pinpoint the excitation pathway for the SWNT triplet excitons: The triplet-triplet annihilation is the only mechanism, that explains both the observed kinetics and the delayed fluorescence.

The TTA model was already briefly introduced in ch. 2.2.2, and will here be discussed in greater detail, especially in respect to its application to carbon nanotubes.

In fig. 4.11, the possible excitation pathways are shown. SWNT are a low-dimensional system, whose large delocalization length facilitates the interaction of multiple non-geminate (previously non-correlated) excitons. In such a system, the mixing of two triplet states leads to the creation of either again of a triplet pair or of a single triplet. Additionally, with a $\frac{1}{9}$ probability, the triplet pair can also scatter to an excited singlet, which decays under emission of fluorescence, delayed by the lifetime of the TTA-channel.

To explain the ODMR resonance at with $D = 0$ at $g \approx 2$ (335mT), the analogy to the explanation for the polaron pair peak in organics (long distance localized free charge carriers in triplet configuration) is an option. A free charge carrier band above the E_{11} gap, which is populated via the E_{22} excitation, could be responsible for this signal [106]. However, as no light dependent EPR signal can be observed for charge carriers in SWNT [107], and with the signal also present with E_{11} excitation in the following section, this model is improbable. The large EPR signal in darkness, nevertheless, hints a large concentration of traps in the (6,5) SWNT [108]. These traps could facilitate a long-range triplet-trap-quenching [109, 110], giving rise to the observed resonance in the delayed fluorescence [111].

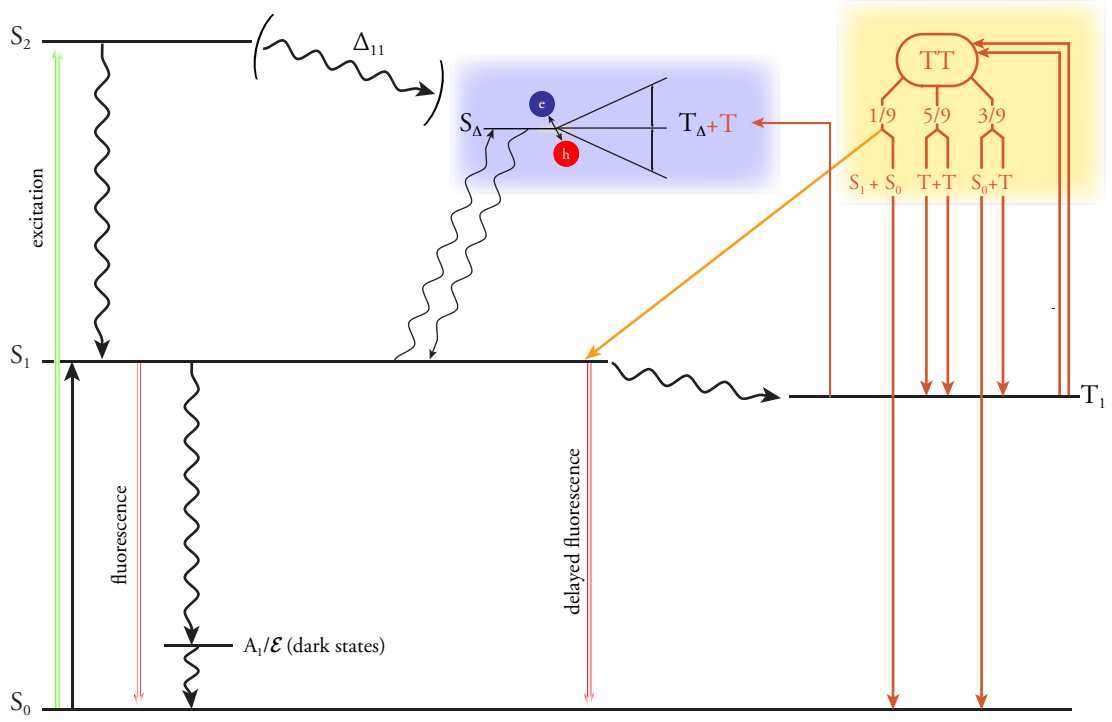

Figure 4.11.: Excitation schematic of semiconducting SWNT including triplet-triplet annihilation. The wiggly lines depict nonradiative transitions; the green and red lines are optical excitation and fluorescence, respectively. The orange lines denote the different pathways a triplet-triplet annihilation (orange box) can take. The triplet-polaron-annihilation is depicted in the blue box. As the mechanisms for triplet-trap-annihilation is very similar, it is left out. Triplet-polaron-annihilation at least of the Δ_{11} band is improbable, and therefore put in brackets.

4.5.4. $E_{22} \rightarrow E_{11}$ deactivation

It is well known that the deactivation from the S_2 (E_{22}) into the S_1 (E_{11}) state is a rapid process in the lower femtosecond range [112], which should be too fast to facilitate an intersystem crossing. The latter is occuring three orders of magnitude slower, needing tens to hundreds of picoseconds [113].

Nevertheless, the possibility that the observed triplet states could, contradicting our working model shown in 4.11, scatter directly from the S_2 into a higher triplet excitonic state, should not be discounted. To elucidate this question, the now well known ODMR spectrum with excitation into the S_2 (E_{22}) exciton was compared to a spectrum recorded with an excitation slightly above the S_1 energy (1.26eV), and detection of the residual tail of the S_1 fluorescence below 1.18eV. Obviously, the signal-noise ratio of the spectrum shown in fig. 4.12 is much lower with this measurement, but it was sufficient to show that the spectra are similar regardless of their excitation.

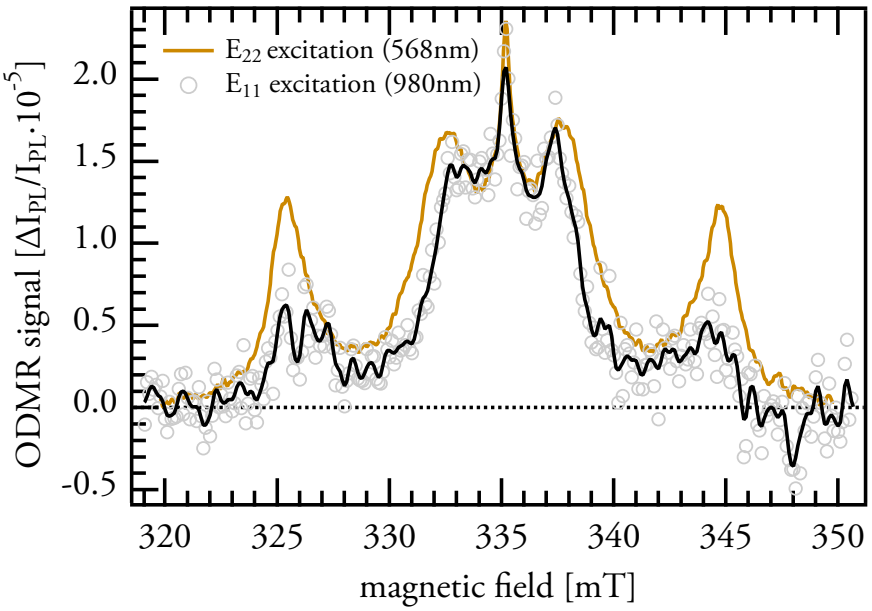

Figure 4.12.: ODMR of (6,5) SWNT with E_{11} excitation with a 980nm laser. Detection of the luminescence tail above 1050nm. The measurement (grey circles, smoothed: black line), was recorded at $T = 5$K on the thin sample with B $\perp$ sample surface. For comparison, the spectrum with excitation into the E_{22} band is also shown (orange line).

Additionally, the tentative assumption, that the long interaction distance triplet T_Δ is linked to the free charge carrier continuum, could be further discounted. As the continuum is populated through the S_2 exciton [106], the T_Δ contribution should be much weaker or absent when exciting into S_1.

4.6. Single walled carbon nanotubes – Summary

In this chapter, the first direct detection of the elusive triplet excitons in semiconducting (6,5) single walled carbon nanotubes was shown. The characteristic full field ODMR signature, corroborated by the existence of a half field transition, unambiguously ensured the observation of a high spin state. Artifacts could be excluded by examination of multiple samples made from different preparation pathways. The excitation kinetics and presence of a delayed fluorescence portend the triplet-triplet-annihilation as the excitation pathway responsible for the localized triplet's ODMR.

The zero field interaction parameters of the localized triplet could be deconvolved considering the reduced dimensionality of thin SWNT active layers, to $D = 345$MHz and $E = 78$MHz. In a nearly one-dimensional sample of stretched SWNT, another triplet signature could be observed, but not yet designated.

5. Spin defects in silicon carbide

5.1. Introduction to quantum computing, single photon application and metrology

The idea of using a quantum system for data processing is not a new one. Already in 1982 Richard Feynman suggested that quantum mechanics could be applied in data processing applications [116]. But Feynman also states the main problem in implementing such a quantum mechanics system using a classical computer: The hidden variable problem, which forbids the representation of quantum mechanics using a classical universal device. The solution to this problem is to actually use a quantum mechanical universal device, i. e. a quantum computer. David Deutsch extends on this idea, describing a universal quantum computer which can simulate every finite, realizable physical system, as well as the only possibility for a true random number generator [117]. Especially in light of the recent breakdown of computer cryptography, true randomness is a crucial component even for classical cryptographic methods [118].

Cryptography is also an important scope of the work of Shor, which tackles the number theory problem of integer factorization [119]. Prime factorization is a very good example for a problem which is very hard for classical computers, having a super-polynomial complexity [120]. In contrast, a quantum computer is able to factorize in polynomial time, which could be for example utilized to break the widely used RSA encryption.

But secret services are not the only ones that could be interested in quantum computing. It could also be used in big data evaluation, which is also becoming an important issue nowadays [121]. Grover proposed an algorithm that allows searching in a large unsorted database with the size n, not with the classical calculation cost of $\mathcal{O}(n)$, but with a much faster order of $\mathcal{O}(\sqrt{n})$ [122]. In general, a quantum computer can effortlessly outperform large classical supercomputer, at least for some specific problems; where the fundamental quantum parallelism allows the computer to perform multiple calculations at once. This is due to the fact that every quantum bit (qubit) coexists in a superposition of multiple states.

Results of this chapter are partially published in Phys. Rev. Lett. [114], Nat. Phys. [115] and Sci. Rep. [26].

To realize these qubits, the scientific community seeks quantum systems which can be initialized, controlled and read out in a simple manner, and retain their state for a certain time. Additionally, the quantum systems for qubit application often show, as "bycatch", promising properties for other quantum applications, e.g. single quantum systems can also act as single photon sources. In the following chapter, the fundamental necessities for a qubit quantum system, and the competitors for this application will be introduced.

5.2. Quantum systems for quantum computing

The search for the right systems to finally build a working quantum computer is on, but there are many obstacles on the way. David DiVincenzo formulated a set of physical criteria, which every candidate for implementing a working quantum computer has to reliably fulfill [123]. These criteria are:

1. A scalable physical system with well characterized qubits
2. The ability to initialize the state of the qubits
3. Sufficiently long decoherence time
4. A universal set of quantum gates
5. A qubit-specific measurement capability

Here, we will focus on spin-based systems, as they are amongst the most promising candidates to implement these criteria, satisfying especially the first criterion by being fundamentally quantum-mechanical in nature. A spin can be easily initialized by optical pumping and manipulated using magnetic resonance techniques. These are well developed, hence supporting the fulfillment of the fourth criterion.

To properly relate the advantages and caveats of our research focus, the silicon carbide (SiC) system, the other competing solid state spin-based approaches will be briefly introduced, focusing on the initialization (second criterion), coherence times (third criterion) and readout (fifth criterion). Additionally, feasibility of fabrication upscaling, as well as day-to-day applicability of the approaches will be discussed.

Silicon based quantum centers have been proposed to be realized in a spin-free isotopically pure ^{28}Si lattice, by embedding phosphorus donor centers with a low concentration of 10^{14}–$10^{15} cm^{-3}$ [124]. Here, the quantum information is stored in the electron spin bound to the donor, characterized by a very long coherence time, which very quickly progressed from two seconds reported by Tyryshkin et al. in 2011 [125], to 39 minutes in 2013 [126]. While the readout of this qubit class is done electrically, and hence very easy, the initialization of the

qubits via a pulsed magnetic field is difficult. Advantageous however is the readily available technology for silicon fabrication.

Quantum dot based quantum centers is an approach focusing on electron spins that are confined to quantum dots on semiconductors [127]. These spin qubits can be initialized and read out optically and electrically at zero magnetic field. Also, this system is one of the few where two-qubit operations have already been demonstrated [128]. The disadvantages of this system are the millikelvin operating temperatures, the short coherence time in the microsecond range [129], and the lack of large scale production technology.

Diamond NV-based quantum centers are, together with the SiC approach, the only system which is working at ambient conditions [130]. The qubits consist of single nitrogen+vacancy (NV) defects: Substitutional nitrogen atoms adjacent to carbon vacancy in a diamond lattice, which can be initialized optically into a certain spin state through a spin-selective relaxation path. This excitation is done with green illumination, and readout is also done optically, detecting the red photoluminescence of the NV defects. The ODMR contrast of the resonance lines is very high (up to 0.3) even at room temperature, making this system easily accessible [131]. These convenient properties are opposed by a lack of coherence time (2 ms), and a virtually nonexistent fabrication technology.

Finally, we should discuss the youngest competitor, the **silicon carbide** quantum center approach. The silicon vacancy first went into the spotlight as a qubit candidate when Weber et al. first-principle calculated the electronic structural conditions a quantum system has to fulfill to be feasible for qubit usage [132]. They identified hexagonal defects in the 4H polytype of SiC as a surprisingly suitable system, which fits the criteria they established equally well as the diamond NV center.

David DiVincenzo quoted this work in his estimation of the significance of the young SiC research field *"However, a search to find defects with even more potential has now been launched."*, where he highlights some supposed advantages of the SiC system over diamond NV centers [133]:

1. larger Franck-Condon-Factor (stronger zero phonon lines)

2. lower, more convenient transition frequencies

In the following chapters, the silicon carbide material systems will be introduced in more detail. Furthermore, some steps we have taken to elucidate SiC quantum defects as prospective qubit candidate will be discussed. At last, the intriguing properties of this quantum system opens possibilities for application not only as a qubit, but also as a quantum measurement method, a clock standard or even as a microwave amplifier (MASER) system; all of which will be shown later.

5.3. Silicon carbide, its polytypes and defects

SiC or carborundum is the only chemical compound of carbon and silicon. For technological applications, SiC has some interesting properties [134]:

- **High breakdown electric field.** SiC can endure a voltage gradient exceeding 7 times that of silicon.
- **Large Bandgap.** Almost as wide gap as diamond, SiC cannot be driven into intrinsic conduction by high temperatures.
- **Large Thermal conductivity.** Also close to the diamond performance, SiC boasts a thermal conductivity of up to $5\frac{W \cdot K}{cm}$.
- **High saturated mobility.** Although less performant than Si or GaAs in pure mobility terms, SiC exceeds the former two when nearing electric field saturation, i.e. when the drift velocity saturates at high fields, limiting the responsitivity of the system at rapid field modulation. This means SiC outperforms the other semiconductors at high frequency (microwave range).
- **Robustness against radiation.** Especially for high energy detectors, SiC's hardness against radiation is important. [135]. Although point (quantum) defects are easily introduced into the silicon carbide crystal lattice by neutron irradiation, as shown later in this chapter, the electric properties remain comparatively unfazed [136].

Because of these properties, SiC is seeing more and more applications, especially in extreme environments (spacecrafts) and for high power electronics. Thus, in contrast to e.g. diamond, the fabrication of SiC wafers and devices is a commercially established procedure, and different polytypes (3C, 4H, 6H...) can be routinely grown on wafer scale since the 1990s [137].

There exist about 250 crystalline forms of SiC. This polymorphism is characterized by a large family of similar crystalline structures called polytypes. These are variations of the same chemical compound which are identical in two dimensions and differ in the third. Thus, they can be viewed as layers stacked in a specific sequence. For the research shown here, we mainly use silicon carbide grown with the modified Lely method [138, 139], of the 6H and 4H polytypes. The 6H polytype is a hexagonal wurtzite crystal, with the stacking sequency ABCACB, and three inequivalent lattice sites. The 4H polytype has the stacking sequence ABCB, and carries two inequivalent lattice sites.

5.3.1. Extended defects

The silicon carbide crystal lattice can carry a multitude of different crystal defects, which can be grouped into different dimensionalities, from 3D defects to the zero-dimensional defects

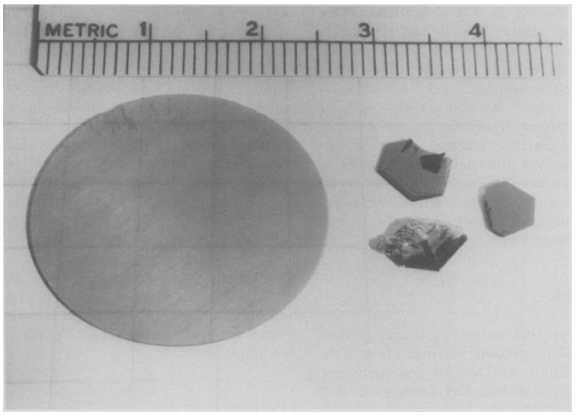

Figure 5.1.: Lely platelets from the 1950s, in contrast to a transparent (defect poor) Cree wafer from 1990. Image from [137].

(also called point defects). We will focus on the point defects, but the other defect classes (summarized as extended defects) will be briefly introduced here.

Three-dimensional defects consist mainly of large growth imperfections, like inclusions of foreign substances, gas or solvent remnants. From a quantum point of view, these defects can hamper the technical performance of the material, but do not influence the physical properties.

Two-dimensional defects are mainly crystal grain boundaries in a polycrystal, and are usually build from an ensemble of one-dimensional defects, which will be explained later. A grain boundary is the interface of adjacent, but differently oriented crystallites. Fig. 5.3 shows a strongly simplified sketch of the lattice including a grain boundary in a single-atom cubic lattice. One should notice, that in reality, grain boundaries consist not only of simple edge dislocations, as shown in the example, but can also comprise a complicated combination of screw dislocations.

As they influence mainly the SiC toughness and fatigue under high temperature [140], their genesis and their prevention (e.g. through temperature induced recrystallization) is mainly interesting for applications in high-power electronic devices, and will therefore not be discussed in detail.

One-dimensional defects consist of two major dislocation classes: The edge dislocation, and the screw dislocation. Edge dislocations are defined by an extra half plane introduced in the crystal, shifting the surrounding crystal planes (shown in Fig. 5.3) by the Burgers-Vector. A screw dislocation is more difficult to describe: A shift of one part of the crystal in respect to the other part by one atomic distance creates a screw-like arrangement of atoms along the dislocation line (the lattice singularity shown in Fig. 5.3). The models shown here are strongly simplified; in real crystals a combination/mixture of screw and edge dislocations impede an easy description of the whole crystal. The reason why they influence quantum applications of SiC are that they can be optically active, and therefore influence the pumping and readout

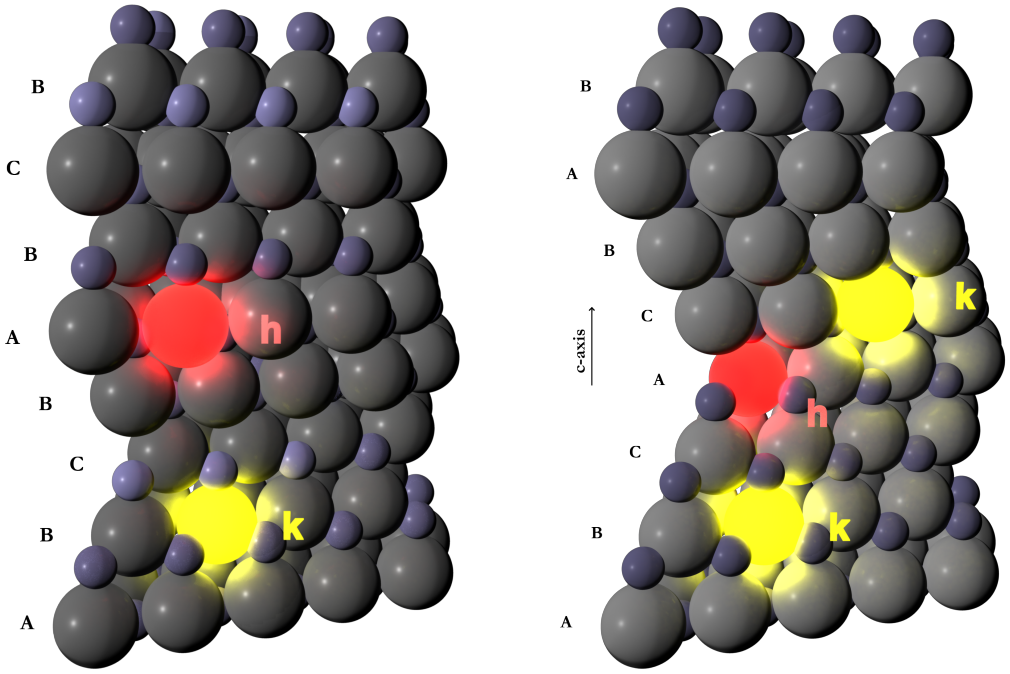

(a) 4H silicon carbide (b) 6H silicon carbide

Figure 5.2.: 4H and 6H polytypes of silicon carbide. The lattice stacking (4H: ABCB, 6H: ABCACB) and the possible unique silicon lattice positions (cubic: k, hexagonal: h) are highlighted. Silicon is grey and carbon is dark blue. The vertical axis is oriented along the principal crystal axis, also called c-axis. For another depiction, see fig. 5.28

of quantum centers. For example, Bergman et al. claim that the emission from 4H-SiC in the 420nm region stems from a stacking fault, which is in essence an extended dislocation defect [141, 142].

5.3.2. Point defects

The defects mostly relevant for quantum applications are, however, the zero-dimensional defects, or point defects. These include silicon and carbon interstitials, silicon and carbon vacancies, antisites and combinations thereof. One can distinguish two general classes of point defects:

i) Frenkel defect: An atom vacates its lattice position and moves into the lattice interstitial space.

ii) Schottky defect: An atom vacates its lattice position and travels to the crystal surface; leaving a vacancy defect.

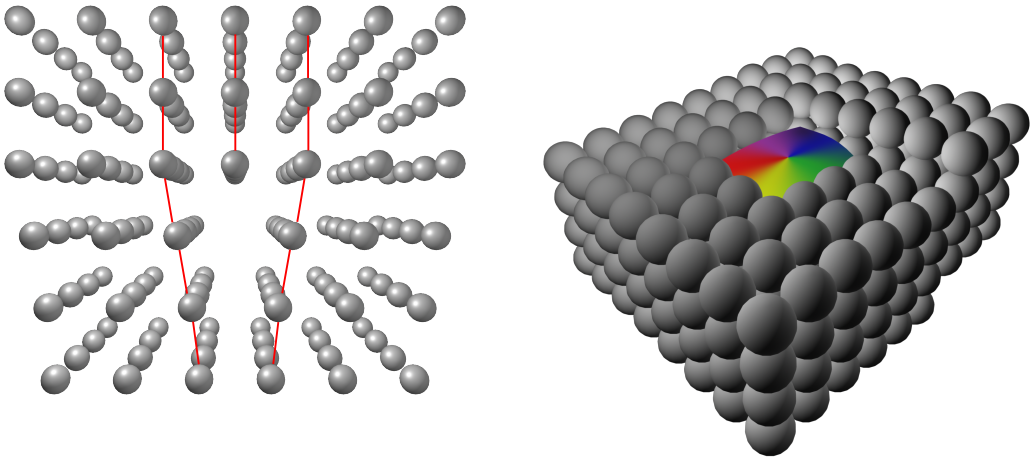

(a) (b)

Figure 5.3.: Extended defects. a) Edge Dislocation. In the fourth vertical lattice layer from the top, one layer of atoms vanishes. The lattice contorts to assume it's natural lattice constant. b) Screw dislocation. The multihued square is the location of the lattice singularity, around which the "screw thread" of lattice atoms revolve.

In more complex crystal lattices, these defects can additionally induce an electronic disorder, leading to charged defects, which are also visible in electron paramagnetic resonance (EPR) [143].

Point defects can be introduced either through the growing method (especially when using the Lely method) or by introducing irradiation damage. The silicon vacancy V_{Si} introduced by Lely growing was first observed in photoluminescence by Hagen and van Kemenade in 1974 [144]. For a more controlled manner of defect creation, silicon vacancies can also be created via electron irradiation [145] or neutron irradiation [146].

The sheer number of possibilities, in which these defect properties can be combined, lead to a multitude of different point defects in the silicon carbide crystal lattice; these additionally differ between the SiC polytypes. Just listing all of them, and their corresponding properties would break the mould of this document. We will therefore start with defects which are optically active, as these are the only ones which are accessible from a spectroscopic – and ultimately, from a quantum application point of view. To understand the upcoming results, the absorption and emission properties of crystal defects have to be briefly explained.

5.3.3. Zero phonon lines and phonon sidebands

A zero phonon line (ZPL), and its corresponding phonon sideband, are characteristic for the absorption and emission of chromophores embedded in a crystal lattice. Every individual

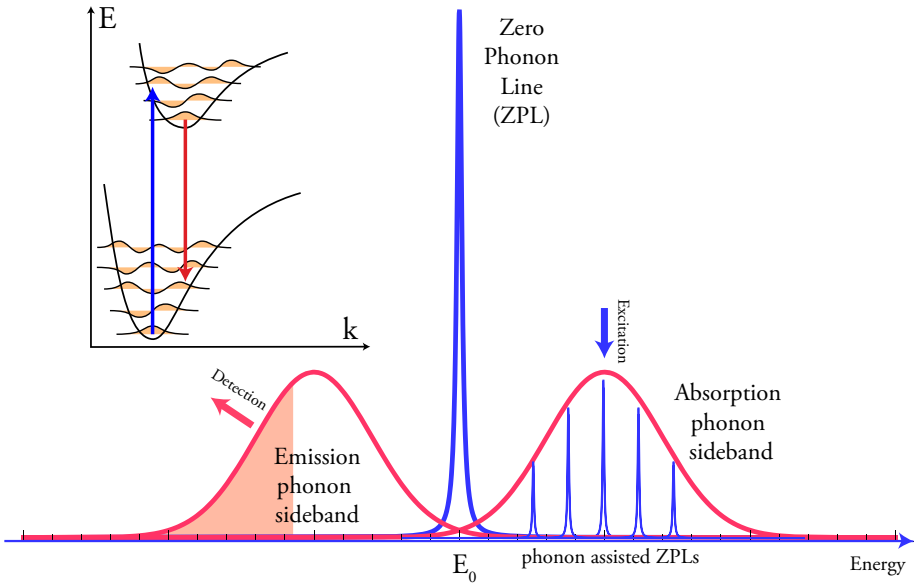

Figure 5.4.: Zero phonon line and phonon sidebands. The zero phonon line (ZPL) is the absorption/emission line of a color center without any disturbance from lattice phonons (T=0K). With phonons, individual color centers shift their ZPL according to the Franck-Condon principle (inset). These are here called phonon assisted ZPLs. Their ensemble creates the absorption/emission phonon sidebands. To better understand the pump cycle used in for most of the SiC experiments in this work (except the double resonance experiments), exemplary excitation and detection energies are indicated.

chromophore will emit its ZPL and sideband. In an ensemble of identical chromophores, this leads to an inhomogeneous broadening due to the differing lattice environment for each chromophore. The ZPL is spectrally located at an energy determined by the energy gap between ground and excited state, and only visible when phonons only play a minor role in the chromophores environment; i.e. at low temperatures. The phonon sideband stems from the Franck-Condon-Principle, leading to absorption into higher vibronic modes in the excited state, causing a blue-shifted absorption band, and emission into higher vibronic modes in the ground state, leading to a red-shifted emission band.

5.3.4. Photoluminescence of SiC defects

In fig. 5.5, the near infrared photoluminescence of the aforementioned 6H-SiC sample at T=4K and T=150K is shown. The first thing to notice when discussing the low temperature spectrum are the narrow, sharp lines. These are the zero phonon lines (ZPL) of the different defect types in the crystal.

In our 6H-SiC sample, the infrared region is dominated by four different lines, of which three are ascribed to silicon vacancies V_{Si} , matching to the three inequivalent lattice sites

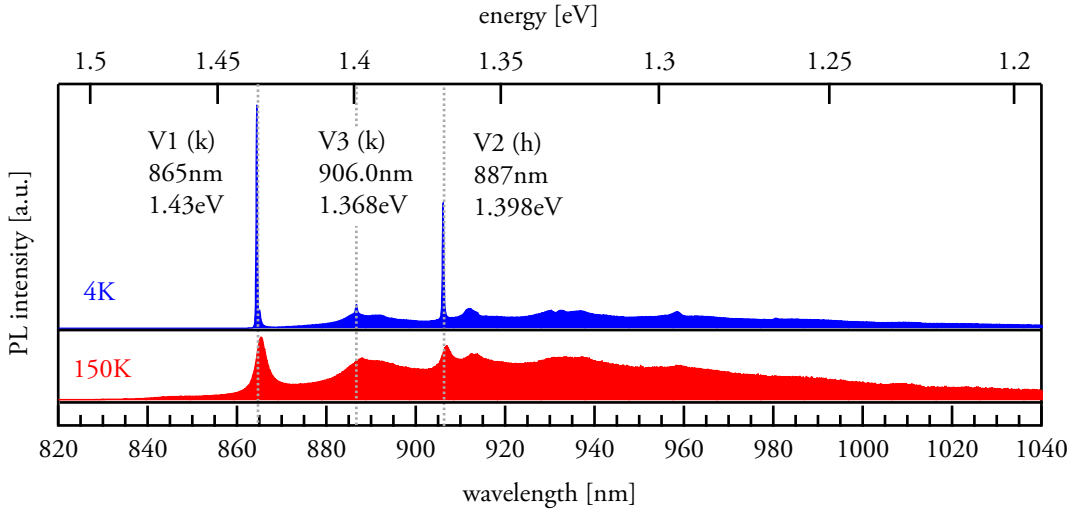

Figure 5.5.: Photoluminescence of neutron irradiated 6H-SiC at liquid helium temperature and higher temperature. The curve for T=150K is enlarged one order of magnitude. At low temperatures, the zero phonon lines are more pronounced, while at higher temperature, the phonon sidebands arise. The PL measurements were carried out by Franziska Fuchs [114].

possible in 6H (see fig. 5.2): The so-called V1 vacancy at 1.43 eV, V2 at 1.397 eV and V3 at 1.368 eV [147].

The origin of the fourth line is still under discussion, also in literature [148]; we will take a closer look in Ch. 5.7.1.

For the 4H (not shown), one could expect two V_{Si} lines from the two inequivalent lattice sites. Although one can identify the silicon vacancy defects, the V1 vacancy at 1.438 eV (862nm) and 1.352eV (917nm), the rest of the ZPLs is unaccounted for. In Literature, this is not discussed in detail, as the spectra are usually conveniently shown at higher temperatures T>10K, where most of the ZPLs except the silicon vacancy lines vanish [147].

The ZPLs of both polytypes are masked at room temperature, being overlaid by a very broad band which we attribute to a mixture of phonon sidebands from all participating defects in this spectral range. The higher overall amplitude of the emission at room temperature is due to the 633nm excitation not being in absorption ZPL resonance at low temperatures. At higher temperature the absorption phonon sideband arises and increases absorption, and ultimately, emission.

5.3.5. Defect isolation: zero field ODMR

To isolate one defect type out of this assortment, there are two possible approaches. The first possibility is to spectrally isolate one defect by resonantly exciting just the ZPL of one specific defect. This was done in [114], and will be discussed further in ch. 5.5. The main issue of

this approach is that here, the ZPL is only accessible at low temperatures – a caveat the zero field ODMR approach does not suffer from: Excitation of all defects through the phonon sidebands at room temperature, and subsequent selection of specific defects' spin transition by radio frequency resonance (explained in ch. 2.3.5).

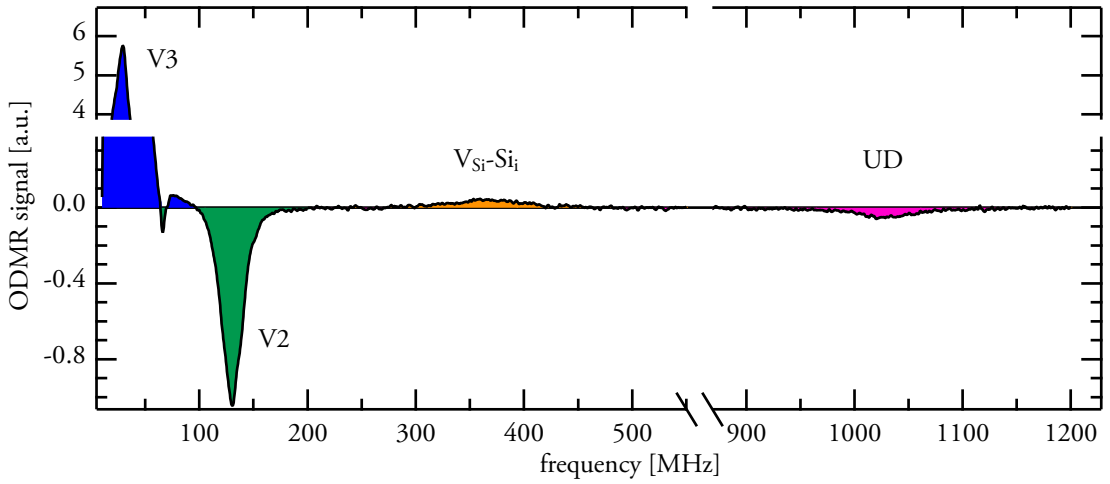

Figure 5.6.: ODMR resonances in 6H-SiC over frequency at zero magnetic field (Zero field (ZF)-ODMR) at room temperature. The strong broadening is due to the high incident microwave power $W = 2$W.

Fig. 5.6 shows the zero field ODMR signature of 6H silicon carbide. As excitation is done with a 785nm cw laser, all the defects with ZPL in the near infrared region (shown in fig. 5.5) are pumped. The individual defects are then isolated by their rf resonance, i.e. by inducing transitions between their Kramers doublets (separated by the zero field splitting D, ch. 2.1.4) through microwave quanta of matching frequency, which is in turn detected in the luminescence (see ch. 2.2.1).

6H-SiC shows four resonances for four defects, in tune with the results for low temperature photoluminescence. We stay with the nomenclature introduced by Sörman et al. in tentatively assigning the defects V3 to the silicon vacancy at the cubic lattice sites, and V2 to the hexagonal lattice site vacancy [149]. The fourth, unassigned signature will be discussed later in Ch. 5.7.

The broadening of the individual lines is dominated by the reduced lifetime broadening due to the high incident microwave powever (ch. 2.1.10. The other relevant broadening mechanisms are, on the one hand, due to the residual magnetic field in the range of 30μT; this leads only to a marginal Zeeman splitting of $\Delta\nu = 2$MHz. On the other hand, the specimens were not isotopically pure, which means the isotopes ^{29}Si and ^{13}C also contribute a signal at the main peaks' slopes. The hyperfine interaction splitting (ch. 2.1.9) for, e.g. the V2 defect accounts for sidebands at $\Delta\nu = \pm 4.5$MHz.

These zero field ODMR measurements help to find quantum defects in silicon carbide, which are able to be initialized and read out optically and whose spin states can be accessed by magnetic resonance – and therefore fulfill the second criterion of DiVincenzo. In the following we will further discuss the spin properties, especially in view of a possible qubit candidate.

5.4. Spin 1? Or maybe something else?

Three things cannot be long hidden: the sun, the moon, and the truth.

— Buddha

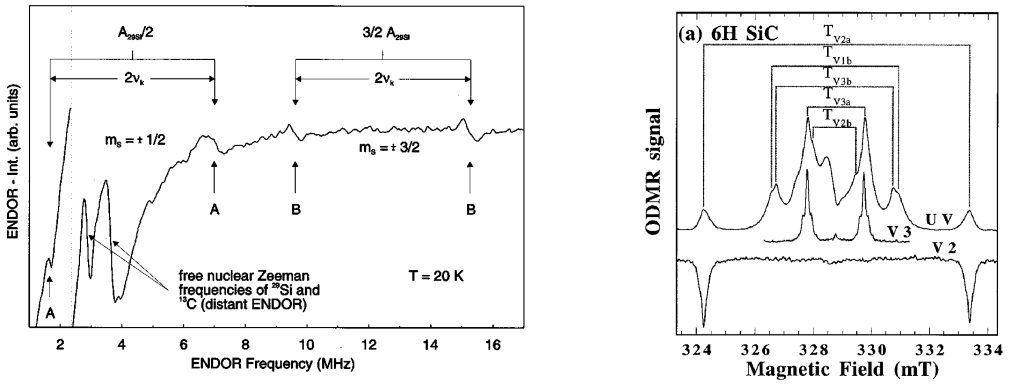

(a) (b)

Figure 5.7.: a) ENDOR spectrum of 4H-SiC on the EPR silicon hyperfine line. Lines labeled B are linked to $m_S = \pm 3/2$, while A are $m_S = \pm 1/2$. Reproduced from [150]. b) ODMR of 6H-SiC. The curve labeled UV is excited above-gap, the spectra labeled V2 and V3 are excited resonantly to the corresponding defects. Reproduced from [149].

A long lasting discussion in the silicon carbide community revolves around the multiplicity of the spin ground state of the silicon vacancy defects. The importance of this question, aside from scientific curiosity, will be elucidated when we discuss the pumping schematic of SiC, and the possibilities unique to a quartet high spin system in ch. 5.6.

For 4H-SiC, Wimbauer et al. identify the spin state of the negatively charged silicon vacancy V_{Si}^- to be $S = 3/2$, by using electron-nucleus double resonance (ENDOR) [150]. ENDOR spectra resonances are calculated with the following solution of the EPR spin hamiltonian 2.1:

$$h\nu_{\mathrm{ENDOR}} = -g_{\mathrm{Nuclear,Si}}\mu_{\mathrm{Nuclear}}B_0 + m_S A_{\mathrm{Si}} \tag{5.1}$$

From this equation an easy proof for $S = 3/2$ can be deducted. In ENDOR, a spin quartet should yield four resonances; the latter being observed in [150] (fig. 5.7a). Also, Zywietz et al. predicted the high spin state as energetically favorable with first-principle calculations [151].

5.4.1. The spin 1 empire

Also, Sörman and Son accept the V_{Si}^{-} to be a quartet high-spin in [149]. Nevertheless, they identify the luminescent V1, V2, V3 defects as $S = 1$ spin triplets, and therefore discount the possibility that they are connected to V_{Si}^{-}, based on the preceding EPR experiments which clearly state $S_{V_{Si}^{-}} = 3/2$. They subsequently link the states to the neutral silicon vacancy V_{Si}^{0}, and name them T_{V1a}, T_{V2a} and T_{V3a}, where T denominates the triplet spin state, and the a standing for the center allowing for resonant optical excitation.

This model was supported by a pulsed EPR study by Orlinski, Baranov et al., where they convincingly assign $S = 1/2$ to V_{Si}^{+}, $S = 1$ to V_{Si}^{0} and $S = 3/2$ to V_{Si}^{-} [152]. They derive the assignment of the triplet to V_{Si}^{0} from the matching of their EPR lines to the ODMR of Sörman [149], and the absence of the quartet center transition $|3/2, -1/2\rangle \longleftrightarrow |3/2, +1/2\rangle$ at $B \approx 335$mT.

Using conventional EPR, we were also able to detect the low and high field transitions of V2, but could neither disprove nor reconstruct the quartet's center field transition at $B = 335$mT, due to the superimposing light independent EPR signal of nitrogen impurities (Fig. 5.8). At first glance, we come to the same conclusions as the other triplet proponents.

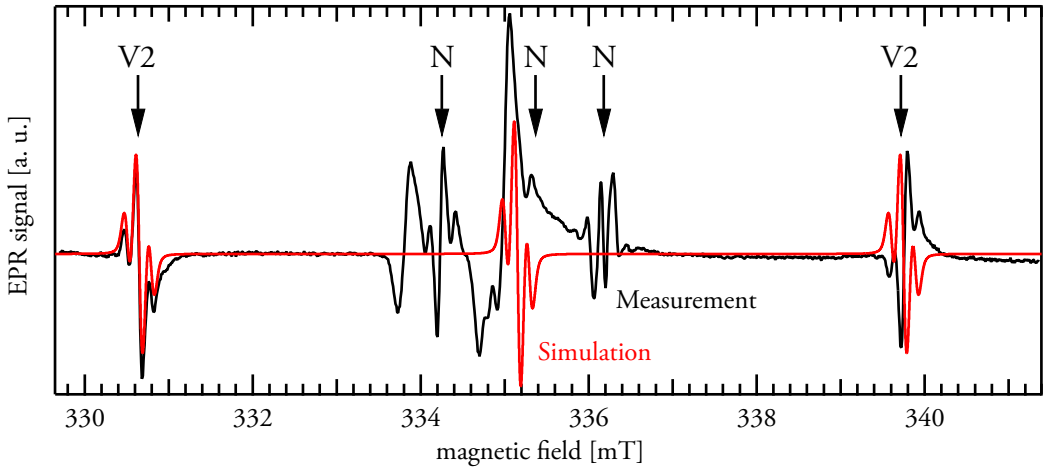

Figure 5.8.: Light induced EPR of 6H-SiC measured at T=4K under resonant excitation of the V2 ZPL (black line), with B||c-axis, and a tentative simulation using $S = 3/2$ with $D = 127\,MHz$, taking into account the isotope hyperfine interaction. The inversion of the high field signal will be discussed in ch. 5.6. Note how the supposed $|3/2, -1/2\rangle \longleftrightarrow |3/2, +1/2\rangle$ center transition is superimposed by the nitrogen impurity signals.

5.4.2. The high spin rebellion

Contrarily, Mizuochi and coworkers show another pulsed ENDOR study, specifically aimed at the so-called T_{V2a} defect, and identify a $S = 3/2$ quartet state [153]. They position their results against the triplet model of Sörman, Son and Baranov, with a very clear wording:

> *"[…] clearly indicate that the spin multiplicity of T_{V2a} is quartet and not triplet ($S = 1$)."*

However, they base their findings on ENDOR, which provides no unambiguous link to the optically active states discussed by Sörman. Nevertheless, the relevance of this study is increased when Mizuochi later, together with Son and coworkers, uses pulsed double electron-electron resonance (DEER, also known as P-ELDOR), to detect the missing $|3/2, -1/2\rangle \longleftrightarrow |3/2, +1/2\rangle$ transition [154]. This line is not illumination dependent, and therefore invisible to the ODMR study in [149].

To summarize: There was no consensus concerning the spin ground state and the charge nature of the silicon vacancy V2 in 6H-SiC, and additionally, there are no further studies we are aware of concerning V1 and V3 in 6H-SiC, and also for V1 and V2 in 4H-SiC. Using conventional EPR, it is challenging to single out a specific state to clarify its spin properties, due to the presence of a multitude of different defects in silicon carbide.

In the following chapters, we intend to clear up this enduring question, and use our learnings about the spin states to propose interesting applications of the IR active defects.

5.5. Fingerprint of a spin $\frac{3}{2}$ system

5.5.1. Double radio-optical resonance

Our approach to clarify the spin multiplicity of the V2 ground state, is to try to address only the light sensitive defects by using the double radio-optical resonance method. Here, a very narrow bandwidth excitation is used, using a Sacher Lion laser system with a linewidth <1MHz. This allows to resonantly excite into a single zero phonon line, which is unique to every silicon vacancy defect type, and has a very narrow linewidth at low temperatures (see ch. 5.3.3). The ZPL linewidth of the V2 defect has been ascertained by resonant light induced EPR by Riedel, Fuchs, Astakhov, myself and coworkers in [114], to be in the range of 200 μeV at $T = 50K$. At lower temperatures, the V2 ensemble then splits into a forest of very narrow ZPLs individual for each single defect (see ref. [114], fig. 2). This discretization is ascribed to the individual defects' local environments differing slightly. The linewidth of such a single ZPL can be as low as $2\mu eV$. This suggests that we are resonantly exciting small ensembles or even single defects, as this linewidth can be expected for single defects [155].

This method solves the problem of discerning single defect types mentioned in the last chapter. It allows to look at the spin properties of a single defect class, of its ground and excited states. A first EPR example was already shown in fig. 5.8, where we already mentioned the detrimental effect of nitrogen impurities.

5.5.2. Light-dependent EPR reconstruction by sideband demodulation

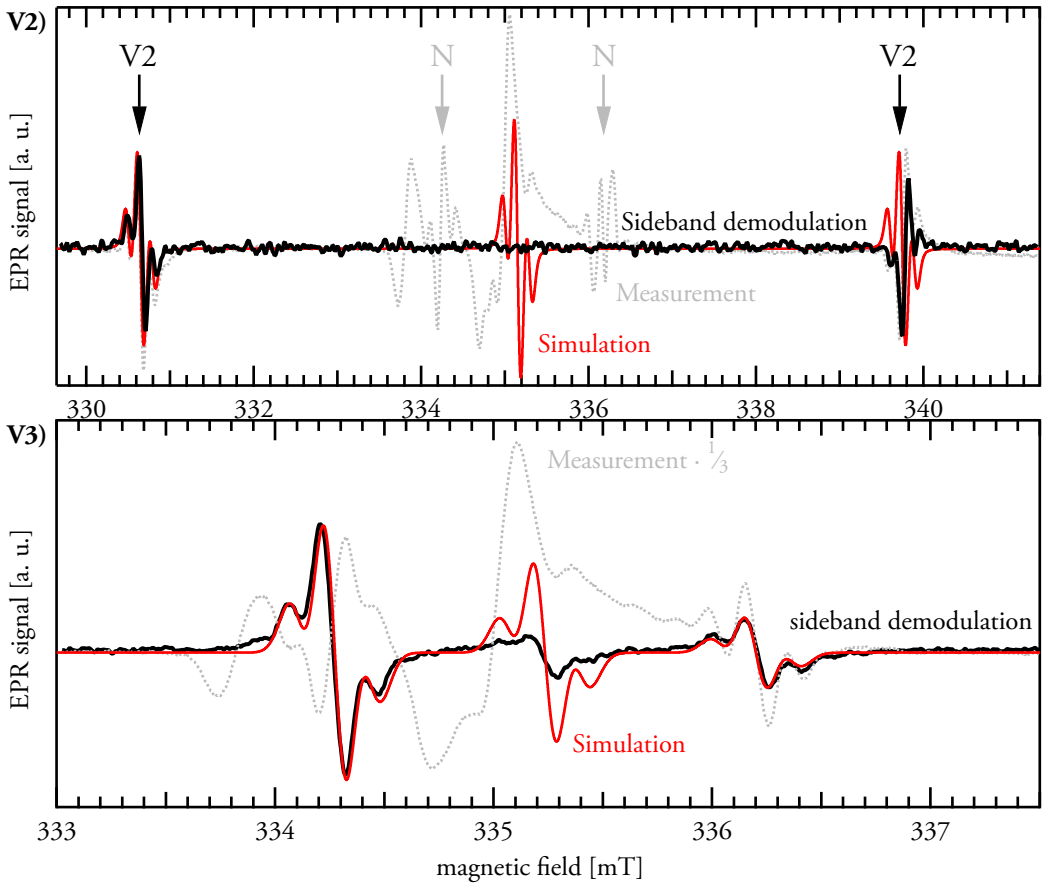

Figure 5.9.: Light induced EPR of 6H-SiC with sideband demodulation, measured at T=4K, with conventional EPR in grey, and the simulation in red (compare to fig. 5.8). The magnetic field is modulated by a $f_1 = 100\text{kHz}$ carrier wave, and the excitation wavelength is centered on the corresponding ZPL slope, and modulated by $\Delta\lambda = 143\text{pm}$ at $f_2 = 280\text{Hz}$. The EPR signal is reconstructed from the lower f_2 sideband of f_1. **V2)** Resonant excitation of V2. Note the vanishing light independent nitrogen signature, and the absence of the quartet center transition. **V3)** Resonant excitation of V3. Here, the quartet center transition is weak, but traceable.

One possibility to alleviate the problem of light independent EPR signals was the introduction of a sideband demodulation technique. Here, the lock-in amplifier is locked onto the carrier frequency of the external magnetic field modulation of 100kHz. Additionally, the excitation wavelength is modulated by 143pm with a 280Hz sinus. The excitation modula-

tion center frequency is then set to a slope of the corresponding ZPL, to achieve a maximum difference in EPR signal at the modulation extrema. This creates two sidebands on the carrier modulation, which can be reconstructed by the Zurich Instruments HF2LI lock-in amplifier's sideband demodulation; effectively leaving only light dependent signals [156].

Alas, for the **V2 defect**, no trace of the $|3/2,-1/2\rangle \longleftrightarrow |3/2,+1/2\rangle$ signal can be seen in fig. 5.9 (top). The problem is the same as stated in [154]: The center quartet transition is very weak, hinting a small population difference of the participating states. However, the simulation parameter for the zero field splitting $2D_{V2} = 127.5$MHz coincide very well with the literature values (see table 5.2). The smaller EPR transitions on the slope of the main transitions stem from the hyperfine interaction (HFI) with the $I = 1/2$ nuclei of the ^{29}Si, which are considered with a isotropic HFI tensor of $A_{\mathrm{HFI},^{29}\mathrm{Si}} = 8.5$MHz.

The same was attempted on the **V3 defect** (fig. 5.9 bottom), whose EPR signal is completely superimposed by the nitrogen defects. Here, the center excitation wavelength was set to the slope of the V3 ZPL. The sideband demodulation reveals a spectrum with three transitions, with a detectable $|3/2,-1/2\rangle \longleftrightarrow |3/2,+1/2\rangle$ transition. The simulation again matches the expected value for $D_{V3} = 27.3$MHz, and includes $A_{\mathrm{HFI},^{29}\mathrm{Si}} = 7.8$MHz. . Therefore, at least for the V3 defect, the light induced EPR can corroborate the assumption of an $S_{V3} = 3/2$ spin quartet.

5.5.3. Low temperature optically detected magnetic resonance (ODMR) of the V2 defect

Another opportunity to single out light dependent signals is to use optically detected magnetic resonance (ODMR), which is by principle insensitive to light independent signals. The fundamentals of ODMR are discussed in ch. 2.2. In combination with resonant excitation, this method yields only the participating spin signatures of the tuned in species.

Firstly, the V2 ZPL is excited resonantly at $T = 4$K, and the – at low temperature very small – red shifted residual phonon replica emission is detected after a $\lambda > 900$nm laser cutoff. An external magnetic field $B \parallel c$-Axis of the 6H-SiC crystal is sweeped, while the sample is exposed to square-wave modulated X-band microwaves ($\nu_{\mathrm{microwave}} = 9.43$GHz). The general experimental setup is described in more detail in ch. 2.3.2. The resulting spectrum is shown in fig. 5.10, together with the corresponding $S = 3/2$ Zeeman energy scheme.

The principal full field transitions, marked with $\pm$ and positioned at a distance of $\frac{4D_{\mathrm{V2,gs}}}{g_e \mu_B}$ ($2D_{\mathrm{V2,gs}} = 127.5$MHz) around the free electron g-factor $g = 2.0023$ could be also interpreted as a triplet signature, again because of the missing center $|3/2,-1/2\rangle \longleftrightarrow |3/2,+1/2\rangle$ transition, as already shown in conventional EPR.

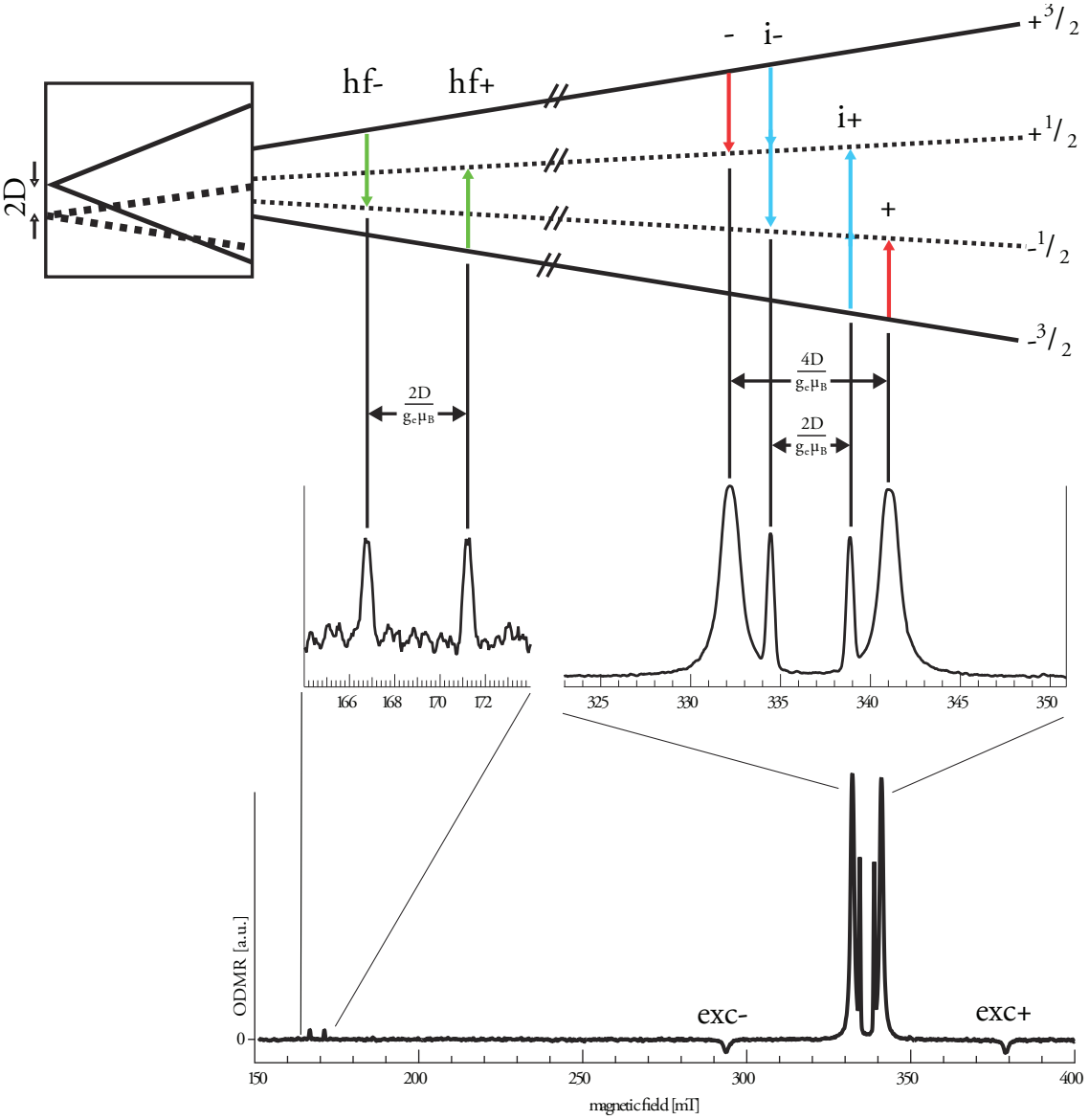

Figure 5.10.: ODMR signature of the V2 defect in 6H-SiC. The ODMR spectra were measured with the excitation tuned to the V2 ZPL ($E_{V2} = 1.397$eV). The external magnetic field B was parallel to the crystal c axis, and the microwave frequency was $\nu = 9.43451$GHz. The annotated transitions are the half field transitions hf$\pm$, the principal transitions $\pm$ and the two-photon transitions i$\pm$. Measurements done by Daniel Riedel [115]

5.5.4. Two quantum transitions in the V2 defect

However, with the increased sensitivity and specificity of ODMR, other transitions can be detected. The transitions marked $i\pm$ which are at half width of the full field transitions $\frac{2D_{\mathrm{V2,gs}}}{g_e \mu_B}$ can be interpreted and simulated as two photon transitions between $|{}^3/_2, -{}^1/_2\rangle \leftrightarrow |{}^3/_2, +{}^3/_2\rangle$ and $|{}^3/_2, +{}^1/_2\rangle \leftrightarrow |{}^3/_2, -{}^3/_2\rangle$. These $\Delta m_S = \pm(1+1)$ transitions are in principle forbidden at first order, but are made possible due to the exceptionally high incident microwave power of $P = \frac{1}{4} P_{\mathrm{max}} = 0.5\,W$; which is also responsible for the line broadening rendering the isotope transitions observed in fig. 5.9 invisible. The power dependency of the SiC ODMR will be discussed in detail in 5.6.4. These transitions are impossible to explain using a triplet scheme, because the triplet would only yield one transition $|1,-1\rangle \leftrightarrow |1,+1\rangle$ at $g \approx 2$.

To theoretically explain these two quantum transitions, one has to fall back on time-dependent perturbation theory. The transition is possible, if the second order perturbation is considered, as it provides an intermediate state to facilitate two transitions with half the Zeeman energy distance between e. g. $|\phi_n\rangle = |{}^3/_2, -{}^1/_2\rangle$ and $|\phi_m\rangle = |{}^3/_2, +{}^3/_2\rangle$ [157, 158].

First order perturbation theory. The probability amplitude of the system being in the state $|\phi_m\rangle$ after a time t is, in the first order:

$$\langle \phi_m | \psi(t) \rangle_{\mathrm{FO}} = \frac{1}{i\hbar} \int_{-t}^{+t} \mathrm{d}t' \, e^{\frac{i(E_m - E_n)t'}{\hbar}} \langle \phi_m | \mathscr{H}'(t) | \phi_n \rangle \tag{5.2}$$

With the Hamiltonian in the Dirac interaction picture being $\mathscr{H}(t) = \mathscr{H}_0 + \mathscr{H}'(t)$, and the time independent part $\mathscr{H}_0$ being the electron Zeeman interaction term in Eqn. 2.1. The perturbation term $\mathscr{H}'(t)$ in 5.2 is

$$\mathscr{H}'(t) = \mu_{\mathrm{Bohr}} g_J \hat{J} \vec{B}_1(t) \tag{5.3}$$

Here, g_J is the atomic g-tensor, $\hat{J}$ is the angular momentum and B_1 the internal magnetic field of the microwave radiation. As the latter is the only time dependent term $\vec{B}_1(t) = \vec{B}_1 e^{-i\omega t}$, the whole perturbation term can be contracted to

$$\mathscr{H}'(t) = \mathscr{H}'(0) e^{-i\omega t} \tag{5.4}$$

so eqn. 5.2 can be rewritten as

$$\langle \phi_m | \psi(t) \rangle = \frac{1}{i\hbar} \langle \phi_m | \mathscr{H}'(0) | \phi_n \rangle \int_{-t}^{+t} \mathrm{d}t' \, e^{\frac{i(E_m - E_n)t'}{\hbar}} e^{-i\omega t'} \tag{5.5}$$

$$= \frac{1}{i\hbar} \langle \phi_m | \mathscr{H}'(0) | \phi_n \rangle \, \frac{e^{-i\omega t + i(E_m - E_n)t' \hbar^{-1}} - 1}{-i\omega + i(E_m - E_n)t' \hbar^{-1}} \tag{5.6}$$

When the rf photon frequency ω is near the Bohr frequency of the transition, and t is sufficiently small, the right term just leaves a simple t dependence, and the one quantum transition is possible.

$$\langle \phi_m | \psi(t) \rangle = \frac{t}{i\hbar} \langle \phi_m | \mathscr{H}'(0) | \phi_n \rangle \tag{5.7}$$

Still, the transitions observed in ODMR are far from the resonance positions of the single photon transitions. To find allowed transitions at these positions, the scope has to be extended to second order transitions.

Second order perturbation theory. Similar to first order perturbation theory, we consider the probability amplitude, but this time with another intermediate state ϕ_l in between ϕ_n, ϕ_m:

$$\langle \phi_m | \psi(t) \rangle_{\mathrm{SO}} = \frac{-1}{\hbar^2} \int_{-t}^{+t} \int_{-t}^{+t'} \mathrm{d}t' \mathrm{d}t'' \, e^{\frac{i(E_m - E_l)t' + i(E_l - E_n)t''}{\hbar}} \langle \phi_m | \mathscr{H}'(t) | \phi_l \rangle \langle \phi_l | \mathscr{H}'(t) | \phi_n \rangle \tag{5.8}$$

With the same contractions and modifications as shown for the first order perturbation, the integrals can be solved to

$$\langle \phi_m | \psi(t) \rangle_{\mathrm{SO}} = \frac{-1}{\hbar^2} \frac{\langle \phi_m | \mathscr{H}'(0) | \phi_l \rangle \langle \phi_l | \mathscr{H}'(0) | \phi_n \rangle}{-i\omega + i(E_l - E_n)/\hbar} \times \left(\frac{e^{-2i\omega t + i(E_m - E_n)t/\hbar} - 1}{-2i\omega + i(E_m - E_n)/\hbar} - \frac{e^{-i\omega t + i(E_m - E_l)t/\hbar} - 1}{-i\omega + i(E_m - E_l)/\hbar} \right) \tag{5.9}$$

Here, the resonance of the principal $\langle \phi_m | \phi_n \rangle$ transition is determined by the dominant resonance denominator (marked blue in eqn. 5.9), which resolves to $2\omega\hbar = E_m - E_n$.

This, in comparison with the one quantum transition resonance $\omega\hbar = E_m - E_n$, tells that in this transition, two quanta with identical energies are involved. Furthermore, with half transition energy the transition linewidth $\Delta\nu_{i\pm} = 11.2\,\mathrm{MHz}_{\mathrm{Gauss}} + 8.13\,\mathrm{MHz}_{\mathrm{Lorentz}}$ should be half of the full field transitions' linewidth $\Delta\nu_{\pm} = 22.4\,\mathrm{MHz}_{\mathrm{Gauss}} + 16.3\,\mathrm{MHz}_{\mathrm{Lorentz}}$, which is the case.

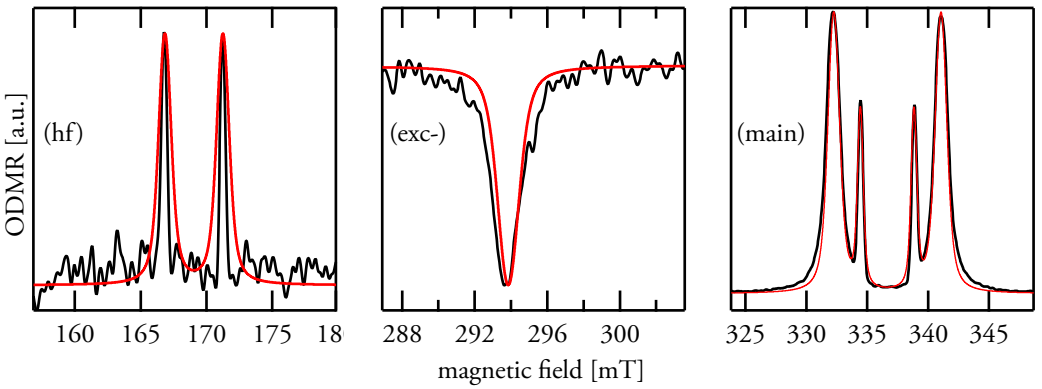

Figure 5.11.: Simulation of the V2 defect ODMR in 6H-Sic. The half field (**hf**) and full field (**main**) transitions are both described by a simulation of a $S = 3/2$ quartet system with $D = 127.5$MHz, the excited state quartet has $D_{exc} = 1240$MHz. The curves with a slightly ($+10\mu$eV) detuned excitation were left out; they show a zero line. Spectra recorded by D. Riedel, simulations by the author.

Caveat. The interpretation of a equienergetic two quantum transition seems to hold for this case. However, there are also transitions documented in literature which are at the same resonance position where you expect a double quantum line, but which behave like multiple single quantum transitions in both power dependence and linewidth [159]. This is excluded in the SiC case, as both linewidth and power dependence match the two quantum assumptions.

Another simplification to keep in mind is the high microwave B_1 field, which can not be interpreted as a small perturbation any more. Therefore, quantifying the results using second order perturbation theory should be treated with utmost respect.

5.5.5. Irrefutable and straightforward evidence: The half field transition

The final proof for a high spin transition is the, albeit weak, but still incontestable existence of the two half field transitions at $B_{\text{hf-,V2}} = 167\,\text{mT}$ and $B_{\text{hf+,V2}} = 171\,\text{mT}$. The only scenario where more than one half field transition can be detected is in a high spin system with $S > 1$. After correcting for the magnetic field nonlinearity, the simulation shown in fig. 5.11 matches the half field transition to the zero field splitting observed for the full field transitions $\pm$ and the two quantum transitions i$\pm$ shown in fig. 5.10.

This is already the unambiguous proof of the V2 defect system being in a $S = 3/2$ quartet ground state. It therefore identifies with the negatively charged V_{Si}^- vacancy.

The issue that a V_{Si}^- defect should have no zero field splitting due to its symmetry is discussed in ch. 5.9.2.

5.5.6. Excited V2 defect

Not all transitions seen in fig. 5.10 are described by the ground state $S = 3/2$ canon. The transitions $B_{\text{exc-,V2}} = 293.8\,\text{mT}$ and $B_{\text{exc+,V2}} = 293.8\,\text{mT}$ are also depending on the V2 ZPL resonant excitation; they vanish when exciting off resonance. However, the different sign and far greater zero field splitting of $D_{\text{exc,V2}} = 1240\,\text{MHz}$ signifies them not being part of the ground state manifold. The simulation shown in fig. 5.11 is only possible with an $S = 3/2$ quartet. Simulating a triplet is only feasible when severely changing the spin system g-factor, far away from the free electron $g = 2.0023$, which is the g-factor for all other observed SiC systems. Hence, ontological parsimony dictates to attribute this transition to the excited state manifold of the 6H-SiC V2 defect. This assumption is corroborated by the broader linewidth of $\Delta\nu_{\text{exc}\pm} = 28.0\,\text{MHz}_{\text{Gauss}} + 19.6\,\text{MHz}_{\text{Lorentz}}$, indicating a shorter lifetime of the corresponding state. In diamond NV centers, an excited state is also reported to have a shortened lifetime in comparison to the ground state [160].

5.6. Room temperature ODMR and microwave emitters

> *The game has changed now, with works by Stefania Castelletto et al. and Hannes Kraus et al. who have isolated single emitters and identified microwave spin qubits in silicon carbide.*
>
> — Igor Aharonovich and Milos Toth, in [161]

To summarize the last chapter, the spectrum in fig. 5.10 clears up the question whether the V2 vacancy in 6H-SiC, which is commonly associated with the vacancy at the hexagonal lattice site, is a spin triplet or a spin quartet in favor of the latter assumption. The defect can hence be identified with the negatively charged silicon vacancy V_{Si}^{-}, and it can be initialized, addressed and read out individually. It therefore meets already some of DiVincenzos criteria, save one: scalability. The measurements shown until now were taken at liquid helium temperature, with an ultra narrow bandwidth tunable laser system. This does not bode well for large scale application.

In this chapter, the same interesting spin properties will be exploited at ambient temperature; furthermore we will adress the not yet discussed 6H V3 defect, and the 4H V1 and V2 defects.

5.6.1. ODMR of 6H-SiC at ambient conditions

As a first step, we will extend from the already introduced 6H silicon carbide. Fig. 5.12 shows the full field ODMR of the 6H-SiC at room temperature. The most noteworthy experimental

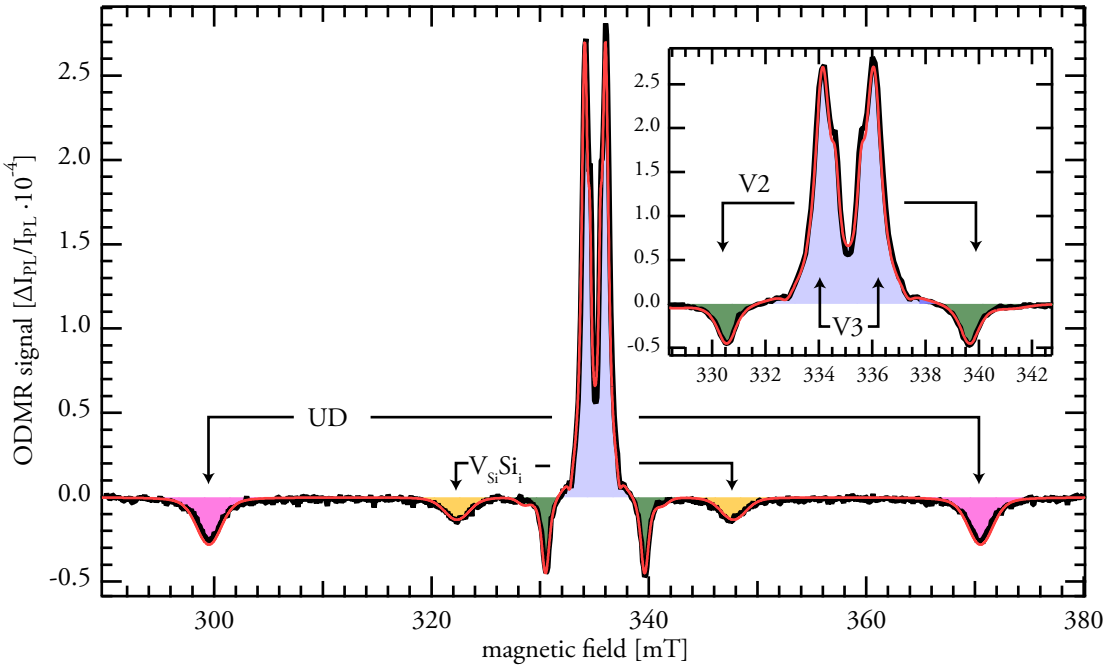

Figure 5.12.: Full field ODMR of 6H-SiC at ambient temperature. Excitation with 785nm. Experimental spectrum in black, simulation (parameters in table 5.2) in red. The inset is a zoom of the environment of g=2. Here, B || c-axis.

difference in comparison to the measurements in fig. 5.10 is the excitation, which is now situated at the higher energy of $E = 1.58$eV (785nm). As the zero phonon lines of 6H-SiC vanish at $T = 300$K, the defects are now absorbing and emitting only in their corresponding phonon replicae (see fig. 5.5). Therefore, the 785nm light excites all defects working in the near IR, similar to the zero field ODMR defect screening already described in ch. 5.3.5. Unlike in the zero field, the full field ODMR allows for spectrally separating the defects due to their large differences in zero field splitting D. The spectrum shows four major contributions (from the center – increasing ZFS D):

1. The V3 defect with a positive $\Delta I_{\mathrm{PL}}/I_{\mathrm{PL}}$ sign
2. The V2 defect with a negative $\Delta I_{\mathrm{PL}}/I_{\mathrm{PL}}$ sign
3. The Frenkel pair with a silicon interstitial $V_{\mathrm{Si}} - \mathrm{Si}_i$
4. The unassigned defect UD

We will first expand on the former two, while the latter two will be discussed in ch. 5.7.

The V2 defect has been already studied minutely, and will hence be discussed first. The zero field splitting D of the simulation shown in fig. 5.12 match the low temperature case (fig. 5.11), the EPR measurement (fig: 5.9) and the literature values to a tee. The linewidth changes according to expectations: The lorentzian linewidth increases, as the lifetime gets shorter with higher temperature, leading to higher natural (homogeneous) broadening. The inhomogenous gaussian broadening stems from the high incident microwave power of $P = P_{\mathrm{max}} = 2\mathrm{W}$, wherein the unresolved hyperfine interaction with the ^{29}Si isotope are also lost. The two photon transitions vanish in the much stronger V3 signature; they are also expected to be weaker also due to the states' shorter lifetime [158]. The corresponding half field transitions have also been observed in 5.13.

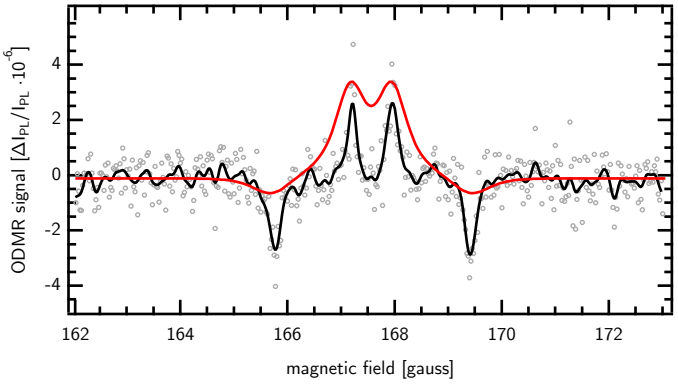

Figure 5.13.: ODMR of the half field transition of 6H-SiC of V2 and V3 at room temperature. The measurement was not done together with fig. 5.12, and the sample was slightly tilted. For the simulation, this was corrected by including a shift of $\vartheta = 21.2°$, which fits the shown half field spectrum and the corresponding full field spectrum (not shown). The intrinsic parameters are the same as in fig. 5.12.

The V3 vacancy located at one 6H cubic lattice site dominates the spectrum, also expressing two quantum and half field transitions. This again unambiguously asserts the quartet multiplicity of the V3 defect. A salient quality is the much stronger rf resonant response for the V3 contribution in comparison to V2 and the other defects. This strong response is also visible in room temperature EPR, shown in fig. 5.14, and additionally the EPR shows a signal inversion of one transition.

5.6.2. RF emission of vacancy defects

The room temperature light induced EPR, with excitation into the phonon sideband, is similar to the room temperature ODMR, in the respect that one observes all excitable transitions in

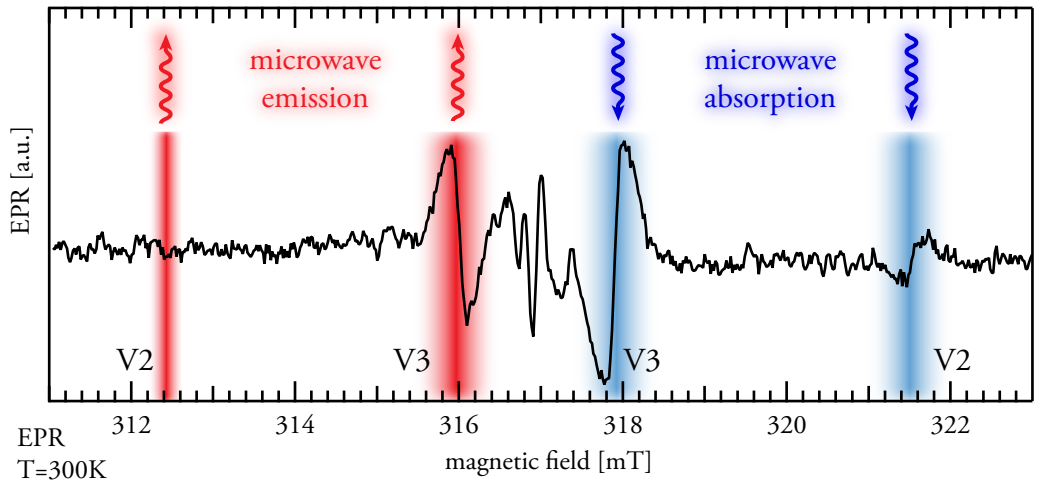

Figure 5.14.: Light-induced EPR of 6H-SiC at room temperature. Excitation with 808nm, curve recorded as microwave absorption first derivative. The transition positions are from the simulation with values derived from fig. 5.12, adapted to this measurements microwave frequency $\nu_{mw} = 8.9\,\mathrm{GHz}$. The V3 low field transitions' signs are inverted, signifying a microwave emission. The measurement was performed by Victor Soltamov at the IOFFE institute St. Petersburg.

one ODMR measurement. The transitions in the spectrum shown in fig. 5.14 are located at the same magnetic field positions as in low and room temperature ODMR, save the adaptation to the different rf frequency in the IOFFE experimental setup. The simulation parameters are the same as in our ODMR and EPR experiments (table 5.2), so we can assign the transitions seen here to the V2 and the V3 silicon vacancy. The striking feature of this spectrum is the signal inversion of the low field transitions, which we already could observe for V2 in fig. 5.9.

The inversion of the signal can be interpreted as the lower field transitions being microwave emitting, while the higher fields are absorbing. This behaviour is most prominent in the V3 signature, while in V2 the low field transition vanishes because the spin pumping and the spin relaxation compensate each other.

5.6.3. A shelving state

To construct an excitation schematic which explains this behaviour, a system with at least three levels has to be considered. Microwave emission necessitates a polarization of the spin substates. As spin conservation forbids the spin-polarized direct repopulation of the ground state after excitation, the existence of a metastable third level, a so-called *shelving state*, is a prerequisite. A strong indication of an at least three level system is given in fig. 5.15.

Here, a correlation measurement was carried out at room temperature on 6H-SiC. The interpretation of a correlation measurement relies on the quantum interpretation of the Han-

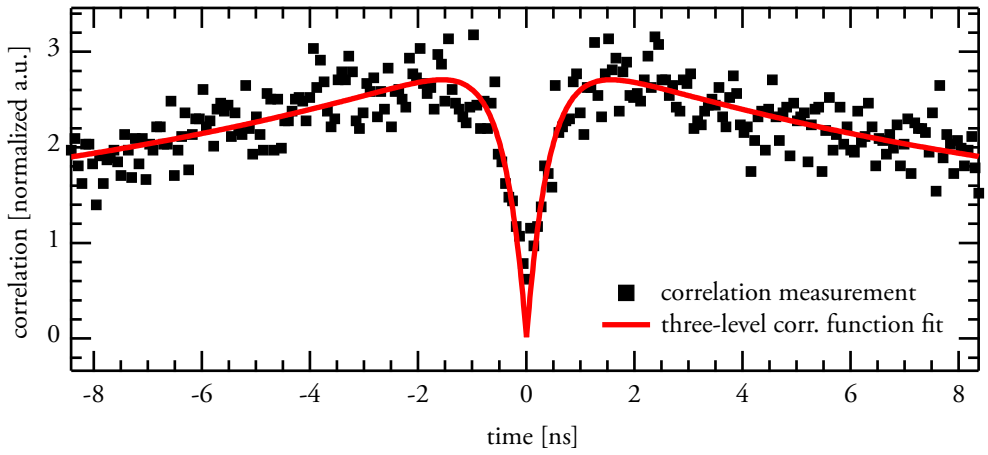

Figure 5.15.: Correlation measurement on 6H-SiC with a 785nm excitation power of 0.3mW. The fit was made with a correlation function based on a three level system [146]. The measurement was done by Franziska Fuchs and Benedikt Stender.

bury Brown and Twiss effect, where two detectors observe the same beam from a light source simultaneously. Strongly simplified, if the light source is a single photon source, it is quantum mechanically impossible to detect a photon on both detectors at the same time: At delay times between the two detectors nearing zero, the *antibunching* tentatively shown here is detected [162]. Discussing single photon emission from SiC is beyond the scope of this work; F. Fuchs et al. and Castelleto et al. have already shown single photon emission from SiC [146, 163]. The interesting feature for this discussion is the photon bunching behaviour exceeding a correlation of 2 around the antibunching signal dip. The correlation function to explain this curve shape has to consider at least three participating states [164, 165], which proves the existence of a third, metastable shelving state in the excitation kinetic of the silicon vacancy in SiC [146].

5.6.4. RF power dependence

Another building block to figure out the excitation kinetics of the SiC silicon vacancy is the dependence of the signal shape on the incident rf power. The EPR saturation method has been traditionally used to get an estimate of the T_2 spin-spin relaxation time, when a pulsed EPR method is not available [166, 167]. In [115], we use a standard EPR approximation to model the rf power dependence of both signal amplitude and linewidth for the low temperature ODMR of 6H-SiC. At ambient temperature, the data in fig. 5.16 can be interpreted in a similar, albeit more qualitative manner. The signal amplitudes of the principal $\pm$ transitions behave as expected. At low temperatures, the linewidths of these increase linearly with the incident rf power, without approaching saturation range (ref. [115] fig. 3). However at room

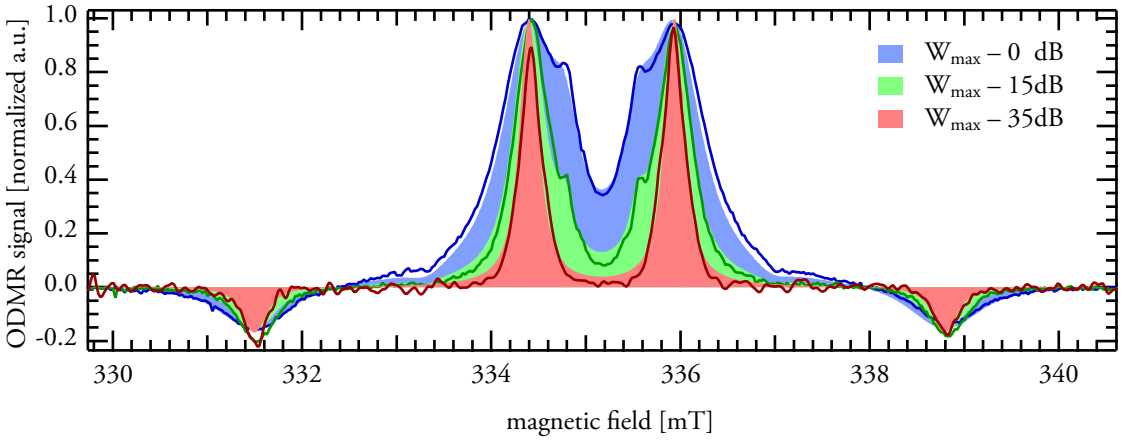

Figure 5.16.: RF incident power dependence of the ODMR of 6H-SiC at room temperature. Three exemplary ODMR spectra at different incident rf powers (lines) and simulations (fills to zero). Here, B is 75° to the c-axis.

temperature (fig. 5.17b), at high power, we observe a saturation. When interpreting the low power range as linear, rhe linewidth can be written as

$$\Delta B^2 = \left(\frac{\hbar}{g_e \mu_B T_2^2}\right)^2 \left(1 + \frac{W}{W_0}\right) \tag{5.10}$$

with the characteristic rf power $W_0 \propto \frac{1}{T_1 T_2^*}$ and the incident rf power W. If one now assumes a very short spin-spin relaxation time T_2^*, the saturation rf power W_0 increases. The saturation behaviour of the curve, tentatively fitted with a logarithm, is nevertheless unaccounted for. Hence we have to assume eqn. 5.10 is incomplete concerning high rf power at high temperature. The introduction of a simple power dependence $T_2^*(W)$ into the spin-spin relaxation, as we expect lifetime shortening at high powers, was not successful. To quantify these results, more complex processes, like e.g. lifetime shortening through phonon coupling in an rf heated sample, have to be considered.

The two quantum transitions in fig. 5.17b,c are also not linearly dependent on the microwave power. As expected from [157], this second order process is more viable with higher microwave power. However, at these power levels, the two quantum ratio (i.e. the ratio with which the simulated two quantum spectra are superimposed on the one quantum spectra) also begins to saturate, which contradicts the superlinear power dependence behaviour expected for a second order process.

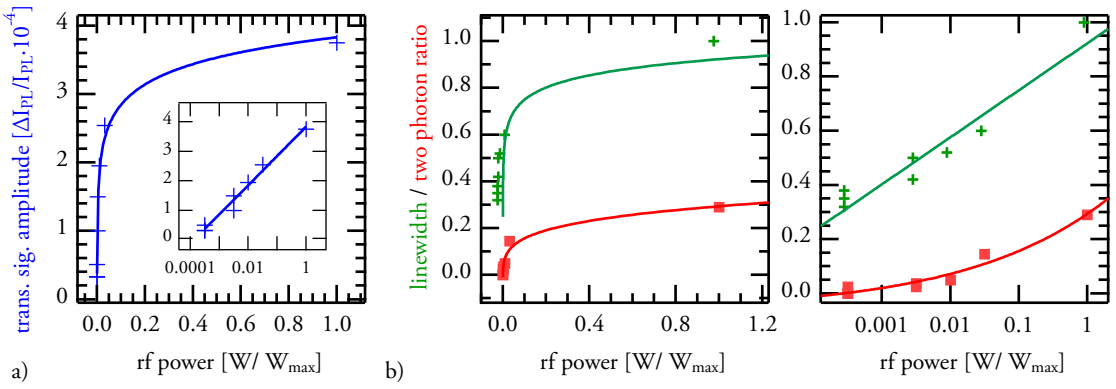

Figure 5.17.: RF power dependence of signal amplitudes, linewidth and two photon transition proportion at room temperature. a) is the principal + transitions signal height development at changing rf power, with the inset showing a log-lin representation. The solid line is a logarithmic fit, as are the green lines in b) and c), which are fitted to the overall linewidth ratios. The linewidths are extracted from the simulations shown in fig. 5.16, and are normalized to the linewidth at highest microwave power. The two photon transition ratios in red are also extracted from simulation.

5.6.5. Excitation schematic of the silicon vacancy

In the last chapters, it has been established that for the V2 and the V3 defect in 6H-SiC, there is a at least three level excitation system, where the ground state shows emission and absorption for different spin substates. We have also shown that these processes are still viable at ambient temperature. From the information gathered we can now propose an excitation schematic, shown in fig. 5.18.

The silicon vacancy is excited by a pumping laser into the upper phonon sideband, and can then recombine radiatively from the lower phonon sideband, emitting a red shifted photoluminescence. The other possibility is a spin selective recombination via one or more metastable shelving states. The excitation transitions into the shelving state, from where it preferably populates the $m_S = \pm 3/2$ manifold. This manifold also conveniently lies energetically higher, fulfilling the requirements for a population inversion. In analogy with a LASER, this is the prerequisite to construct a solid state MASER system using the intriguing spin pumping cycle of SiC silicon vacancies [168].

5.6.6. MASER Gain

With the samples and facilities as they were at transcription of this document, the feasibility of a SiC V_{Si} MASER could be proven. To create a working prototype, several parameters have to be understood and improved. For the ambition of a low noise, high amplification solid state MASER, great emphasis is on the terms *noise and gain*.

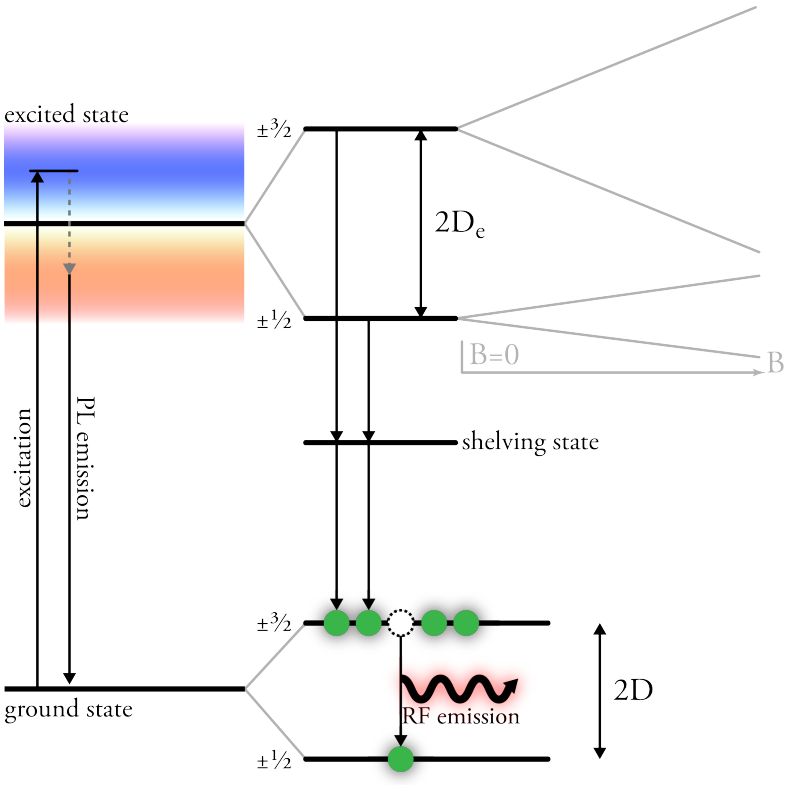

Figure 5.18.: SiC silicon vacancy excitation schematic. Excitation of the V_{Si} into the phonon assisted absorption (see ch. 5.3.3), and subsequent phonon assisted emission . The excited state is axially zero-field split with a D_{exc} into the $\pm 3/2$ and $\pm 1/2$ manifolds, which can be Zeeman-split by an external magnetic field (gray). The same goes for the zero-field split ground state. The excitation can cross into a metastable shelving state, thence it intersystem-crosses selectively into the $\pm 3/2$ manifold. The overcharged manifold can then relax into the lower lying $\pm 1/2$ manifold, under emission of microwaves with the energy $2D$..

A MASER system which is very similar to the SiC system is the paramagnetic amplifier in ruby crystals [169]. The same approach is now adapted to the parameters of SiC [170].

The gain of such an amplifier is described by

$$G = \left(\frac{2 d_m}{1 + d_m \frac{\nu}{\Delta\nu}} Q + 1 \right)^2 \tag{5.11}$$

with the transition linewidth $\Delta\nu$ at a center frequency $\nu = 9.434\text{GHz}$. d_m is the interaction between the crystal and the rf field inside the resonance cavity, which has a quality factor $Q = 3000$. This interaction is also denoted as the negative magnetic decrement, and is as follows:

$$d_m = 4\pi |\chi''| \eta \tag{5.12}$$

Here, η is the resonator filling factor, which we approximate with $\eta = 3\times10^{-4}$. The imaginary part of the magnetic susceptibility χ'', which identifies the stimulated emission of microwaves, causes an exponential increase of microwave radiation:

$$\chi'' \approx 10^{-13}\rho N_{V\mathrm{Si}}\frac{\sigma^2}{\Delta\nu} \tag{5.13}$$

The V_{Si} concentration is $N_{V_{Si}} = 10^{15}\mathrm{cm}^{-3}$ and the transition matrix element for stimulated quantum transitions is $\sigma^2 = \frac{1}{2}$ for a first order spin transition $\Delta m_S = \pm1$ [170]. For $V_{Si}(V2)$ at low temperatures, $\Delta\nu_{V_{Si}(V2),T=5K} \approx 5\,\mathrm{MHz}$, and therefore $G = 1.00036$. This is already a very small amplification factor, which will be eventually be compensated by losses in the resonator. At room temperature ($\Delta\nu_{V_{Si}(V2),T=300K} \approx 30\,\mathrm{MHz}$), the amplification drops to $G = 1.00006$. However, this holds only for the nonspecialized samples used previously. Possible room for improvement is the defect density, which can be brought up to $N_{V\mathrm{Si}} = 10^{18}\,\mathrm{cm}^{-3}$, which already increases G to 1.06. The very small sample in comparison to the large X-Band cavity is also an angle for increasing G. With a fill factor η nearing unity, the gain reaches nearly 300 ($G_{\mathrm{dB}} = 25\mathrm{dB}$). This can be further increased to $G_{\mathrm{dB}} = 100\mathrm{dB}$ using a travelling-wave amplifier approach [115].

As aforementioned, the noise figures of a high frequency amplifier system plays a crucial role in assessing its applicability. A common method to describe a system's noise, especially for communications, is the noise temperature. There, the frequency dependent power distribution of the noise, the spectral power density, is expressed as a temperature

$$T_{\mathrm{noise}} = \frac{1}{k_B}\frac{\mathrm{Power}}{\mathrm{Bandwidth}} \tag{5.14}$$

To set the stage: The noise temperature of a typical electronic low noise amplifier is $298K$. The present gold standard for communications, the ruby MASER, possesses noise temperatures around $13K$ [171], and cryogenic MESFETs can reach noise temperatures below $10K$ [172]. However, both of these systems operate at a liquid helium temperature. This weakness pertains all conventional maser systems [173], until the recent advent of quantum amplifier approaches with silicon carbide and, with similar advantages, organic crystals [174].

The noise in the silicon vacancy quantum amplifier is mainly caused by spontaneous emission, and can therefore be described by

$$T_{\mathrm{noise}} = \frac{1}{k_B}h\nu \approx 0.4K \text{ at } \nu = 9\,\mathrm{GHz} \tag{5.15}$$

This very low intrinsic value accumulates with the resonator's noise, which is depending on the ambient temperature. However, if the number of microwave amplifying centers is larger than the number of thermally excited microwave photons, it is expected to be much smaller than ambient temperature.

5.7. The $V_{Si} - Si_i$ Frenkel pair, the unassigned defect UD, and defects in 4H-SiC

In the last chapters, mainly the 6H silicon vacancies V2 and V3 were discussed. As already mentioned in ch. 5.6.1, there are two more microwave active quantum defect types addressable by near infrared excitation: The $V_{Si} - Si_i$ vacancy-interstitial Frenkel pair, and an unassigned defect (UD). In general, these defects are not so different from the already discussed silicon vacancies, but they boast some intriguing properties concerning their environmental parameters. In this chapter, the defects themselves will be briefly introduced. Furthermore, the previous chapters concerned themselves mainly with the 6H polytype of silicon carbide. However, there are a lot of common features of 6H and the 4H polytype. Here, 4H-SiC defects will be briefly introduced analogously to the chapters pertaining 6H-SiC. Application of the Frenkel pair and of the UD in magnetometry and temperature sensing will then be discussed in the following chapters.

5.7.1. The unassigned defect (UD)

Similar to the silicon vacancies' spin multiplicity, the literature is discordant about the nature of the defects with parameters similar to these shown in fig. 5.19. Overhof et al. connects the so-called P6/P7 defects with a carbon antisite-carbon vacancy ($C_{Si} - V_C$) combination, wherein the involved high-spin state is an excited triplet. The zero field splittings ($2D > 2000$MHz) they calculate for these defects far outstrip the ZFS measured in this work [175]. On the contrary, Baranov et al. later claim, for the same defect class, a neutral $V_{Si} - V_C$ divacancy [176]. They corroborate their model with excluding an excited triplet by proving a high-spin ground state in low temperature EPR in absolute darkness [177]. Baranov measures a zero field splitting of $2D_{V_{Si}-V_C} = 1288$MHz at low temperatures. The room temperature measurement in this work deviates from this value by almost 20% ($2D_{UD,T=300K} = 1002$MHz). However, at low temperature, the deviation is much less: $2D_{UD,T=10K} = 1188$MHz. An easy approach would now be to surmise that UD identifies with the divacancy. But although the crystal field values match best to the values for P6/P7, we will later prove a quartet ground state for UD, similar to the V_{Si}. Therefore, assuming a neutral

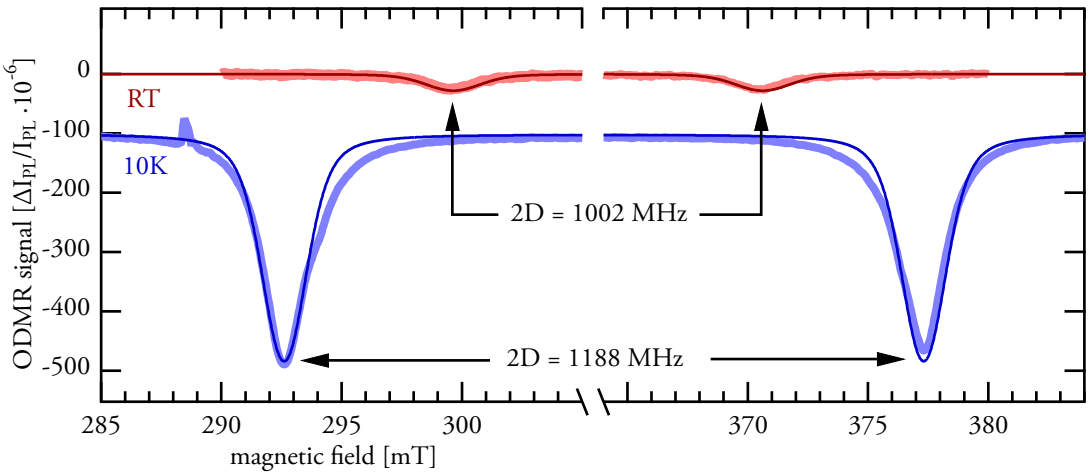

Figure 5.19.: A closer look at the ODMR of the unassigned defect in 6H-SiC at room temperature and 10K, both with phonon assisted excitation at $E_{exc} = 1.57$eV. The room temperature measurement is the same as in fig. 5.12. The thick curves are the measurements, the thin simulations. There is no data on the expected half field positions. $B \parallel c$ — axis.

divacancy for the UD state is not yet possible, and will need classic or pulsed EPR studies, preferably at double resonance conditions (ch. 5.5.1), to further clarify the issue.

Additionally, the linewidth of the UD is much larger than the V2 or V3 linewidths. This is attributed to a strong sensitivity to the local environment, which is emphasized by the strong spectral difference between room and low temperature which was not observed for the V_{Si} defects. This compelling property will be investigated closely in the following chapter.

5.7.2. The Frenkel pair

To classify the defect shown in fig. 5.20, we compare the defect's parameters to [143]. Von Bardeleben and his coworkers assign a Frenkel pair of a silicon interstitial, together with a silicon vacancy ($V_{Si} - Si_i$). The spin multiplicity is $S = \frac{3}{2}$, and they observe $2D = 412MHz$ at room temperature, which is close to the 358MHz measured here. The discrepancy, like for the unknown defect, can be explained by the strong influence of excitation power and temperature on these large ZFS defects. Therefore this signature is tentatively attributed to the $V_{Si} - Si_i$ Frenkel pair (see fig. 5.28).

5.7.3. Spin multiplicity of UD and Frenkel pair

Unlike for the V_{Si} vacancies, a quick look at the overview spectrum (fig. 5.12) and the zoom in fig. 5.19 and fig. 5.20 shows that straightforward evidence proving $S = 3/2$ is unfortunately absent here. Neither two quantum transitions (ch. 5.5.4), nor half field transitions

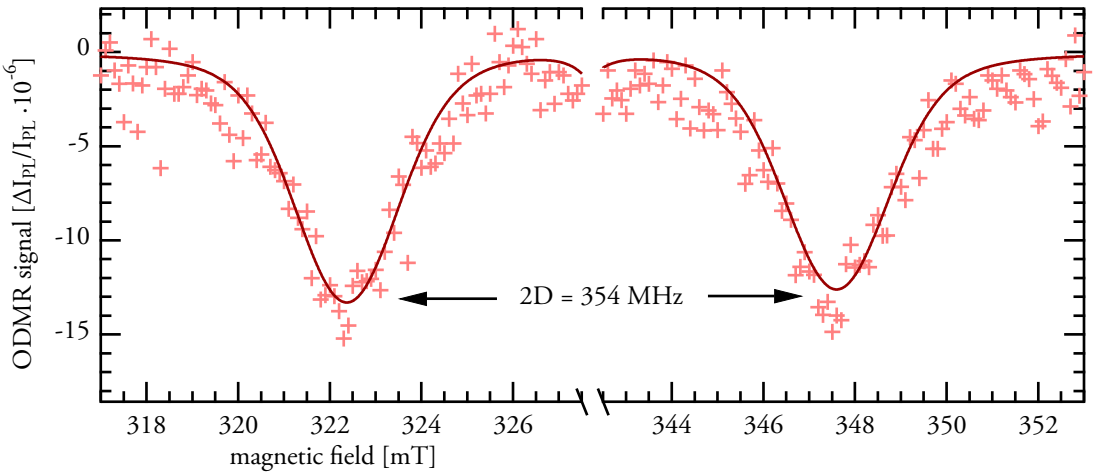

Figure 5.20.: ODMR of the Frenkel pair at room temperature. The measurement is the same as in fig. 5.12. The cross markers are the ODMR measurement, the thin line is a simulation with $2D = 358$MHz. There is no data on the expected half field positions. $B \parallel c$ — axis.

(ch. 5.5.5) could be isolated. To ascertain the spin state, we have to rely on the low magnetic field behaviour of the defects' ODMR. Low field ODMR has been measured (fig. 5.21) and the evolution of the signal from $B = 0$mT to $B = 2.2$mT is simulated in Fig. 5.22. The individual defect peak position evolution and the corresponding simulation clearly shows a behaviour which can only be explained with a quartet spin state, especially for the defects with higher zero field splitting like the UD and the $V_{Si} - Si_i$. For an axial zero field splitting, at low magnetic fields and with the B-field $\perp$ c-axis, for a $S = 1$ triplet no splitting is expected (fig. 5.22 - dotted lines). The $S = 3/2$ quartet however splits into two transitions right away, which is observed for all defects. Therefore, we can assume a quartet for all defects.

To explain the low field behaviour of especially V3, the hyperfine interaction with the ^{29}Si has to be taken into account. This was also done tentatively in fig. 5.22, considering the energy level splitting depicted in fig. 5.11. Some observed transitions can only be explained by the lower frequency transitions allowed by the hyperfine splitting. Here, we assume the same hyperfine interaction value $A = 8.5$MHz used in the low temperature EPR. The availably data only allows to do a rough estimate for this, however the software realized to obtain these simulations should simplify the interpretation of future measurements with this method.

5.7.4. Overview over the defects in 4H-SiC

The lattice stacking sequence of 4H-SiC allows for two distinguishable lattice position, resulting in two possible V_{Si} defects, one fewer than in 6H-SiC. Accordingly, we also observe one V_{Si} defect less. The V_{Si}(V2) defect in 4H, shown in fig. 5.24, has a zero field splitting of

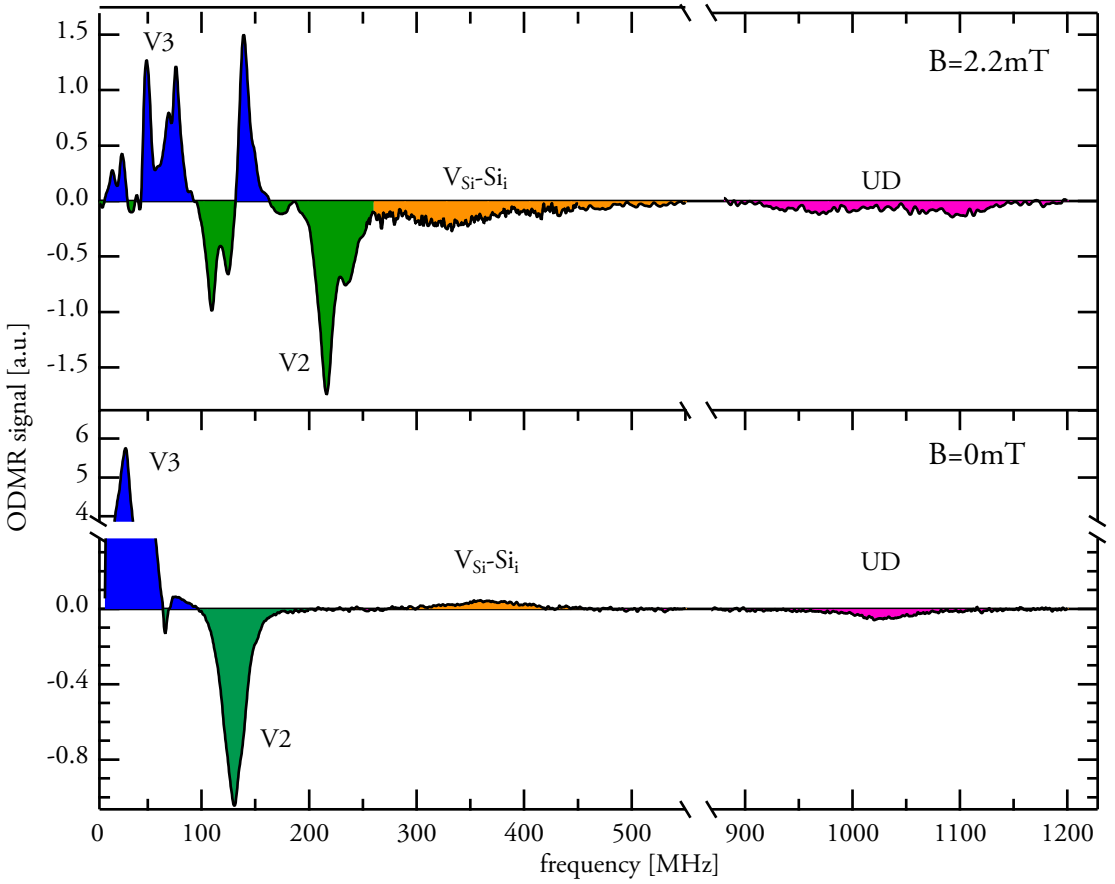

Figure 5.21.: Zero ($B = 0$mT, lower) and low field ($B = 2.2$mT, upper) ODMR of 6H-SiC at room temperature. These are two out of six spectra used do reconstruct the plots shown in 5.22.

$2D = 67.1$ MHz at room temperature, with linewidths of $\Delta\nu_g = 8.4$ MHz, $\Delta\nu_l = 16.8$ MHz. For this defect, we can also ascertain the quartet ground state, with the two photon transitions and also a half field transition, however the latter is difficult to detect.

The defect with larger zero field splitting $2D = 407$ MHz is linked to a Frenkel defect with silicon interstitial and V_{Si}, analogously to ch. 5.7.2. Like the V_{Si}—Si_i defect in 6H, this defect also expresses a large linewidth, of $\Delta\nu_g = 64.5$ MHz, $\Delta\nu_l = 25.2$ MHz.

5.8. A SiC quantum center temperature sensor

A significant temperature dependence of the zero field splitting D of the higher field Frenkel defect and the unidentified defect in 6H was already mentioned in the last chapter. A temperature dependence of D between 280K and 310K has already been observed in diamond

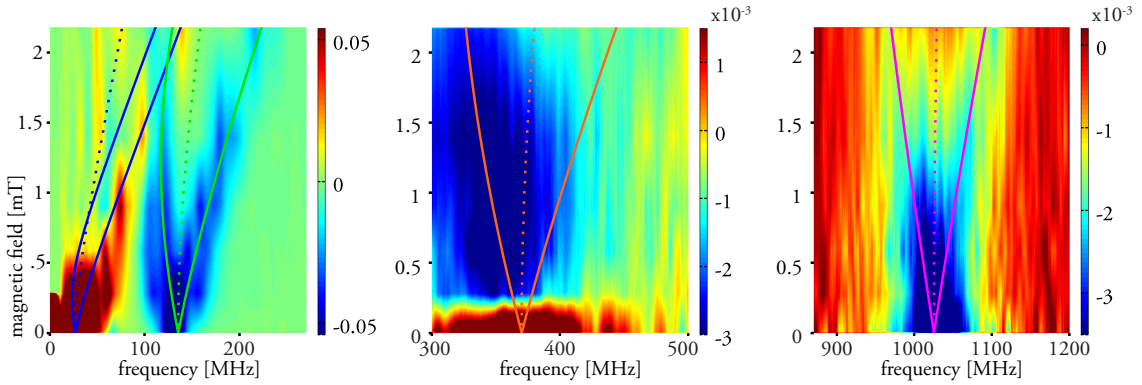

(a) V3 and V2 (b) Frenkel pair (c) UD

Figure 5.22.: Zero to low magnetic field ODMR curve evolution of 6H-SiC. The color code represents the ODMR amplitude [a.u.]. The solid lines show simulations of the $S = 3/2$ transitions without hyperfine interactions. The dotted lines are simulations of the corresponding $S = 1$ transitions. The surface plot was reconstructed from discrete ODMR frequency sweeps at 6 different magnetic fields $\perp$ c-axis.

NV centers [178]. The variation of $\frac{dD}{dT} = -75\frac{kHz}{K}$ [179] is there explained by thermal lattice expansion, although the authors also mention that the experimental value transcends the calculated value by a factor of 4.5.

For 6H-SiC, a temperature dependent full field ODMR curve batch was recorded between $T = 10K$ and $T = 310K$. The position of the ODMR resonance fields was simulated, and the temperature dependence of D was described by a third order polynomial:

$$2D(T) = 2D_{10K} + a_1 T + a_2 T^2 + a_3 T^3 \tag{5.16}$$

For the V2 and V3 defects, the temperature dependence was in the order of the experiments' resolution. For the $V_{Si} - Si_i$ Frenkel defect and the unidentified defect, however, a significant change is observed (table 5.1).

	V3	V2	$V_{Si} - Si_i$	UD
$2D_{0K}$[MHz]	27	124	662	1180
a_1[MHz/K]	0	0	-1.7	0.24
a_2[MHz/K^2]	0	0	2.3×10^{-3}	-5.2×10^{-3}
a_3[MHz/K^3]	0	0	-8×10^{-7}	6.9×10^{-6}

Table 5.1.: Low temperature ZFS parameter 2D and polynomial coefficients to describe the temperature evolution of the 6H ODMR resonances.

From these values, a thermal shift for the silicon interstitial of $\beta_{V_{Si}-Si_i} = -530\frac{kHz}{K}$ is calculated, which is already almost 7 times as large as for the diamond NV defect. The shift

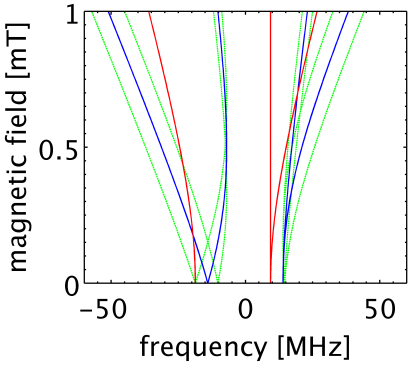

Figure 5.23.: The energy level splitting of the 6H V3 defects under low external magnetic field. Here, the red lines are the triplet energy substates, the blue lines are the quartet states, and the green lines are the quartet states, in turn split by the hyperfine interaction with the ^{29}Si's $I = 1/2$ nuclei.

of the UD is even larger, amounting to $\beta_{\mathrm{UD}} = -1017\frac{\mathrm{kHz}}{\mathrm{K}}$. For realization of a temperature sensor, we want the D to be as large as possible, and also its thermal shift, to obtain a maximum of resolution. Therefore, the UD is the most appropriate candidate for this application. However, the nature of this giant thermal shift is not clear, as will be discussed now.

5.8.1. Thermal shift of D and lattice expansion

If the zero field splitting is dipolar in nature, and has a negligible spin-orbit coupling, it can be used to derive an upper boundary for the distance of the participating charge carriers (see also 2.1.8).

For the UD, the defects' wavefunction extent approximation is, for 10K, $r_{10\mathrm{K}} = 0.494\mathrm{nm}$ and for 310K $r_{310\mathrm{K}} = 0.617\mathrm{nm}$. The variation between 10K and 310K is $\Delta D_{\mathrm{UD}} = 1.22\mathring{A}$, which amounts, simplified to a linear expansion module, to $\alpha = 1.54 \cdot 10^{-4}\frac{1}{K}$. This is two orders of magnitude larger than the literature values for the lattice expansion module of $(4.3 \ldots 4.7) \cdot 10^{-6}\frac{1}{K}$ [180]. Hence the simple explanation of the thermal shift by lattice expansion does also not hold for SiC.

For the interstitial silicon, the working hypothesis is that the interstitial is not rigid in the lattice; a small perturbation then leads to a large shift of position relative to the rigid V_{Si}. Another possibility would be a localized lattice distortion during the spin state transition, which could also be strongly temperature dependent. This has been observed in perovskite cobalt oxide crystals [181].

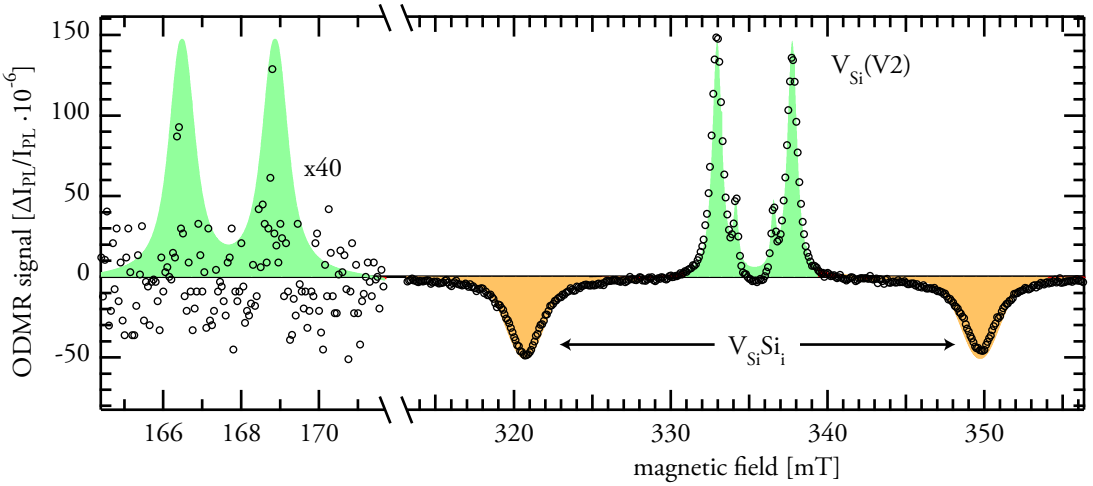

Figure 5.24.: Full field ODMR of 4H-SiC at room temperature. The circles denote the experimental spectrum, while the fills are the corresponding simulation, with parameters shown in 5.2. The half field data is expanded by a factor of 40.

5.9. SiC magnetometry

5.9.1. ODMR dependence on sample axis vector

In the last chapter, a large change of the zero field splitting parameters with temperature was observed for the $V_{Si} - Si_i$ and UD defects. It was also observed, that the V3 and V2 defects had no detectable temperature dependence. Although unsuitable for temperature sensing, one could utilize the robustness of these defects against ambient conditions to realize sensors for other observables. The zero field splitting D > 0, and the low field ODMR predictability shown in fig. 5.21, inspire the idea to use V3 and V2 as a magnetic field sensor. Compared to the already existing diamond NV magnetic field sensors, there is no rhombicity in the zero field interaction of SiC. In rhombic configurations, the low field behaviour in B || c-axis, which is crucial for magnetic field sensing, becomes nonlinear, as illustrated in fig. 5.26. This quadratic dependence of the relative resonance frequency limits the sensitivity at low magnetic fields. Another advantage is the relative shift of spin resonance positions depending on the magnetic field orientation. For NV spin triplet systems, this becomes zero at B $\perp$ c-axis. Therefore, in triplet systems only the projection of the field on the defect's sysmmetry axis can be detected. In pulsed experiments, the total field can be reconstructed from the spin-echo decay, because of the presence of hyperfine interactions with ^{13}C [182]. In $S = \frac{3}{2}$ systems on the other hand, the absolute value can be directly detected in cw measurements, without any reconstruction.

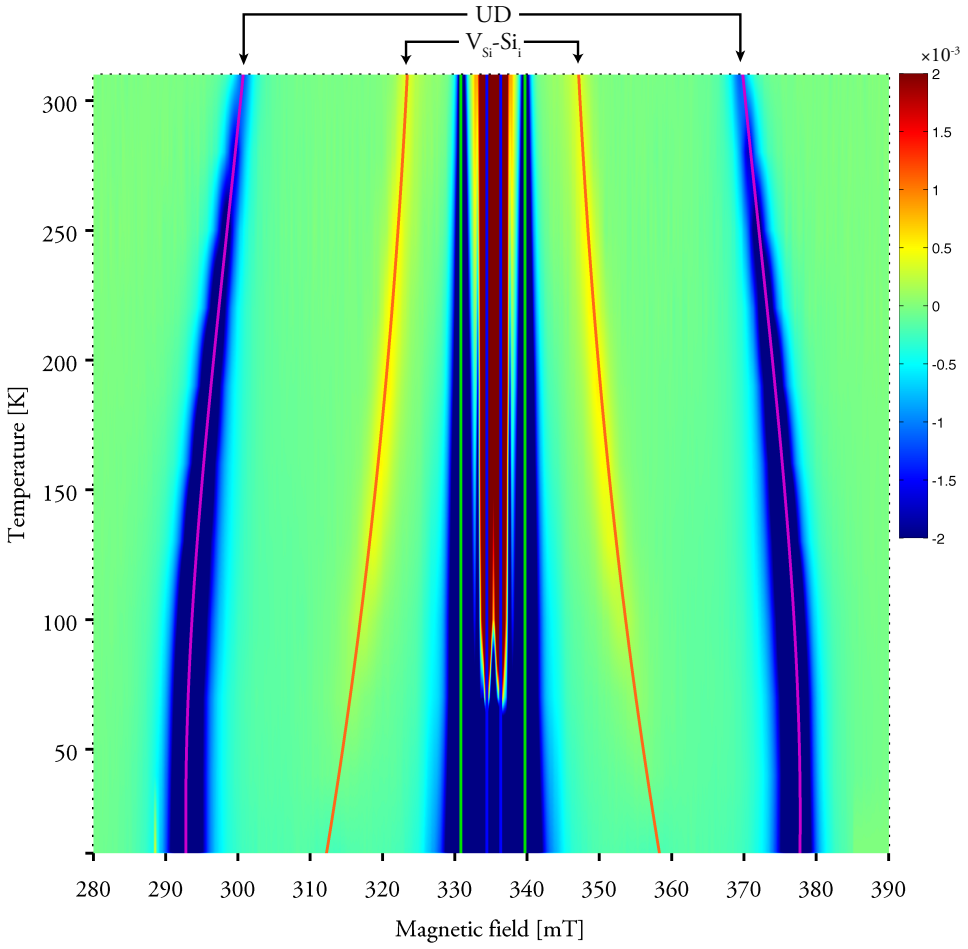

Figure 5.25.: Temperature dependence of the full field ODMR of 6H-SiC. The solid lines are the simulated resonance positions, with the zero field splitting calculated with a third order polynomial with the coefficients in table 5.1. In the center blue and green lines denote the simulations of the temperature independent V3 and V2 defect. The surface plot consists of curves from 10K to 310K in steps of 30K plus a measurement at 300K, denoised by averaging in both dimensions, with the color describing the ODMR signal amplitude $\frac{\Delta I_{\mathrm{PL}}}{I_{\mathrm{PL}}}$.

To properly position a SiC magnetometry sensor, it is neccessary to find the symmetry and spatial configuration of the defects. As the resonance positions of the $\pm$ transitions ($|3/2, \pm 3/2\rangle \rightarrow |3/2, \pm 1/2\rangle$) are depending on

$$\Delta B_{\pm} = B_{+} - B_{-} = \frac{2D}{g\,\mu_B}\left(3\cos^2\vartheta - 1\right) \tag{5.17}$$

with ϑ describing the angle between magnetic field and c-axis. This equation holds for all defects observed in 6H (ref. [26] fig. 3) and 4H (fig. 5.27), which corroborates that all defects are axial in nature, and are oriented in line along the crystal c-axis.

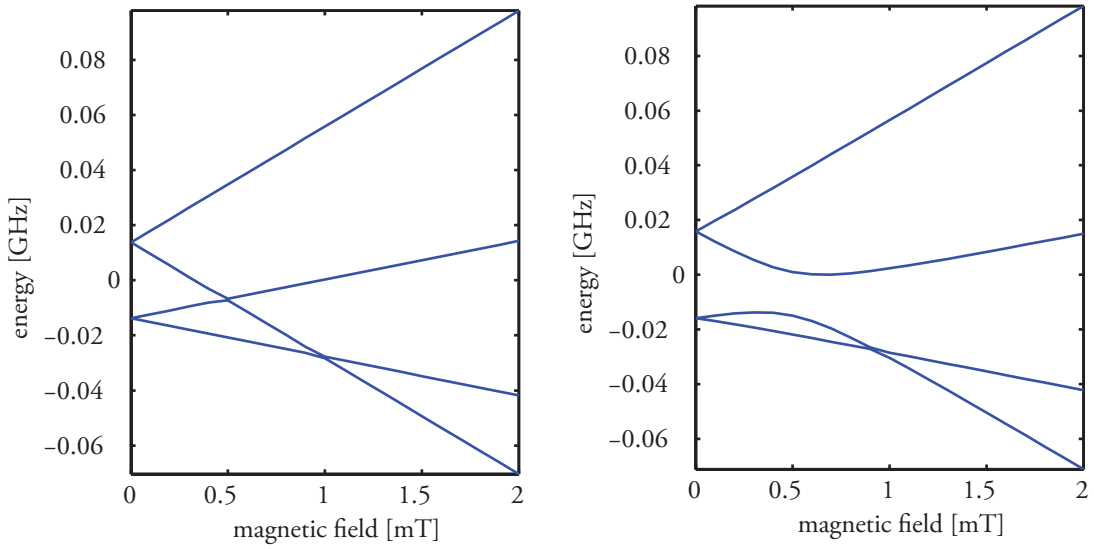

(a) $D \neq 0, E = 0$ (b) $D \neq 0, E = \frac{D}{3}$

Figure 5.26.: Low field behaviour of axial vs. rhombic ZFS spin defects. Simulation of magnetic field || c-axis.

5.9.2. Distortion due to neighboring V_c induces the zero field splitting

An isolated V_{Si}^{-} should have a T_d symmetry, like the V^- in diamond NV centers, and thus should have a vanishing zero field splitting [183, 154]. As a zero field splitting is observed in the V2 and V3 defects in 6H-SiC, and in the V2 in 4H-SiC, a distortion in the vicinity of the defect has to be considered [153]. In the last chapter, we have ascertained the defects axial orientation along the c-axis. Hence, the distortion source is also assumed to be along the c-axis.

We suggest a next neighbor carbon vacancy for 6H-SiC V2 and V3, as shown in 5.28. This also could explain why the V1 defect cannot be observed in ODMR, neither in 4H- nor in 6H-SiC. If V1 is not subject to the aforementioned distortion, the degeneracy of the $m_S = \pm 3/2$ and $m_S = \pm 1/2$ manifolds would lead to just one transition line at $g \approx 2$, which, if observable at all, then overlaps with the $|3/2, -1/2\rangle \leftrightarrow |3/2, +1/2\rangle$ transition lines of the other defects.

If we apply the wavefunction extent calculations from ch. 5.8.1 to the zero field splittings of the V3 defect of 6H, we obtain $r_{V3,ODMR} = 14.2\mathring{A}$. The corresponding calculated lattice distance between the V_{Si} and the V_C (fig. 5.28) is, for V3, $r_{V3 \leftrightarrow V_C} = 8.22\mathring{A}$.

For V2, the ODMR estimated distance is $r_{V2,ODMR} = 8.5\mathring{A}$ and the lattice distance between V2 and the next neighbor V_C is $r_{V2 \leftrightarrow V_C} = 3.16\mathring{A}$. Considering that the calculation in eqn. 2.15 describes an upper bound, we can at least perceive the right trend of increasing ZFS for

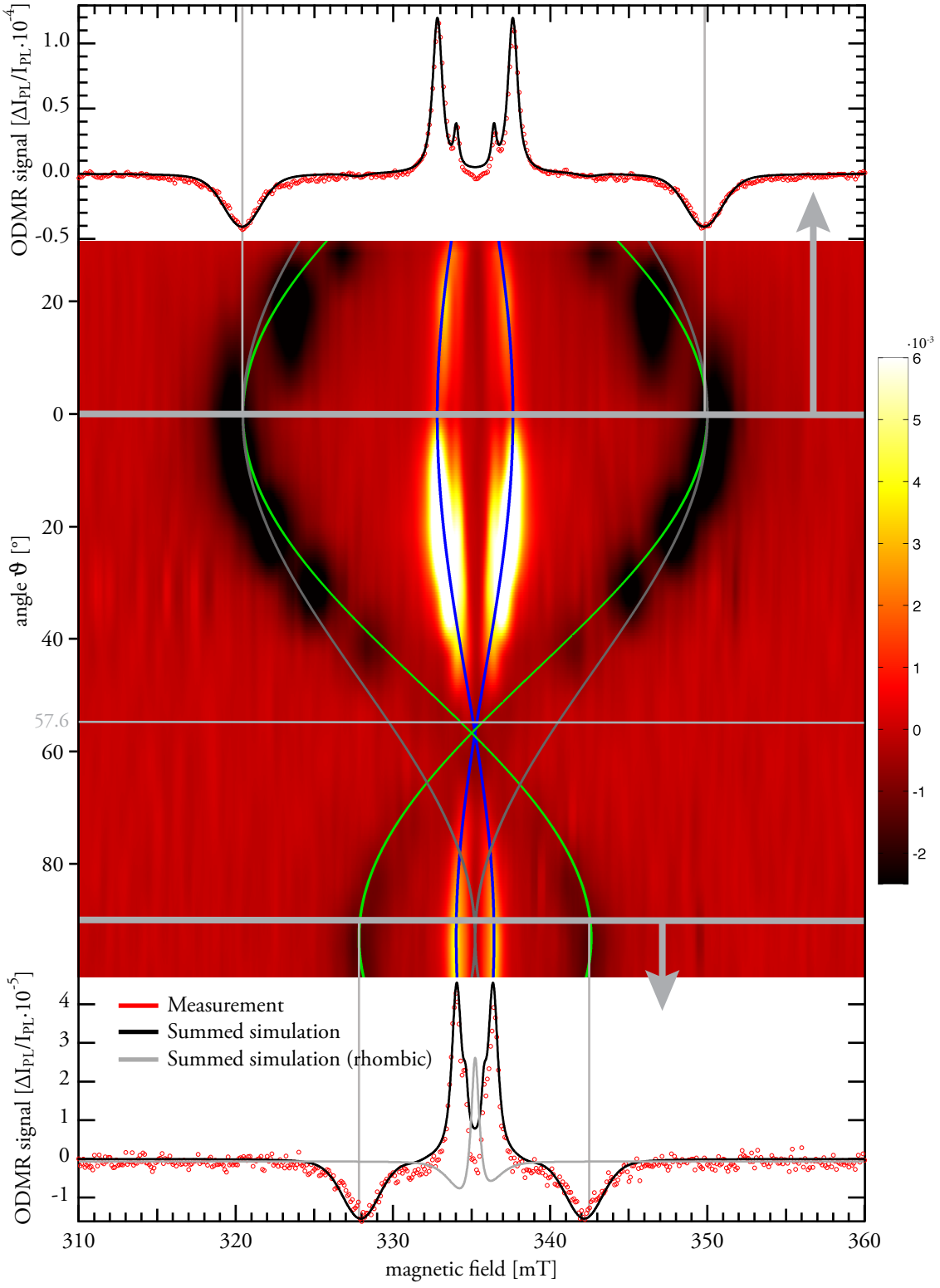

Figure 5.27.: Dependence of 4H-SiC's ODMR on the angle beetween c-axis and external magnetic field. 0° means B || c-axis. The solid lines in the surface plot are simulations with the parameters in 5.2, with the crystal orientation shifted to the corresponding sample rotation angle. The spectra at the top and bottom are horizontal slices at 0° and 90°, respectively, with small circles depiciting the measurement and the black solid line the simulation. To elucidate why a rhombicity can be excluded ($E = 0$), an exemplary rhombic spectrum for the Frenkel pair is plotted in grey.

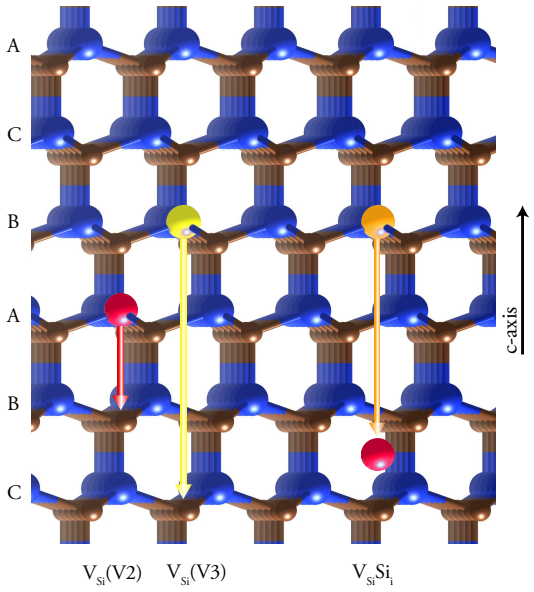

Figure 5.28.: Lattice of 6H-SiC with defects (colored circles). The silicon is depicted in blue, the carbon in copper. The arrows depict, for the V_{Si}, the carbon lattice position responsible for the distortion of the defect; and for the Frenkel pair, the silicon interstitial.

distortions of closer lying V_C. It also implies that both $V_{Si}-Si_i$ and UD with their large ZFS should be located in one unit cell of the SiC crystal.

5.10. Silicon carbide – Summary

In this chapter, silicon carbide was introduced as a potential candidate material for quantum applications. The NIR emitting silicon vacancies V2 and V3 in 6H-SiC, and V2 in 4H, in addition to a vacancy-interstitial Frenkel pair and an unassigned defect UD, were all proven to be optically accessible and to carry a $\frac{3}{2}$ spin. The zero field interaction and hyperfine interaction parameters were ascertained. The ODMR of these defects was shown to also work at room temperature, which is an important prerequisite for upscaling a system for quantum computing. An EPR signal inversion was observed in 6H-SiC, prompting the creation of an excitation schematic that allows for a low noise microwave amplification (MASER) effect at room temperature. The calculated MASER gain in the present state is modest, but opportunities for increasing it to G=300 were demonstrated.

The silicon interstitial and the UD were scrutinized in detail; they express an intriguing giant temperature dependence of the zero field splitting D. Finally, the prerequisites for magnetometry were set by finding out the symmetry axes of the defects, proposing a distortion of the silicon vacancies by carbon vacancies situated in c-axis direction.

Defect	Experiment	$2D$	$\Delta\nu_g$	$\Delta\nu_l$	HFI	I_{2q}/I
		6H-SiC				
$V_{Si}^{-}(V2)$	EPR 4K	127.5	2.2	1.4	7.8	
	ODMR 4K	127.5	22.4	16.2		0.63
	ODMR 300K	128.0	11.2	19.6		0.2
$V_{Si}^{-}(V3)$	EPR 4K	27.3	3.9	0	8.5	
	ODMR 300K	27.0	6.7	16.8		0.29
$V_{Si}^{-}(V_{Si}Si_i)$	ODMR 300K	358	61.7	28		0.3
UD	ODMR 300K	1002	61.7	28		
UD	ODMR 10K	1188	47.6	25.2		
		4H-SiC				
$V_{Si}^{-}(V2)$	ODMR 300K	67.1	8.4	16.7	8.1	0.25
$V_{Si}^{-}(V_{Si}Si_i)$	ODMR 300K	408	64.4	25.2	9.1	

Table 5.2.: Parameters for all shown EPR and ODMR simulations of SiC. The parameters are sorted by material and defect types, and are as follows: the zero field splitting $2D$ [MHz], denoting only the D parameter of the $\boldsymbol{D}$ tensor, with $E = 0$ for all results. $\Delta\nu_g$ [MHz] is the gaussian linewidth, $\Delta\nu_l$ [MHz] the lorentzian, respectively. The HFI [MHz] is the isotope hyperfine interaction frequency $\frac{A}{h}$, assuming an isotropic hyperfine interaction in all cases. Finally, I_{2q}/I is the intensity ratio of two quantum transitions to the principal transitions, where applicable.

6. Summary

In this work, we moved through three different material systems comprising carbon: (i) Organic polymers and small molecules, in conjunction with fullerene molecules for applications in organic photovoltaics (OPV), (ii) single walled semiconducting carbon nanotubes and (iii) silicon carbide (SiC), whose defect color centers are recently in the limelight as candidates for quantum applications.

In the OPV world, the energy level alignment between polymer donors, like the molecules P3HT or PTB7, and fullerene acceptors like $PC_{60/70}BM$, is of crucial interest. It is the driving force for charge separation after excitation, and subsequent charge transport; culminating in a photocurrent – the prerequisite of a working solar cell. The first part of the OPV chapter focuses on using optically detected magnetic resonance (ODMR) to find out the quantity, multiplicity and intrinsic interaction parameters of optically active spin species, as well as their orientation in semiconducting organic materials. The issue of semi-ordered systems in the conjugated polymers P3HT and PTB7, and in the small molecule DIP was discussed, finding an edge-on configuration for DIP and P3HT, and a face-on configuration for PTB7. The information about ordering allowed to deconvolve the pseudo-powder spectra, yielding precise values for the zero field interaction parameters D and E. In both P3HT and PTB7, simulation of one localized and one long interaction range triplet can fully explain the experimental results, while the DIP necessitates the addition of one more localized triplet.

The second part of the OPV chapter is occupied with understanding the mechanisms which allow attaining a high solar cell open circuit voltage through minimizing the donor-acceptor LUMO-LUMO gap, without losing charges due to recombination. A likely candidate for recombination losses in low LUMO-LUMO gap systems is the electron back transfer (EBT) from the acceptor to the donor's triplet state after excitation and charge transfer. Using ODMR, we compared the solar cell blends' triplet yields of the high-efficiency benzodithiophene PTB7 to the lower-efficiency OPV workhorse P3HT. Although the PTB7:$PC_{70}BM$ blends have a much higher solar cell power conversion efficiency, it also shows a significant increase in triplet exciton yield. The P3HT:$PC_{60}BM$, with a much larger LUMO-LUMO gap, shows no triplet generation at all. Additionally, when increasing the donor-acceptor interface/bulk ratio by adding Diiodooctane (DIO) to the PTB7 blend, the triplet yield increases even further. In conjunction with luminescence quenching behaviour and atomic force

microscopy results, an increased triplet yield when increasing interface area, and hence, opportunities for charge transfer strongly indicates an electron back transfer as the triplet generation mechanism.

The second research focus ventured into the still underexplored field of high spin exciton dynamics in single walled carbon nanotubes. Despite their auspicious role in photovoltaics and photoelectronics, little is known about the nanotubes' triplet excitons. This may be due to the fact, that optical spectroscopy on nanotubes is, because of their low luminescence yield, very challenging. We managed to detect, for the first time, the triplet exciton in (6,5) SWNT using ODMR; and found out the lifetime of the triplet to be in the 30μs range. The reduced dimensionality of the large aspect ratio nanotubes in a thin sample helped to ascertain the zero field interaction parameters of the triplet excitons. Time resolved PL spectroscopy, carried out by the group of Prof. Tobias Hertel, showed a very long-lived background fluorescence signal. This delayed fluorescence is ascribed to annihilating triplets, leading to an excited singlet in $\frac{1}{9}$ of all annihilations events.

The last part of this work devotes itself to spin centers in silicon carbide. These centers are usually limiting the performance of high-power applications of SiC material, and are rather unwanted. However recently, due to the easy initialization and readout even at ambient conditions, spin carrying defects (e.g. silicon vacancies) in SiC are traded as a possible augmentation of diamond NV defects as qubits for quantum computing and other applications. One important open question, that has a large impact on the spin coherence time, and also on the sensitivity to the crystalline environment, is whether the spin multiplicity of the center's ground state is an S=1 triplet, or an S=3/2 quartet. ODMR could answer this question unambiguously: The existence of both two half field transitions and two two-quantum transitions clearly state an S=3/2 quartet, for the silicon vacancy (V_{Si}) and also for defects in 6H-SiC which are ascribed to a Frenkel defect ($V_{Si}-Si_i$) and an yet unassigned defect UD. We discovered a unique spin polarized pumping of the ground state; this optically pumped population inversion leads to the stimulated emission of microwaves.

When taking a closer look at the Frenkel and UD defects, a very strong temperature dependence of the center's zero field splitting is obvious, which is, in the Frenkel defect case, due to the mobility of the interstitial silicon in the crystal lattice. This, together with the V_{Si} centers being sensitive to the vector and strength of the external magnetic field, ushered us to investigate the prospects of SiC as a quantum temperature and magnetometry sensor. To continue on this, the knowledge gained about full field EPR and ODMR, especially about microwave technology, was devoted to the construction of a spatially-resolved zero/low field ODMR spectrometer, with the capability to three-dimensionally control the magnetic field up to 30mT. First measurements, together with sample angle dependent full field ODMR, show

that the V_{Si} centers, which are independent of temperature fluctuations and crystal strain, could be used as precise vector magnetometers.

Zusammenfassung

In der hier vorgelegten Arbeit wurden drei verschiedene Kohlenstoffallotrope bearbeitet: (i) Organische Polymere zusammen mit Fullerenmolekülen für Anwendung in der organischen Photovoltaik (OPV). (ii) Einwandige Kohlenstoffnanoröhren sowie (iii) Siliziumkarbid, dessen optisch aktive Defekte derzeit als heißer Kandidat für Anwendungen in Quantentechnologien gehandelt werden.

In der OPV, die Anpassung des Energieabstands von Polymerdonatoren wie dem Polythiophen P3HT oder dem Benzodithiophen PTB7, zu Fullerenakzeptoren wie $PC_{60/70}BM$, ist als treibende Kraft für die Ladungstrennung nach Anregung elementar wichtig. Diese, und der durch sie entstehende Photostrom, macht die funktionsfähige Solarzelle aus. Der erste Teil des OPV-Kapitels konzentriert sich darauf, Anzahl, Multiplizität und intrinsische Parameter der optisch aktiven spintragenden Zustände und organischen Donatoren mittels optisch detektierter Magnetresonanz herauszufinden. Dazu muss die teilweise Ordnung der betrachteten System diskutiert werden. Es wurden für P3HT und DIP eine stehende, und für PTB7 eine liegende molekulare Anordnung gefunden. Die Information über die Ordnung hat eine präzise Bestimmung der Nullfeldaufspaltung der Pseudopulverspektren ermöglicht. Sowohl für PTB7 als auch für P3HT, erklärt die Simulation mit einem lokalisierten und einem weit entfernten Triplet die experimentell gewonnenen Spektren vollständig. In DIP dagegen is ein weiteres lokalisiertes Triplet zur vollständigen Beschreibung notwendig.

Der zweite Teil des OPV-Kapitels beschäftigt sich mit dem Spannungsfeld zwischen optimaler Leerlaufspannung, erreicht durch Minimieren der Donator-Akzeptor LUMO-LUMO-Bandlücke, und Ladungsverlust durch Rekombination. Ein möglicher Kandidat für Rekombinationsverluste in Materialien mit geringem LUMO-LUMO-Abstand is der Elektronenrücktransfer vom Akzeptor in den Triplettzustand des Donators nach Ladungstrennung. Mittels ODMR wurde die Triplettproduktion von Heteroübergängen des effizienteren PTB7 mit der des traditionellen Arbeitspferds der OPV – P3HT – verglichen. Während die P3HT:$PC_{60}BM$-Mischung keinerlei Tripletts zeigt, sticht das PTB7:$PC_{70}BM$-Blend trotz seiner hohen Konversionseffizient mit einer deutlichen Triplettproduktion hervor. Diese wird unter Zugabe des Additivs Diiodooktan (DIO), welches das Verhältnis von Donor-Akzeptor-Grenzfläche zu Volumen erhöht, noch deutlich stärker. Diese Tatsache deutet, zusammen mit dem Verhalten des Materials bezüglich Photolumineszenz und Morphologie, stark auf einen Elektronenrücktransfer als Generationsmechanismus für Triplettexzitonen hin.

Der zweite Forschungsbereich dieser Arbeit bewegt sich im immer noch wenig erforschten Feld der Exzitondynamik hoher Spins in einwandigen halbleitenden Kohlenstoffnanoröhren. Trotz ihrer vielversprechenden Anwendungen in Photovoltaik und -elektronik ist über Triplettexzitonen in Nanoröhren noch wenig bekannt. Der Grund dafür ist möglicherweise, dass optische Spektroskopie an Nanoröhren, ob ihrer schwachen Photolumineszenz, extrem schwierig ist. Im Rahmen dieser Arbeit wurde zum ersten Mal das Triplettexziton in einwandigen Kohlenstoffnanoröhren nachgewiesen. Die Lebensdauer wurde zu 30μs bestimmt. Mittels der Ordnung in zwei statt drei Dimensionen in einer extrem dünnen Probe wurden die Parameter für die Nullfeldaufspaltung des Triplettexzitons herausgefunden. Zeitaufgelöste Photolumineszenzspektroskopie der Gruppe von Prof. Tobias Hertel zeigte einen sehr langlebiges Fluoreszenzhintergrund. Diese verzögerte Fluoreszenz wird ebenfalls einer Triplett-Triplett-Annihilation zugeschrieben.

Der letzte Teil der Arbeit widmet sich Spinzentren in Karborund (Siliziumkarbid - SiC). Üblicherweise werden diese Fehlstellen, zumindest in der Leistungselektronik – dem üblichen Einsatzgebiet von Siliziukarbid – als leistungsmindernd eingestuft und dementsprechend wenig geschätzt. Seit Kurzem werden spintragende Kristalldefekte in SiC (z.B. Siliziumfehlstellen) als mögliche Alternative zu NV-Defekten in Diamant für Qubits in Quantencomputing und anderen Quantenanwendungen gehandelt – nicht zuletzt wegen ihrer einfachen Initialisier- und Auslesbarkeit sogar bei normalen Umgebungsbedingungen. Eine wichtige, in der Literatur intensiv diskutierte Fragestellung, die einen großen Einfluss auf Spinkoheränzzeiten und auch auf Sensitivität gegenüber der Kristallumgebung hat, ist, welche Multiplizität diese Fehlstellen aufweisen. Diese Frage konnte mit ODMR zweifelsfrei zugunsten des $S = \frac{3}{2}$ Quartetts beantwortet werden, für alle Siliziumvakanzen in 4H-SiC und 6H-SiC und auch für Frenkel-Defekte mit interstiziellem Silizium und dem nicht zugeordneten Defekt UD. Die Existenz zweier Halbfeldübergänge und zweier Zweiphotonübergänge ist durch ein Spin-Triplett nicht zu erklären. Der Grundzustand ist aufgespalten in zwei Kramers-Dupletts, von welchem das Höherenergetische selektiv optisch gepumpt wird. Die dadurch verursachte Besetzungsinversion erzeugt eine stimulierte Emission, und ermöglicht den Einsatz von SiC-Spindefekten als MASER.

Nähere Betrachtung des Frenkel- und UD-Defekts zeigen eine starke Temperaturabhängigkeit der Nullfeldaufspaltung, die – im Falle des Frenkeldefekts – einer erhöhten Beweglichkeit des interstitiellen Siliziums im Kristallgitter zugeschrieben wird. Diese Abhängigkeit, zusammen mit der Abhängigkeit der Vakanzdefekte von Stärke und Richtung des Magnetfelds, eröffnet die Möglichkeit, SiC als Temperatursensor und Magnetometer einzusetzen. Um diesen Weg zu verfolgen, wurden die gewonnenen Kenntnisse um Vollfeld-ESR und -ODMR – speziell Mikrowellentechnik – genutzt, um ein raumaufgelöstes Nullfeld-ODMR-Spektrometer zu konstruieren. Erste Messungen, zusammen mit Vollfeld-

ODMR abhängig von Probenorientierung, zeigten, dass die Siliziumvakanz, welche zudem noch robust gegen sowohl Kristallverspannungen als auch Temperaturfluktuationen ist, als präzises Vektormagnetometer eingesetzt werden kann.

Bibliography

[1] *Sagan C. The Cosmic Connection: an extraterrestrial perspective*. Cambridge University Press, **1973**. ISBN 0521783038.

[2] *Abragam A. and Pryce M.H.L.* Theory of the Nuclear Hyperfine Structure of Paramagnetic Resonance Spectra in Crystals. *Proc. Royal Soc. A: Math. Phys. Eng. Sci*. **205** (1951), 135. doi:10.1098/rspa.1951.0022.

[3] *Sperlich A. Electron Paramagnetic Resonance Spectroscopy of Conjugated Polymers and Fullerenes for Organic Photovoltaics*. Ph.D. thesis, Julius Maximilian University of Würzburg, **2013**.

[4] *Zeeman P.* VII. Doublets and triplets in the spectrum produced by external magnetic forces. *London, Edinburgh, Dublin Philos. Mag. J. Sci*. **44** (1897), 55.

[5] *Gerlach W. and Stern O.* Der experimentelle Nachweis der Richtungsquantelung im Magnetfeld. *Zeitschrift für Physik* **9** (1922), 349. doi:10.1007/BF01326983.

[6] *Zavoisky E.* Paramagnetic relaxation of liquid solutions for perpendicular fields. *J. Phys. USSR* **9** (1945), 211.

[7] *Sinnecker S. and Neese F.* Spin–Spin Contributions to the Zero-Field Splitting Tensor in Organic Triplets, Carbenes and BiradicalsA Density Functional and Ab Initio Study. *J. Phys. Chem. A* **110** (2006), 12267. doi:10.1021/jp0643303.

[8] *El-Sayed M.A.* Multiple resonance techniques in the study of the magnetic, radiative and non-radiative properties of the triplet state. *Pure Appl. Chem*. **24** (1970), 475. doi:10.1351/pac197024030475.

[9] *Steinhoff H.J., Radzwill N., Thevis W., Lenz V., Brandenburg D., Antson A., Dodson G., and Wollmer A.* Determination of interspin distances between spin labels attached to insulin: comparison of electron paramagnetic resonance data with the X-ray structure. *Biophys. J.* **73** (1997), 3287. doi:10.1016/S0006-3495(97)78353-X.

[10] *Maryasov A.G., Bowman M.K., and Tsvetkov Y.D.* Dipole-dipole interactions of high-spin paramagnetic centers in disordered systems. *Appl. Magn. Reson*. **30** (2006), 683. doi:10.1007/BF03166227.

[11] *Riplinger C., Kao J., Rosen G., Kathirvelu V., Eaton G., Eaton S., Kutateladze A., and Neese F.* Interaction of Radical Pairs Through-Bond and Through-Space: Scope and Limitations of the Point– Dipole Approximation in Electron Paramagnetic Resonance Spectroscopy. *J. Am. Chem. Soc*. **131** (2009), 10092. doi:10.1021/ja901150j.

[12] *Swanson L., Lane P., Shinar J., and Wudl F.* Polarons and triplet polaronic excitons in poly(paraphenylenevinylene) (PPV) and substituted PPV: An optically detected magnetic resonance study. *Phys. Rev. B* **44** (1991), 10617. doi:10.1103/PhysRevB.44.10617.

[13] *Bucher M.* The electron inside the nucleus: an almost classical derivation of the isotropic hyperfine interaction. *Eur. J. Phys*. **21** (2000), 19. doi:10.1088/0143-0807/21/1/303.

[14] *Manson N., Harrison J., and Sellars M.* Nitrogen-vacancy center in diamond: Model of the electronic structure and associated dynamics. *Phys. Rev. B* **74** (2006), 104303. doi:10.1103/PhysRevB.74.104303.

[15] *Dyakonov V., Rösler G., Schwoerer M., and Frankevich E.L.* Evidence for triplet interchain polaron pairs and their transformations in polyphenylenevinylene. *Phys. Rev. B* **56** (1997), 3852. doi:10.1103/PhysRevB.56.3852.

[16] *Johnson R.C. and Merrifield R.E.* Effects of magnetic fields on the mutual annihilation of triplet excitons in anthracene crystals. *Phys. Rev. B* **1** (1970), 896. doi:10.1103/PhysRevB.1.896.

[17] *Suna A.* Kinematics of exciton-exciton annihilation in molecular crystals. *Phys. Rev. B* **1** (1970), 1716. doi:10.1103/PhysRevB.1.1716.

[18] *Hachani L., Benfredj A., Romdhane S., Mejatty M., Monge J., and Bouchriha H.* Fluorescence-detected magnetic resonance in organic systems: A pair-density matrix formalism approach. *Phys. Rev. B* **77** (2008), 035212. doi:10.1103/PhysRevB.77.035212.

[19] *Frankevich E.L., Lesin V.I., and Pristupa A.I.* Magnetic resonance of short-lived intermediate complexes in the reaction of quenching of triplet excitons by radicals. *Sov. J. Exp. Theor. Phys*. **48** (1978), 208.

[20] *Piris J., Dykstra T.E., Bakulin A.A., Loosdrecht P.H.M.v., Knulst W., Trinh M.T., Schins J.M., and Siebbeles L.D.A.* Photogeneration and Ultrafast Dynamics of Excitons and Charges in P3HT/PCBM Blends. *J. Phys. Chem. C* **113** (2009), 14500. doi:10.1021/jp904229q.

[21] *Stich D., Späth F., Kraus H., Sperlich A., Dyakonov V., and Hertel T.* Triplet–triplet exciton dynamics in single-walled carbon nanotubes. *Nat. Photonics* **8** (2013), 139. doi:10.1038/nphoton.2013.316.

[22] *McLauchlan K.A. and Steiner U.E.* Invited article: The spin-correlated radical pair as a reaction intermediate. *Mol. Phys*. **73** (1991), 241. doi:10.1080/00268979100101181.

[23] *Kraus H. Optisch detektierte Magnetresonanzspektroskopie an organischen Halbleitern*. Master's thesis, Julius Maximilian University of Würzburg, **2009**.

[24] *Stoll S. and Schweiger A.* EasySpin, a comprehensive software package for spectral simulation and analysis in EPR. *J. Magn. Reson*. **178** (2006), 42.

[25] *Gonen O. and Levanon H.* Line-shape analysis of transient triplet electron paramagnetic resonance spectra. Application to porphyrins and chlorophylls in nematic uniaxial liquid crystals. *J. Phys. Chem*. **88** (1984), 4223. doi:10.1021/j150663a007.

[26] *Kraus H., Soltamov V.A., Fuchs F, Simin D., Sperlich A., Baranov P.G., Astakhov G.V., and Dyakonov V.* Magnetic field and temperature sensing with atomic-scale spin defects in silicon carbide. *Sci. reports* **4** (2014). doi:10.1038/srep05303.

[27] *Simin D. Vektormagnetometrie mit Punktdefekten in Siliciumcarbid*. Master's thesis, Julius Maximilian University of Würzburg, **2014**.

[28] *Kraus H., Heiber M., Väth S., Kern J., Foertig A., Sperlich A., Deibel C., and Dyakonov V.* Triplet excitons in high-efficiency organic solar cell materials, in preparation, **2014**.

[29] *Sinn H.W.* Public policies against global warming: a supply side approach. *Int. Tax Public Finance* **15** (2008), 360. doi:10.1007/s10797-008-9082-z.

[30] *Brabec C.J., Sariciftci N.S., and Hummelen J.C.* Plastic solar cells. *Adv. Funct. Mater*. **11** (2001), 15.

[31] *Zervos H., Das R., and Ghaffarzadeh K.* Organic Photovoltaics (OPV) 2013-2023: Technologies, Markets, Players. Technical report, **2013**.

[32] NREL Best Research-Cell Efficiencies - Aug 2014. NREL, **2014**.

[33] *Sperlich A., Kraus H., Deibel C., Blok H., Schmidt J., and Dyakonov V.* Reversible and irreversible interactions of poly (3-hexylthiophene) with oxygen studied by spin-sensitive methods. *J. Phys. Chem. B* **115** (2011), 13513. doi:10.1021/jp2077215.

[34] *Su W.P., Schrieffer J.R., and Heeger A.J.* Soliton excitations in polyacetylene. *Phys. Rev. B* **22** (1980), 2099. doi:10.1103/PhysRevB.22.2099.

[35] *Deibel C., Strobel T., and Dyakonov V.* Origin of the Efficient Polaron-Pair Dissociation in Polymer-Fullerene Blends. *Phys. Rev. Lett.* **103** (2009), 036402. doi:10.1103/PhysRevLett.103.036402.

[36] *Ohkita H., Cook S., Astuti Y., Duffy W., Tierney S., Zhang W., Heeney M., McCulloch I., Nelson J., Bradley D.D.C., and Durrant J.R.* Charge Carrier Formation in Polythiophene/Fullerene Blend Films Studied by Transient Absorption Spectroscopy. *J. Am. Chem. Soc.* **130** (2008), 3030. doi:10.1021/ja076568q.

[37] *Pelzer K.M., Chan M., and Gray S.K.* Polaron Structure and Transport in Fullerene Materials: Insights from First-Principles Calculations. *J. Phys. Chem. C* (2014).

[38] *Lauchlan L., Etemad S., Chung T.C., Heeger A.J., and MacDiarmid A.G.* Photoexcitations in polyacetylene. *Phys. Rev. B* **24** (1981), 3701. doi:10.1103/PhysRevB.24.3701.

[39] *Deibel C. and Dyakonov V.* Polymer–fullerene bulk heterojunction solar cells. *Reports on Prog. Phys.* **73** (2010), 096401. doi:10.1088/0034-4885/73/9/096401.

[40] *Zenz C., Cerullo G., Lanzani G., Graupner W., Meghdadi F., Leising G., and De Silvestri S.* Ultrafast photogeneration mechanisms of triplet states in para-hexaphenyl. *Phys. Rev. B* **59** (1999), 14336. doi:10.1103/PhysRevB.59.14336.

[41] *Dyakonov V. and Frankevich E.* On the role played by polaron pairs in photophysical processes in semiconducting polymers. *Chem. Phys.* **227** (1998), 203. doi:10.1016/S0301-0104(97)00305-4.

[42] *Vanlaeke P., Swinnen A., Haeldermans I., Vanhoyland G., Aernouts T., Cheyns D., Deibel C., D'Haen J., Heremans P., Poortmans J., and Manca J.V.* P3HT/PCBM bulk heterojunction solar cells: Relation between morphology and electro-optical characteristics. *Sol. Energy Mater. Sol. Cells* **90** (2006), 2150. doi:10.1016/j.solmat.2006.02.010.

[43] *Izumi T., Kobashi S., Takimiya K., Aso Y., and Otsubo T.* Synthesis and Spectroscopic Properties of a Series of β-Blocked Long Oligothiophenes up to the 96-mer: Revaluation of Effective Conjugation Length. *J. Am. Chem. Soc.* **125** (2003), 5286. doi:10.1021/ja034333i.

[44] *Swanson L.S., Shinar J., and Yoshino K.* Optically detected magnetic resonance study of polaron and triplet-exciton dynamics in poly (3-hexylthiophene) and poly (3-dodecylthiophene) films and solutions. *Phys. Rev. Lett.* **65** (1990), 1140. doi:10.1103/PhysRevLett.65.1140.

[45] *Chu C.W., Yang H., Hou W.J., Huang J., Li G., and Yang Y.* Control of the nanoscale crystallinity and phase separation in polymer solar cells. *Appl. Phys. Lett.* **92** (2008), 103306. doi:10.1063/1.2891884.

[46] *Väth S. Winkelaufgelöste Photolumineszenz detektierte Magnetresonanz an organischen Halbleitern*. Master's thesis, Julius Maximilian University of Würzburg, **2011**.

[47] *Marks T.J.* Inorganic and Organic/Plastic Photovoltaics. In *NSF/ONR workshop on Key Scientific and Technological Issues for Development of Next-Generation Organic Solar Cells*, pages 1–30. **2012**.

[48] *Liang Y., Xu Z., Xia J., Tsai S.T., Wu Y., Li G., Ray C., and Yu L.* For the Bright Future-Bulk Heterojunction Polymer Solar Cells with Power Conversion Efficiency of 7.4%. *Adv. Mater.* **22** (2010), E135. doi:10.1002/adma.200903528.

[49] *He Z., Zhong C., Su S., Xu M., Wu H., and Cao Y.* Enhanced power-conversion efficiency in polymer solar cells using an inverted device structure. *Nat. Photonics* **6** (2012), 593. doi:10.1038/nphoton.2012.190.

[50] *Szarko J.M., Guo J., Liang Y., Lee B., Rolczynski B.S., Strzalka J., Xu T., Loser S., Marks T.J., and Yu L.* When function follows form: effects of donor copolymer side chains on film morphology and BHJ solar cell performance. *Adv. Mater.* **22** (2010), 5468. doi:10.1002/adma.201002687.

[51] *Wagner J., Gruber M., Hinderhofer A., Wilke A., Bröker B., Frisch J., Amsalem P., Vollmer A., Opitz A., Koch N., Schreiber F., and Brütting W.* High Fill Factor and Open Circuit Voltage in Organic Photovoltaic Cells with Diindenoperylene as Donor Material. *Adv. Funct. Mater.* **20** (2010), 4295. doi:10.1002/adfm.201001028.

[52] *Verreet B., Cnops K., Cheyns D., Heremans P., Stesmans A., Zango G., Claessens C.G., Torres T., and Rand B.P.* Decreased Recombination Through the Use of a Non-Fullerene Acceptor in a 6.4% Efficient Organic Planar Heterojunction Solar Cell. *Adv. Energy Mater.* **4** (2014), 1301413. doi:10.1002/aenm.201301413.

[53] *Yu S., Opitz A., Grob S., Resel R., Oehzelt M., Brütting W., Salzmann I., and Koch N.* Organic Electronics. *Org. Electron.* **15** (2014), 2210. doi:10.1016/j.orgel.2014.06.023.

[54] *Lane P.A., Swanson L.S., Ni Q.X., Shinar J., Engel J.P., Barton T.J., and Jones L.* Dynamics of photoexcited states in C 60: An optically detected magnetic resonance, ESR, and light-induced ESR study. *Phys. Rev. Lett.* **68** (1992), 887. doi:10.1103/PhysRevLett.68.887.

[55] *Liedtke M., Sperlich A., Kraus H., Baumann A., Deibel C., Wirix M.J.M., Loos J., Cardona C.M., and Dyakonov V.* Triplet Exciton Generation in Bulk-Heterojunction Solar Cells Based on Endohedral Fullerenes. *J. Am. Chem. Soc.* **133** (2011), 9088. doi:10.1021/ja2025432.

[56] *Foertig A., Kniepert J., Gluecker M., Brenner T., Dyakonov V., Neher D., and Deibel C.* Nongeminate and Geminate Recombination in PTB7:PCBM Solar Cells. *Adv. Funct. Mater.* **24** (2013), 1306. doi:10.1002/adfm.201302134.

[57] *Jarzab D., Cordella F., Gao J., Scharber M., Egelhaaf H.J., and Loi M.A.* Low-Temperature Behaviour of Charge Transfer Excitons in Narrow-Bandgap Polymer-Based Bulk Heterojunctions. *Adv. Energy Mater.* (2011). doi:10.1002/aenm.201100083.

[58] *Cleveland J.P., Anczykowski B., Schmid A.E., and Elings V.B.* Energy dissipation in tapping-mode atomic force microscopy. *Appl. Phys. Lett.* **72** (1998), 2613. doi:10.1063/1.121434.

[59] *Ochiai S., Imamura S., Kannappan S., Palanisamy K., and Shin P.K.* Current Applied Physics. *Curr. Appl. Phys.* (2013), 1. doi:10.1016/j.cap.2013.01.010.

[60] *Lee M.K., Segal M., Soos Z., Shinar J., and Baldo M.* Yield of Singlet Excitons in Organic Light-Emitting Devices: A Double Modulation Photoluminescence-Detected Magnetic Resonance Study. *Phys. Rev. Lett.* **94** (2005), 137403. doi:10.1103/PhysRevLett.94.137403.

[61] *Lane P.A., Shinar J., and Yoshino K.* Photoluminescence-detected magnetic-resonance study of fullerene-doped π-conjugated polymers. *Phys. Rev. B* **54** (1996), 9308. doi:10.1103/PhysRevB.54.9308.

[62] *Lou S.J., Szarko J.M., Xu T., Yu L., Marks T.J., and Chen L.X.* Effects of Additives on the Morphology of Solution Phase Aggregates Formed by Active Layer Components of High-Efficiency Organic Solar Cells. *J. Am. Chem. Soc.* **133** (2011), 20661. doi:10.1021/ja2085564.

[63] *Deibel C., Mack D., Gorenflot J., Rauh D., and Dyakonov V.* Energetics of excited states in the conjugated polymer poly(3-hexylthiophene). *Phys. Rev. B* **81** (2010). doi:10.1103/PhysRevB.81.085202.

[64] *Liang Y., Xiao S., Feng D., and Yu L.* Control in energy levels of conjugated polymers for photovoltaic application. *J. Phys. Chem. C* **112** (2008), 7866. doi:10.1021/jp711623w.

[65] *Vandewal K., Gadisa A., Oosterbaan W.D., Bertho S., Banishoeib F., Van Severen I., Lutsen L., Cleij T.J., Vanderzande D., and Manca J.V.* The Relation Between Open-Circuit Voltage and the Onset of Photocurrent Generation by Charge-Transfer Absorption in Polymer: Fullerene Bulk Heterojunction Solar Cells. *Adv. Funct. Mater.* **18** (2008), 2064. doi:10.1002/adfm.200800056.

[66] *Mola G.T. and Abera N.* Correlation between LUMO offset of donor/acceptor molecules to an open circuit voltage in bulk heterojunction solar cell. *Phys. B: Condens. Matter* **445** (2014), 56. doi:10.1016/j.physb.2014.04.004.

[67] *Hodes G. and Cahen D.* Perovskite cells roll forward. *Nat. Photonics* (2014), 1. doi:10.1038/nphoton.2014.5.

[68] *Iijima S.* Helical microtubules of graphitic carbon. *Nat.* **354** (1991), 56. doi:10.1038/354056a0.

[69] *Lukyanovich V.M. and Radushkevich L.V.* О структуре углерода, образующегося при термическом разложении окиси углерода на железном контакте. *Журнал физической химии* **26** (1952), 395.

[70] *Oberlin A., Endo M., and Koyama T.* Filamentous Growth of Carbon Through Benzene Decomposition. *J. Cryst. Growth* **32** (1976), 335. doi:10.1016/0022-0248(76)90115-9.

[71] *Monthioux M. and Kuznetsov V.L.* Who should be given the credit for the discovery of carbon nanotubes? *Carbon* **44** (2006), 1621. doi:10.1016/j.carbon.2006.03.019.

[72] *Iijima S. and Ichihashi T.* Single-shell carbon nanotubes of 1-nm diameter. *Nat.* **363** (1993), 603. doi:10.1038/363603a0.

[73] *Bethune D.S., Klang C.H., de Vries M.S., Gorman G., Savoy R., Vazquez J., and Beyers R.* Cobalt-catalysed growth of carbon nanotubes with single-atomic-layer walls. *Nat.* **363** (1993), 605. doi:10.1038/363605a0.

[74] *Kalaugher L.* Nanotube bike enters Tour de France - nanotechweb.org, **2005**.

[75] *Pugno N.M.* On the strength of the carbon nanotube-based space elevator cable: from nanomechanics to megamechanics. *J. Physics: Condens. Matter* **18** (2006), S1971. doi:10.1088/0953-8984/18/33/S14.

[76] *Edwards B.C.* Design and deployment of a space elevator. *Acta Astronaut.* **47** (2000), 735. doi:10.1016/S0094-5765(00)00111-9.

[77] *Gannon C.J., Cherukuri P., Yakobson B.I., Cognet L., Kanzius J.S., Kittrell C., Weisman R.B., Pasquali M., Schmidt H.K., Smalley R.E., and Curley S.A.* Carbon nanotube-enhanced thermal destruction of cancer cells in a noninvasive radiofrequency field. *Cancer* **110** (2007), 2654. doi:10.1002/cncr.23155.

[78] *Bachtold A.* Logic Circuits with Carbon Nanotube Transistors. *Sci.* **294** (2001), 1317. doi:10.1126/science.1065824.

[79] *Misewich J.A., Martel R., Avouris P., Tsang J.C., Heinze S., and Tersoff J.* Electrically induced optical emission from a carbon nanotube FET. *Sci.* **300** (2003), 783. doi:10.1126/science.1081294.

[80] *Avouris P., Freitag M., and Perebeinos V.* Carbon-nanotube photonics and optoelectronics. *Nat. Photonics* **2** (2008), 341. doi:10.1038/nphoton.2008.94.

[81] *Wen Q., Qian W., Nie J., Cao A., Ning G., Wang Y., Hu L., Zhang Q., Huang J., and Wei F.* 100mm Long, Semiconducting Triple-Walled Carbon Nanotubes. *Adv. Mater.* **22** (2010), 1867. doi:10.1002/adma.200902746.

[82] *Saito R., Fujita M., Dresselhaus G., and Dresselhaus M.S.* Electronic structure of chiral graphene tubules. *Appl. Phys. Lett.* **60** (1992), 2204. doi:10.1063/1.107080.

[83] *Lu X. and Chen Z.* Curved Pi-Conjugation, Aromaticity, and the Related Chemistry of Small Fullerenes (. *Chem. Rev.* **105** (2005), 3643. doi:10.1021/cr030093d.

[84] *Lefebvre J. and Finnie P.* Polarized Photoluminescence Excitation Spectroscopy of Single-Walled Carbon Nanotubes. *Phys. Rev. Lett.* **98** (2007), 167406. doi:10.1103/PhysRevLett.98.167406.

[85] *Lebedkin S., Hennrich F., Kiowski O., and Kappes M.* Photophysics of carbon nanotubes in organic polymer-toluene dispersions: Emission and excitation satellites and relaxation pathways. *Phys. Rev. B* 77 (2008), 165429. doi:10.1103/PhysRevB.77.165429.

[86] *Kato K., Koretsune T., and Saito S.* Energetics and electronic properties of twisted single-walled carbon nanotubes. *Phys. Rev. B* **85** (2012), 115448. doi:10.1103/PhysRevB.85.115448.

[87] *Slonczewski J.C. and Weiss P.R.* Band structure of graphite. *Phys. Rev.* **109** (1958), 272. doi:10.1103/PhysRev.109.272.

[88] *Ando T.* Effects of Valley Mixing and Exchange on Excitons in Carbon Nanotubes with Aharonov–Bohm Flux. *J. Phys. Soc. Jpn.* **75** (2006), 024707. doi:10.1143/JPSJ.75.024707.

[89] *Barros E.B., Jorio A., Samsonidze G.G., Capaz R.B., Souza Filho A.G., Mendes Filho J., Dresselhaus G., and Dresselhaus M.S.* Review on the Symmetry-related Properties of Carbon Nanotubes. *Phys. Reports* **431** (2006), 261. doi:10.1016/j.physrep.2006.05.007.

[90] *Ando T.* Excitons in Carbon Nanotubes. *J. Phys. Soc. Jpn.* **66** (1997), 1066. doi:10.1143/JPSJ.66.1066.

[91] *Jiang J., Saito R., Samsonidze G., Jorio A., Chou S., Dresselhaus G., and Dresselhaus M.* Chirality dependence of exciton effects in single-wall carbon nanotubes: Tight-binding model. *Phys. Rev. B* **75** (2007), 035407. doi:10.1103/PhysRevB.75.035407.

[92] *Jankus V., Snedden E.W., Bright D.W., Whittle V.L., Williams J.A.G., and Monkman A.* Energy Upconversion via Triplet Fusion in Super Yellow PPV Films Doped with Palladium Tetraphenyltetrabenzoporphyrin: a Comprehensive Investigation of Exciton Dynamics. *Adv. Funct. Mater.* (2012), n/a. doi:10.1002/adfm.201201284.

[93] *Smith M.B. and Michl J.* Singlet Fission. *Chem. Rev.* **110** (2010), 6891. doi:10.1021/cr1002613.

[94] *Högele A., Galland C., Winger M., and Imamoğlu A.* Photon Antibunching in the Photoluminescence Spectra of a Single Carbon Nanotube. *Phys. Rev. Lett.* **100** (2008), 217401. doi:10.1103/PhysRevLett.100.217401.

[95] *Perebeinos V., Tersoff J., and Avouris P.* Radiative lifetime of excitons in carbon nanotubes. *Nano Lett.* **5** (2005), 2495. doi:10.1021/nl051828s.

[96] *Tretiak S.* Triplet state absorption in carbon nanotubes: A TD-DFT study. *Nano Lett.* 7 (2007), 2201. doi:10.1021/nl070355h.

[97] *Park J., Deria P., and Therien M.J.* Dynamics and Transient Absorption Spectral Signatures of the Single-Wall Carbon Nanotube Electronically Excited Triplet State. *J. Am. Chem. Soc.* **133** (2011), 17156. doi:10.1021/ja2079477.

[98] *Wang F., Dukovic G., Brus L., and Heinz T.* Time-Resolved Fluorescence of Carbon Nanotubes and Its Implication for Radiative Lifetimes. *Phys. Rev. Lett.* **92** (2004), 177401. doi:10.1103/PhysRevLett.92.177401.

[99] *Ju S.Y., Kopcha W.P., and Papadimitrakopoulos F.* Brightly Fluorescent Single-Walled Carbon Nanotubes via an Oxygen-Excluding Surfactant Organization. *Sci.* **323** (2009), 1319. doi:10.1126/science.1166265.

[100] *Kobayashi K.* A theoretical study of C80 and La2@C80. *Chem. Phys. Lett.* **245** (1995), 230. doi:10.1016/0009-2614(95)00991-C.

[101] *Collins P.G.* Extreme Oxygen Sensitivity of Electronic Properties of Carbon Nanotubes. *Sci.* **287** (2000), 1801. doi:10.1126/science.287.5459.1801.

[102] *Ozawa H., Ide N., Fujigaya T., Niidome Y., and Nakashima N.* One-pot Separation of Highly Enriched (6,5)-Single-walled Carbon Nanotubes Using a Fluorene-based Copolymer. *Chem. Lett.* **40** (2011), 239. doi:10.1246/cl.2011.239.

[103] *Schöppler F., Rühl N., and Hertel T.* Photoluminescence microscopy and spectroscopy of individualized and aggregated single-wall carbon nanotubes. *Chem. Phys.* **413** (2013), 112. doi:10.1016/j.chemphys.2012.08.011.

[104] *Späth F.* Personal Communication: Polarimetry of stretched (6,5) SWNT in a PFO-BPy-Polystyrene matrix, **2014**.

[105] *Epshtein O., Eichen Y., Ehrenfreund E., Wohlgenannt M., and VARDENY Z.* Linear and nonlinear photoexcitation dynamics in pi-conjugated polymers. *Phys. Rev. Lett.* **90** (2003), 046804. doi:10.1103/PhysRevLett.90.046804.

[106] *Hertel T., Perebeinos V., Crochet J., Arnold K., Kappes M., and Avouris P.* Intersubband Decay of 1-D Exciton Resonances in Carbon Nanotubes. *Nano Lett.* **8** (2008), 87. doi:10.1021/nl0720915.

[107] *Niklas J., Holt J.M., Mistry K., Rumbles G., Blackburn J.L., and Poluektov O.G.* Charge Separation in P3HT:SWCNT Blends Studied by EPR: Spin Signature of the Photoinduced Charged State in SWCNT. *J. Phys. Chem. Lett.* **5** (2014), 601. doi:10.1021/jz402668h.

[108] *Auth M. Elektronen-Spin-Resonanz Untersuchung von Ladungstransfer zwischen Kohlenstoffnanoröhren, Polymeren und Fullerenen*. Bachelor's thesis, Julius Maximilian University of Würzburg, **2014**.

[109] *Ern V. and Merrifield R.E.* Magnetic field effect on triplet exciton quenching in organic crystals. *Phys. Rev. Lett.* **21** (1968), 609. doi:10.1103/PhysRevLett.21.609.

[110] *Bouchriha H., Schott M., Bisceglia M., and Delacote G.* Quenching of triplet excitions by trapped holes in crystalline pyrene. *Chem. Phys. Lett.* **23** (1973), 183. doi:10.1016/0009-2614(73)80245-3.

[111] *Segal M., Baldo M., Lee M., Shinar J., and Soos Z.* Frequency response and origin of the spin-1⁄2 photoluminescence-detected magnetic resonance in a π-conjugated polymer. *Phys. Rev. B* **71** (2005). doi:10.1103/PhysRevB.71.245201.

[112] *Manzoni C., Gambetta A., Menna E., Meneghetti M., Lanzani G., and Cerullo G.* Intersubband Exciton Relaxation Dynamics in Single-Walled Carbon Nanotubes. *Phys. Rev. Lett.* **94** (2005), 207401. doi:10.1103/PhysRevLett.94.207401.

[113] *Habenicht B.F. and Prezhdo O.V.* Ab Initio Time-Domain Study of the Triplet State in a Semiconducting Carbon Nanotube: Intersystem Crossing, Phosphorescence Time, and Line Width. *J. Am. Chem. Soc.* **134** (2012), 15648. doi:10.1021/ja305685v.

[114] *Riedel D., Fuchs F., Kraus H., Väth S., Sperlich A., Dyakonov V., Soltamova A.A., Baranov P.G., Ilyin V.A., and Astakhov G.V.* Resonant addressing and manipulation of silicon vacancy qubits in silicon carbide. *Phys. Rev. Lett.* **109** (2012), 226402. doi:10.1103/PhysRevLett.109.226402.

[115] *Kraus H., Soltamov V.A., Riedel D., Väth S., Fuchs F., Sperlich A., Baranov P.G., Dyakonov V., and Astakhov G.V.* Room-temperature quantum microwave emitters based on spin defects in silicon carbide. *Nat. Phys.* **10** (2013), 1. doi:10.1038/nphys2826.

[116] *Feynman R.P.* Simulating physics with computers. *Int. journal Theor. Phys.* **21** (1982), 467. doi:10.1007/BF02650179.

[117] *Deutsch D.* Quantum theory, the Church-Turing principle and the universal quantum computer. *Proc. Royal Soc. Lond. A. Math. Phys. Sci.* **400** (1985), 97. doi:10.1098/rspa.1985.0070.

[118] *Bos J.W., Halderman J.A., Heninger N., Moore J., Naehrig M., and Wustrow E.* Elliptic Curve Cryptography in Practice. In *Financial Cryptography and Data Security*. Springer, **2014**.

[119] *Shor P.W.* Algorithms for quantum computation: discrete logarithms and factoring. In *35th Annual Symposium on Foundations of Computer Science*, pages 124–134. IEEE Comput. Soc. Press. ISBN 0-8186-6580-7. doi:10.1109/SFCS.1994.365700.

[120] *Pomerance C.* Smooth numbers and the quadratic sieve. In J.P. Buhler and P. Stevenhagen, editors, *Algorithmic number theory: lattices, number fields, curves and cryptography*, pages 69–81. Cambridge University Press, **2008**. ISBN 978-0-521-80854-5.

[121] *Rebentrost P., Mohseni M., and Lloyd S.* Quantum support vector machine for big feature and big data classification. *arXiv.org* (2013), 1307.0471.

[122] *Grover L.K.* A fast quantum mechanical algorithm for database search. In *Proceedings of the twenty-eighth annual ACM symposium on Theory of computing*, pages 212–219. ACM, **1996**. ISBN 0897917855.

[123] *DiVincenzo D.P.* The Physical Implementation of Quantum Computation. *Fortschritte der Physik* **48** (2000), 771. doi:10.1002/1521-3978(200009)48:9/11<771::AID-PROP771>3.0.CO;2-E.

[124] *Kane B.E.* A silicon-based nuclear spin quantum computer. *Nat.* **393** (1998), 133. doi:10.1038/30156.

[125] *Tyryshkin A.M., Tojo S., Morton J.J.L., Riemann H., Abrosimov N.V., Becker P., Pohl H.J., Schenkel T., Thewalt M.L.W., Itoh K.M., and Lyon S.A.* Electron spin coherence exceeding seconds in high-purity silicon. *Nat. Mater.* **11** (2011), 143. doi:10.1038/nmat3182.

[126] *Saeedi K., Simmons S., Salvail J.Z., Dluhy P., Riemann H., Abrosimov N.V., Becker P., Pohl H.J., Morton J.J.L., and Thewalt M.L.W.* Room-Temperature Quantum Bit Storage Exceeding 39 Minutes Using Ionized Donors in Silicon-28. *Sci.* **342** (2013), 830. doi:10.1126/science.1239584.

[127] *Loss D. and DiVincenzo D.P.* Quantum computation with quantum dots. *Phys. Rev. A* **57** (1998), 120. doi:10.1103/PhysRevA.57.120.

[128] *Hanson R., Kouwenhoven L.P., Petta J.R., Tarucha S., and Vandersypen L.* Spins in few-electron quantum dots. *Rev. Mod. Phys.* **79** (2007), 1217. doi:10.1103/RevModPhys.79.1217.

[129] *Petta J.R., Johnson A.C., Taylor J.M., Laird E.A., Yacoby A., Lukin M.D., Marcus C.M., Hanson M.P., and Gossard A.C.* Coherent manipulation of coupled electron spins in semiconductor quantum dots. *Sci.* **309** (2005), 2180. doi:10.1126/science.1116955.

[130] *Gruber A., Dräbenstedt A., Tietz C., Fleury L., Wrachtrup J., and Von Borczyskowski C.* Scanning confocal optical microscopy and magnetic resonance on single defect centers. *Sci.* **276** (1997), 2012. doi:10.1126/science.276.5321.2012.

[131] *Jelezko F. and Wrachtrup J.* Single defect centres in diamond: A review. *Phys. Status Solidi A* **203** (2006), 3207. doi:10.1002/pssa.200671403.

[132] *Weber J.R., Koehl W.F., Varley J.B., Janotti A., Buckley B.B., Van de Walle C.G., and Awschalom D.D.* Quantum computing with defects. *PNAS* **107** (2010), 8513. doi:10.1073/pnas.1003052107.

[133] *DiVincenzo D.* Quantum bits: Better than excellent. *Nat. Mater.* **9** (2010), 468. doi:10.1038/nmat2774.

[134] *Chen W.K. The VLSI Handbook, Second Edition*. Electrical Engineering Handbook. CRC Press, **2006**. ISBN 9781420005967.

[135] *Ivanov A.M., Strokan N.B., Davydov D.V., Savkina N.S., Lebedev A.A., Mironov Y.T., Riabov G.A., and Ivanov E.M.* Radiation hardness of SiC based ions detectors for influence of the relative protons. *Appl. Surf. Sci.* **184** (2001), 431. doi:10.1016/S0169-4332(01)00529-3.

[136] *Moscatelli F., Scorzoni A., Poggi A., Bruzzi M., Sciortino S., Lagomarsino S., Wagner G., Mandic I., and Nipoti R.* Radiation hardness after very high neutron irradiation of minimum ionizing particle detectors based on 4H-SiC p/sup +/n junctions. *IEEE Transactions on Nucl. Sci.* **53** (2006), 1557. doi:10.1109/TNS.2006.872202.

[137] *Choyke W.J. and Pensl G.* Siliciumkarbid—Halbleiter für die neunziger Jahre. *Physikalische Blätter* **47** (1991), 212.

[138] *Lely J.A.* US Patent 2854364: Sublimation Process for Manufacturing Silicon Carbide Crystals. United States Patent Office, **1958**.

[139] *Tairov Y.M. and Tsvetkov V.F.* Investigation of growth processes of ingots of silicon carbide single crystals. *J. Cryst. Growth* **43** (1978), 209. doi:10.1016/0022-0248(78)90169-0.

[140] *Chen D., Sixta M.E., Zhang X.F, De Jonghe L.C., and Ritchie R.O.* Role of the grain-boundary phase on the elevated-temperature strength, toughness, fatigue and creep resistance of silicon carbide sintered with Al, B and C. *Acta Materialia* **48** (2000), 4599. doi:10.1016/S1359-6454(00)00246-9.

[141] *Bergman J.P., Storasta L., Carlsson F., Sridhara S., Magnusson B., and Janzén E.* Defects in 4H silicon carbide. *Phys. B: Condens. Matter* **308** (2001), 675. doi:10.1016/S0921-4526(01)00790-6.

[142] *Sridhara S.G., Carlsson F.H.C., Bergman J.P., and Janzén E.* Luminescence from stacking faults in 4H SiC. *Appl. Phys. Lett.* **79** (2001), 3944. doi:10.1063/1.1425084.

[143] *von Bardeleben H.J., Cantin J.L., Henry L., and Barthe M.F.* Vacancy defects in p-type 6H-SiC created by low-energy electron irradiation. *Phys. Rev. B* **62** (2000), 10841. doi:10.1103/PhysRevB.62.10841.

[144] *Hagen S.H. and Van Kemenade A.* Infrared luminescence in silicon carbide. *J. Lumin.* **9** (1974), 9. doi:10.1016/0022-2313(74)90066-0.

[145] *Kawasuso A., Itoh H., Okada S., and Okumura H.* Annealing processes of vacancy-type defects in electron-irradiated and as-grown 6H-SiC studied by positron lifetime spectroscopy. *J. Appl. Phys.* **80** (1996), 5639. doi:10.1063/1.363615.

[146] *Fuchs F., Stender B., Trupke M., Pflaum J., Dyakonov V., and Astakhov G.V.* Engineering near infrared single photon emitters in ultrapure silicon carbide. *arXiv.org* (2014), 1407.7065.

[147] *Wagner M., Magnusson B., Chen W.M., Janzén E., Sörman E., Hallin C., and Lindström J.L.* Electronic structure of the neutral silicon vacancy in 4 H and 6 H SiC. *Phys. Rev. B* **62** (2000), 16555. doi:10.1103/PhysRevB.62.16555.

[148] *Wagner M., Magnusson B., Chen W.M., and Janzén E.* Electronic Structure of the UD3 Defect in 4H-and 6H-SiC. In *Materials Science Forum*, pages 509–512. Trans Tech Publ, **2002**. ISBN 087849894X. doi:10.4028/www.scientific.net/MSF.389-393.509.

[149] *Sörman E., Son N.T., Chen W.M., Kordina O., Hallin C., and Janzén E.* Silicon vacancy related defect in 4H and 6H SiC. *Phys. Rev. B* **61** (2000), 2613. doi:10.1103/PhysRevB.61.2613.

[150] *Wimbauer T., Meyer B.K., Hofstaetter A., Scharmann A., and Overhof H.* Negatively charged Si vacancy in 4 H SiC: A comparison between theory and experiment. *Phys. Rev. B* **56** (1997), 7384. doi:10.1103/PhysRevB.56.7384.

[151] *Zywietz A., Furthmuller J., and Bechstedt F.* Vacancies in SiC: Influence of Jahn-Teller distortions, spin effects, and crystal structure. *Phys. Rev. B* **59** (1999), 15166. doi:10.1103/PhysRevB.59.15166.

[152] *Orlinskii S.B., Schmidt J., Mokhov E.N., and Baranov P.G.* Silicon and carbon vacancies in neutron-irradiated SiC: A high-field electron paramagnetic resonance study. *Phys. Rev. B* **67** (2003), 125207. doi:10.1103/PhysRevB.67.125207.

[153] *Mizuochi N., Yamasaki S., Takizawa H., Morishita N., Ohshima T., Itoh H., Umeda T., and Isoya J.* Spin multiplicity and charge state of a silicon vacancy (T_{V2a}) in 4H-SiC determined by pulsed ENDOR. *Phys. Rev. B* **72** (2005), 235208. doi:10.1103/PhysRevB.72.235208.

[154] *Isoya J., Umeda T., Mizuochi N., Son N.T., Janzén E., and Ohshima T.* EPR identification of intrinsic defects in SiC. *Phys. Status Solidi B* **245** (2008), 1298. doi:10.1002/pssb.200844209.

[155] *Bassett L.C., Heremans F.J., Yale C.G., Buckley B.B., and Awschalom D.D.* Electrical Tuning of Single Nitrogen-Vacancy Center Optical Transitions Enhanced by Photoinduced Fields. *Phys. Rev. Lett.* **107** (2011), 266403. doi:10.1103/PhysRevLett.107.266403.

[156] *Hafizovic S.* Sideband Analysis with Lock-in Amplifiers `http://www.zhinst.com/blogs/sadik/2014/02/sideband-analysis/`, **2014**.

[157] *Hughes V.W. and Geiger J.S.* Two-quantum transitions in the microwave Zeeman spectrum of atomic oxygen. *Phys. Rev.* **99** (1955), 1842. doi:10.1103/PhysRevLett.112.068103.

[158] *Aminov L.K.* Perturbation-theory calculations of two-quantum relaxation processes. *Zh. Eksp. Teor. Fiz* **67** (1974), 79.

[159] *van Dam P.J., Klaassen A.A., Reijerse E.J., and Hagen W.R.* Application of high frequency EPR to integer spin systems: Unusual behavior of the double-quantum line. *J. Magn. Reson.* **130** (1998), 140. doi:10.1006/jmre.1997.1293.

[160] *Fuchs G.D., Dobrovitski V.V., Hanson R., Batra A., Weis C.D., Schenkel T., and Awschalom D.D.* Excited-State Spectroscopy Using Single Spin Manipulation in Diamond. *Phys. Rev. Lett.* **101** (2008), 117601. doi:10.1103/PhysRevLett.101.117601.

[161] *Aharonovich I. and Toth M.* Optical materials: Silicon carbide goes quantum. *Nat. Phys.* **10** (2014), 93. doi:10.1038/nphys2858.

[162] *Kimble H., Dagenais M., and Mandel L.* Photon Antibunching in Resonance Fluorescence. *Phys. Rev. Lett.* **39** (1977), 691. doi:10.1103/PhysRevLett.39.691.

[163] *Castelletto S., Johnson B.C., Ivády V., Stavrias N., Umeda T., Gali A., and Ohshima T.* A silicon carbide room-temperature single-photon source. *Nat. Mater.* **12** (2013), 1. doi:10.1038/namt3806.

[164] *Basché T., Moerner W.E., Orrit M., and Talon H.* Photon antibunching in the fluorescence of a single dye molecule trapped in a solid. *Phys. Rev. Lett.* **69** (1992), 1516. doi:10.1103/PhysRevLett.69.1516.

[165] *Kurtsiefer C., Mayer S., Zarda P., and Weinfurter H.* Stable solid-state source of single photons. *Phys. Rev. Lett.* **85** (2000), 290. doi:10.1103/PhysRevLett.85.290.

[166] *Poole C.P. Electron Spin Resonance: A Comprehensive Treatise on Exprimental Techniques*. John Wiley & Sons, Ltd., **1967**.

[167] *Rupp H., Rao K.K., Hall D.O., and Cammack R.* Electron spin relaxation of iron-sulphur proteins studied by microwave power saturation. *Biochimica et Biophys. Acta (BBA)-Protein Struct.* **537** (1978), 255. doi:10.1016/0005-2795(78)90509-3.

[168] *Weber J.* Masers. *Rev. Mod. Phys.* **31** (1959), 681. doi:10.1103/RevModPhys.31.681.

[169] *Kikuchi C., Lambe J., Makhov G., and Terhune R.W.* Ruby as a maser material. *J. Appl. Phys.* **30** (1959), 1061. doi:10.1063/1.1776979.

[170] *Kornienko L.S. and Shteinsteiger V.B.* Quantum amplifiers and their application in space research. *Sov. Phys. Uspekhi* **21** (1978), 852. doi:10.1070/PU1978v021n10ABEH005687.

[171] *Moore C.R. and Clauss R.C.* A reflected-wave ruby maser with K-band tuning range and large instantaneous bandwidth. *IEEE Transactions on Microw. Theory Tech.* **27** (1979), 249. doi:10.1109/TMTT.1979.1129602.

[172] *Pospieszalski M.W.* Extremely low-noise amplification with cryogenic FETs and HFETs: 1970-2004. *Microw. Mag. IEEE* **6** (2005), 62. doi:10.1109/MMW.2005.1511915.

[173] *Blank A., Kastner R., and Levanon H.* Exploring new active materials for low-noise room-temperature microwave amplifiers and other devices. *IEEE Transactions on Microw. Theory Tech.* **46** (1998), 2137. doi:10.1109/22.739295.

[174] *Oxborrow M., Breeze J.D., and Alford N.M.* Room-temperature solid-state maser. *Nat.* **488** (2012), 353. doi:10.1038/nature11339.

[175] *Lingner T., Greulich-Weber S., Spaeth J.M., Gerstmann U., Rauls E., Hajnal Z., Frauenheim T., and Overhof H.* Structure of the silicon vacancy in 6H-SiC after annealing identified as the carbon vacancy-carbon antisite pair. *Phys. Rev. B* **64** (2001), 245212. doi:10.1103/PhysRevB.64.245212.

[176] *Baranov P.G., Il'in I.V., Mokhov E.N., Muzafarova M.V., Orlinskii S.B., and Schmidt J.* EPR identification of the triplet ground state and photoinduced population inversion for a Si-C divacancy in silicon carbide. *J. Exp. Theor. Phys. Lett.* **82** (2005), 441. doi:10.1134/1.2142873.

[177] *Ilyin I.V., Muzafarova M.V., Mokhov E.N., Sankin V.I., Baranov P.G., Orlinskii S.B., and Schmidt J.* Evidence of the Ground Triplet State of Silicon-Carbon Divacancies (P6, P7 Centers) in 6H SiC: An EPR Study. In *Materials Science Forum*, pages 535–538. Trans Tech Publ, **2006**. ISBN 0878494251. doi:10.4028/www.scientific.net/MSF.527-529.535.

[178] *Acosta V.M., Bauch E., Ledbetter M.P., Waxman A., Bouchard L.S., and Budker D.* Temperature dependence of the nitrogen-vacancy magnetic resonance in diamond. *Phys. Rev. Lett.* **104** (2010), 070801. doi:10.1103/PhysRevLett.104.070801.

[179] *Acosta V.M., Bauch E., Ledbetter M.P., Waxman A., Bouchard L.S., and Budker D.* Erratum: temperature dependence of the nitrogen-vacancy magnetic resonance in diamond [phys. Rev. Lett. 104, 070801 (2010)]. *Phys. Rev. Lett.* **106** (2011), 209901. doi:10.1103/PhysRevLett.106.209901.

[180] *Kern E.L., Hamill D.W., Deem H.W., and Sheets H.D.* Thermal properties of beta silicon carbide from 20 to 2000 C. *Mater. Res. Bull.* **4** (1969), S25.

[181] *Yamaguchi S., Okimoto Y., and Tokura Y.* Local lattice distortion during the spin-state transition in $LaCoO_3$. *Phys. Rev. B* **55** (1997), R8666. doi:10.1103/PhysRevB.55.R8666.

[182] *Childress L., Dutt M.V.G., Taylor J.M., Zibrov A.S., Jelezko F., Wrachtrup J., Hemmer P.R., and Lukin M.D.* Coherent dynamics of coupled electron and nuclear spin qubits in diamond. *Sci.* **314** (2006), 281. doi:10.1126/science.1131871.

[183] *Mizuochi N., Yamasaki S., Takizawa H., Morishita N., Ohshima T., Itoh H., and Isoya J.* EPR studies of the isolated negatively charged silicon vacancies in n-type 4H- and 6H-SiC: Identification of C3v symmetry and silicon sites. *Phys. Rev. B* **68** (2003), 165206. doi:10.1103/PhysRevB.68.165206.

A. Appendix

Publications and conference contributions

Awards and Grants

- DAAD P.R.I.M.E. postdoc scholarship (Marie-Skłodowska-Curie-Action COFUND) for 2015–June 2016
- DAAD conference travel grant for the International Conference on Silicon Carbide and Related Materials 2013 (Miyazaki, Japan)
- Energy & Environmental Science Poster Prize 2013 at the Solar Energy Conversion Meeting, Kloster Banz, Germany 2013
- Upgrade to invited talk at Materials Research Society Spring Meeting 2012 by Prof. Alejandro Briseño
- DAAD conference travel grant for Materials Research Society Spring Meeting 2012 (San Francisco, USA)
- Energy & Environmental Science Poster Prize 2011 at the SPP 1355 summer school together with Andreas Sperlich. Veitshöchheim, Germany 2011

Peer reviewed work

1. *H. Kraus, V. A. Soltamov, F. Fuchs, D. Simin, A. Sperlich, P. G. Baranov, G. V. Astakhov and V. Dyakonov* Magnetic field and temperature sensing with atomic-scale spin defects in silicon carbide. *Sci. Rep.* **4**, 5303 (2014). 10.1038/srep05303

2. *H. Kraus, V. A. Soltamov, D. Riedel, S. Väth, F. Fuchs, A. Sperlich, P. G. Baranov, V. Dyakonov and G. V. Astakhov*. Room-temperature quantum microwave emitters based on spin defects in silicon carbide. *Nat. Phys.* **10**, 157-162 (2014). 10.1038/nphys2826.

3. *D. Stich, F. Späth, H. Kraus, A. Sperlich, V. Dyakonov and T. Hertel*. Triplet-triplet exciton dynamics in single-wall carbon nanotubes. *Nat. Photonics* **8**, 139-144 (2014). doi: 10.1038/nphoton.2013.316.

4. *H. Braunschweig, V. Dyakonov, B. Engels, Z. Falk, C. Hörl, J. Klein, T. Kramer, H. Kraus, I. Krummenacher, C. Lambert and C. Walter*. Multiple Reduction of 2,5-Bis(borolyl)thiophene: Isolation of a Negative Bipolaron by Comproportionation. *Angew. Chem. Int. Ed.* **52**,128522-12855 (2013). doi: 10.1002/anie.201306969

5. *D. Riedel, F. Fuchs, H. Kraus, S. Väth, A. Sperlich, V. Dyakonov, A. A. Soltamova, P. G. Baranov, V. A. Ilyin and G. V. Astakhov*. Resonant addressing and manipulation of silicon vacancy qubits in silicon carbide. *Phys. Rev. Lett.* **109**, 22, 226402 (2012). 10.1103/PhysRevLett.109.226402. arXiv: 1210.0505.

6. *T. Savenije, A. Sperlich, H. Kraus, O. Poluektov, M. Heeney and V. Dyakonov*. Observation of bi-polarons in blends of conjugated copolymers and fullerene derivatives. *Phys. Chem. Chem. Phys.* **13**, 37, 16579 (2011). doi: 10.1039/c1cp21607d. arXiv: 1110.1881.

7. *A. Sperlich, H. Kraus, C. Deibel, H. Blok, J. Schmidt and V. Dyakonov*. Reversible and Irreversible Interactions of Poly(3-hexylthiophene) with Oxygen Studied by Spin-Sensitive Methods. *J. Phys. Chem. B* **115**, 46, 13513 (2011). doi: 10.1021/jp2077215. arXiv: 1110.1316.

8. *M. Liedtke, A. Sperlich, H. Kraus, A. Baumann, C. Deibel, M. J. M. Wirix, J. Loos, C. M. Cardona and V. Dyakonov*. Triplet Exciton Generation in Bulk-Heterojunction Solar Cells Based on Endohedral Fullerenes. *J. Am. Chem. Soc.* **133**, 23, 9088 (2011). doi: 10.1021/ja2025432. arXiv: 1107.3525.

9. *A. Sperlich, M. Liedtke, J. Kern, H. Kraus, C. Deibel, S. Filippone, J. L. Delgado and V. Dyakonov*. Photoinduced C70 radical anions in polymer:fullerene blends. *Phys. Stat. Sol. RRL* **5**, 3, 128 (2011). doi: 10.1002/pssr.201105030. arXiv: 1102.1899.

10. *M. Liedtke, A. Sperlich, H. Kraus, C. Deibel, V. Dyakonov, S. Filippone, J. L. Delgado, N. Martín and O. G. Poluektov*. Spectroscopic Signatures of Photogenerated Radical Anions in Polymer-[C70]Fullerene Bulk Heterojunctions. *ECS Transactions* **28**, 17, 3 (2010). doi: 10.1149/1.3503347. arXiv: 1007.1653.

In preparation

1. *H. Kraus, M. Heiber, S. Väth, J. Kern, A. Förtig, A. Sperlich, C. Deibel and V. Dyakonov*. Triplet Excitons in High-Efficiency Organic Solar Cell Materials. **In preparation** (2014).

Oral Presentations

1. DPG SKM spring meeting 2010 (Regensburg,Germany). *H. Kraus, A. Sperlich, C. Deibel and V. Dyakonov*. Conjugated Polymers and Fullerenes Under Oxygen Exposure: An Electron Spin Resonance Study.
2. DPG SKM spring meeting 2011 (Dresden, Germany). *H. Kraus, A. Sperlich, A. Keckeisen, H. Ziehlke, M. Riede, K. Leo, R. Fitzner, E. Reinhold, P. Bäuerle, C. Deibel and V. Dyakonov*. A new angle on thiophenes: the influence of molecular orientation on triplets in ODMR
3. Materials Research Society spring meeting 2012 (San Francisco, USA). *H. Kraus, S. Väth, A. Sperlich, C. Deibel and V. Dyakonov*. Studies of Electron Back Transfer and Triplet Exciton Formation in High-efficiency Conjugated Polymers-Fullerene Blends by Optically Detected Magnetic Resonance. *Upgrade to invited talk by session chair Alejandro Briseño*.
4. DPG SKM spring meeting 2013 (Regensburg, Germany). *H. Kraus, F. Späth, A. Sperlich, D. Stich, D. Schilling, T. Hertel and V. Dyakonov*. Tubes n' Triplets - On Excitation dynamics in (6,5) single-wall carbon nanotubes
5. DPK SKM spring meeting 2014. *H. Kraus, F. Fuchs, D. Riedel, V. Soltamov, D. Simin, S. Väth, A. Sperlich, P. Baranov, E. Mokhov, G.V. Astakhov and V. Dyakonov*. Room Temperature Magnetic Resonance on SiC Quantum Defects: A Silicon Carbide MASER?

Conference Posters

1. DPG SKM spring meeting 2009 (Dresden,Germany). *H. Kraus, A. Sperlich, C. Deibel and V. Dyakonov*. Photoluminescence Detected Magnetic Resonance (PLDMR) studies on P3HT-oxygen interaction
2. DFG focused program SPP1355 spring school 2010 (Krippen, Germany). *H. Kraus, A. Sperlich, M. Zerson, C. Deibel, R. Magerle and V. Dyakonov*. Semiconducting Polymers: Morphology and Triplet States Studied With Magnetic Resonance and AFM nanotomography.
3. Plastic Electronics conference 2010 (Dresden, Germany). *H. Kraus, A. Sperlich, M. Liedtke, C. Deibel, S. Filippone, J. L. Delgado, N. Martín, O.G. Poluektov*. Radical Anions in Polymer-[C70]Fullerene Bulk Heterojunctions – a spectroscopic exploration
4. DFG focused program SPP1355 summer school (2011). *H. Kraus, A. Sperlich, S. Väth, A. Topczak, M. Zerson, R. Magerle, C. Deibel and V. Dyakonov*. Magnetic resonance of solar cell materials: The influence of morphology and excitation pathways. *Winner of the EES poster prize 2011, together with A. Sperlich.*

5. DPG SKM spring meeting 2012 (Berlin, Germany). *H. Kraus, S. Väth, A. Sperlich, C. Deibel and V. Dyakonov*. Triplet Exciton Formation and Electron Back Transfer in High-Efficiency Conjugated Polymer-Fullerene Blends studied by Optically Detected Magnetic Resonance.
6. Solar Energy Conversion Meeting "Solar Technologies go Hybrid" 2013 (Kloster Banz, Germany). *H. Kraus, F. Späth, A. Sperlich, D. Stich, D. Schilling, T. Hertel and V. Dyakonov*. Tubes n' Triplets - On Excitation dynamics in (6,5) single-wall carbon nanotubes. *Winner of the EES poster prize 2013.*
7. Internation Conference on Silicon Carbide and Related Materials (ICSCRM) 2013 (Miyazaki, Japan). *H. Kraus, F. Fuchs, V. Soltamov, S. Väth, D. Riedel, A. Sperlich, P. Baranov, E. Mokhov, V. Dyakonov and G.V. Astakhov*. Room Temperature Magnetic Resonance on SiC Quantum Defects: A Silicon Carbide MASER?

Acknowledgements

Although these pages were written by one person alone, carrying out the actual research is always a team effort. First and foremost, I want to express my gratitude to my supervisor, Prof. **Vladimir Dyakonov**, for his guidance, encouragement, and staunch support, especially concerning last-minute, late-night polishing of my grant applications. He managed to create a work climate that reminded me of spending time with friends rather than acquittal of duty.

I would also like to thank my tutor, office neighbour, friend, and – recently – group leader, Dr. **Andreas Sperlich**, for sharing his profound and detailed knowledge about all things EPR and for numerous discussions unintelligible for people unsullied by computer science. Speaking of office neighbours, I would like to acknowledge my silicon carbide research partner in crime and BFF, **Franziska Fuchs**, for almost symbiotic teamwork. Thank you for always counteracting the entropy I tend to create and for readily investing a large amount of your scant time into my projects.

My group leaders of the organics and silicon carbide carbide groups, Prof. **Carsten Deibel** and Dr. **Georgy Astakhov**, respectively, also deserve gratitude for providing guidance, helping with manuscripts, and sharing personal advice. I would like to also mention all of my other colleagues at the chair of Experimental Physics VI for creating a jovial, open, and supportive working environment. I want to extend my gratitude specifically to our technicians, **André Thiem-Riebe** and **Valentin Baianov**, and to the kind heart of the chair, Ms. **Diep Phan**. Additionally, the outstanding state-of-the-art here would not be possible without all of the excellent alumni that I had the honor of meeting over the years, and who all had a significant part in bringing this work into being. Out of these, I want to specifically mention my lab neighbour, dance instructor, endurer of off-color jokes and very good friend, Dr. **Julia Kern**.

The colleagues at our cooperation partners, especially my second assessor from university of Würzburg's physical chemistry, Prof. **Tobias Hertel** and his student **Florian Späth**, and Dr. **Victor Soltamov**, Dr. **Sasha Soltamova**, and Prof. **Pavel Baranov** from IOFFE institute St. Petersburg, also deserve my sincere thanks. I also want to mention Dr. **Tom Savenije** from TU Delft, who helped me get on the right track for understanding ODMR signal genesis.

My work was thankfully supported financially by the German Research Foundation (DFG) in the context of the priority programmes SPP1355 and SPP1601 and by the Bavarian State Ministry of the Environment and Consumer Protection in the *"Umweltverträgliche hocheffiziente Organische Solarzelle"* project.

Finally, I want to thank my parents **Regine** and **Michael Kraus** for picking up the slack when I couldn't, and my beloved wife, **Nicole Kraus**, for her unwavering support, for always backing me up, and for her incredulous, but loyal understanding of a scientist's everyday routine.